

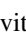




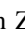










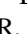
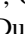
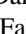
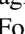
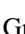
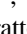


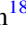
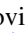




# Astrometric Accelerations as Dynamical Beacons: Discovery and Characterization of HIP 21152 B, the First T-dwarf Companion in the Hyades\*

Kyle Franson<sup>1,24</sup> , Brendan P. Bowler<sup>1</sup> , Mariangela Bonavita<sup>2</sup> , Timothy D. Brandt<sup>3</sup> , Minghan Chen<sup>3</sup> , Matthias Samland<sup>4</sup> , Zhoujian Zhang<sup>1</sup> , Anna Lueber<sup>5,6</sup> , Kevin Heng<sup>5,6,7</sup> , Daniel Kitzmann<sup>5</sup> , Trevor Wolf<sup>8</sup> , Brandon A. Jones<sup>8</sup> , Quang H. Tran<sup>1</sup> , Daniella C. Bardalez Gagliuffi<sup>9</sup> , Beth Biller<sup>10</sup> , Jeffrey Chilcote<sup>11</sup>, Justin R. Crepp<sup>11</sup> , Trent J. Dupuy<sup>12</sup> , Jacqueline Faherty<sup>9</sup> , Clémence Fontaine<sup>5</sup> , Tyler D. Groff<sup>13</sup> , Raffaele Gratton<sup>14</sup> , Olivier Guyon<sup>15,16,17</sup> , Rebecca Jensen-Clem<sup>18</sup> , Nemanja Jovanovic<sup>19</sup> , N. Jeremy Kasdin<sup>20</sup> , Julien Lozi<sup>15</sup> , Eugene A. Magnier<sup>21</sup> , Koraljka Mužić<sup>22</sup> , Aniket Sanghi<sup>1</sup> , and Christopher A. Theissen<sup>23,25</sup> 

<sup>1</sup> Department of Astronomy, The University of Texas at Austin, Austin, TX 78712, USA; [kfranson@utexas.edu](mailto:kfranson@utexas.edu)

<sup>2</sup> School of Physical Sciences, The Open University, Walton Hall, Milton Keynes, MK7 6AA, UK

<sup>3</sup> Department of Physics, University of California, Santa Barbara, Santa Barbara, CA 93106, USA

<sup>4</sup> Max-Planck-Institut für Astronomie, Königstuhl 17, D-69117 Heidelberg, Germany

<sup>5</sup> Center for Space and Habitability, University of Bern, Gesellschaftsstrasse 6, 3012 Bern, Switzerland

<sup>6</sup> Ludwig Maximilian University, University Observatory Munich, Scheinerstr. 1, Munich D-81679, Germany

<sup>7</sup> Department of Physics, Astronomy & Astrophysics Group, University of Warwick, Coventry, CV4 7AL, UK

<sup>8</sup> Department of Aerospace Engineering and Engineering Mechanics, The University of Texas at Austin, Austin, TX 78712, USA

<sup>9</sup> American Museum of Natural History, 200 Central Park West, New York, NY 10024, USA

<sup>10</sup> SUPA, Institute for Astronomy, The University of Edinburgh, Royal Observatory, Blackford Hill, Edinburgh, EH9 3HJ, UK

<sup>11</sup> Department of Physics, University of Notre Dame, 225 Nieuwland Science Hall, Notre Dame, IN 46556, USA

<sup>12</sup> Institute for Astronomy, University of Edinburgh, Royal Observatory, Blackford Hill, Edinburgh, EH9 3HJ, UK

<sup>13</sup> NASA-Goddard Space Flight Center, Greenbelt, MD 20771, USA

<sup>14</sup> INAF Osservatorio Astronomico di Padova, Vicolo dell'Osservatorio 5, I-35121 Padova, Italy

<sup>15</sup> Subaru Telescope, National Astronomical Observatory of Japan, 650 North A'ohōkū Place, Hilo, HI 96720, USA

<sup>16</sup> Steward Observatory, University of Arizona, Tucson, AZ 85721, USA

<sup>17</sup> Astrobiology Center of NINS, 2-21-1 Osawa, Mitaka, Tokyo 181-8588, Japan

<sup>18</sup> Astronomy & Astrophysics Department, University of California, Santa Cruz, CA 95064, USA

<sup>19</sup> Department of Astronomy, California Institute of Technology, 1200 East California Boulevard, Pasadena, CA 91125, USA

<sup>20</sup> Department of Mechanical Engineering, Princeton University, Princeton, NJ 08544-5263, USA

<sup>21</sup> Institute for Astronomy, University of Hawai'i, 2680 Woodlawn Drive, Honolulu, HI 96822, USA

<sup>22</sup> CENTRA, Faculdade de Ciências, Universidade de Lisboa, Ed. C8, Campo Grande, P-1749-016 Lisboa, Portugal

<sup>23</sup> Center for Astrophysics and Space Sciences, University of California, San Diego, 9500 Gilman Drive, La Jolla, CA 92093, USA

Received 2022 August 27; revised 2022 November 3; accepted 2022 November 16; published 2023 January 9

## Abstract

Benchmark brown dwarf companions with well-determined ages and model-independent masses are powerful tools to test substellar evolutionary models and probe the formation of giant planets and brown dwarfs. Here, we report the independent discovery of HIP 21152 B, the first imaged brown dwarf companion in the Hyades, and conduct a comprehensive orbital and atmospheric characterization of the system. HIP 21152 was targeted in an ongoing high-contrast imaging campaign of stars exhibiting proper-motion changes between Hipparcos and Gaia, and was also recently identified by Bonavita et al. (2022) and Kuzuhara et al. (2022). Our Keck/NIRC2 and SCExAO/CHARIS imaging of HIP 21152 revealed a comoving companion at a separation of  $0''.37$  (16 au). We perform a joint orbit fit of all available relative astrometry and radial velocities together with the Hipparcos-Gaia proper motions, yielding a dynamical mass of  $24_{-4}^{+6} M_{\text{Jup}}$ , which is  $1-2\sigma$  lower than evolutionary model predictions. Hybrid grids that include the evolution of cloud properties best reproduce the dynamical mass. We also identify a comoving wide-separation ( $1837''$  or  $7.9 \times 10^4$  au) early-L dwarf with an inferred mass near the hydrogen-burning limit. Finally, we analyze the spectra and photometry of HIP 21152 B using the Saumon & Marley (2008) atmospheric models and a suite of retrievals. The best-fit grid-based models have  $f_{\text{sed}} = 2$ , indicating the presence of clouds,  $T_{\text{eff}} = 1400$  K, and  $\log g = 4.5$  dex. These results are consistent with the object's spectral type of  $T0 \pm 1$ . As the first benchmark brown dwarf companion in the Hyades, HIP 21152 B joins the small but growing number of substellar companions with well-determined ages and dynamical masses.

*Unified Astronomy Thesaurus concepts:* Brown dwarfs (185); Direct imaging (387); T dwarfs (1679); Astrometry (80); Orbit determination (1175); Atmospheric clouds (2180)

\* Based in part on data collected at Subaru Telescope, which is operated by the National Astronomical Observatory of Japan.

<sup>24</sup> NSF Graduate Research Fellow.

<sup>25</sup> NASA Sagan Fellow.



Original content from this work may be used under the terms of the [Creative Commons Attribution 4.0 licence](https://creativecommons.org/licenses/by/4.0/). Any further distribution of this work must maintain attribution to the author(s) and the title of the work, journal citation and DOI.

## 1. Introduction

Brown dwarfs are objects that predominantly form like stars but fail to reach sufficient masses ( $\sim 70-80 M_{\text{Jup}}$ ; Dupuy & Liu 2017; Fernandes et al. 2019) to sustain hydrogen fusion, instead cooling and fading over their lifetimes (Kumar 1963). As these objects radiate away their internal energy, their colors and spectra change dramatically as a rich variety of chemical

species form and condense in their atmospheres. During this process, they pass through a series of associated spectral transitions spanning the M, L, T, and Y spectral classes (Kirkpatrick 2005; Cushing et al. 2011).

Brown dwarfs are an important bridge population between gas giants and low-mass stars. They share much of the same atmospheric chemistry as self-luminous giant planets, but are significantly brighter and easier to observe. While over one thousand field brown dwarfs have been identified, only  $\sim 200$  brown dwarf companions have been discovered via imaging, most of which are on wide orbits ( $>100$  au; Best et al. 2020). These systems serve as important benchmarks for testing atmospheric models, as their host stars enable constraints to be placed on their ages and compositions (e.g., Dupuy et al. 2009, 2014; Brandt et al. 2021a; Zhang et al. 2021b). They additionally comprise an excellent comparison population to imaged planets to delineate the upper boundary of planet formation (e.g., Nielsen et al. 2019; Bowler et al. 2020).

The gold standard for benchmark systems are objects with well-constrained ages and independent mass measurements. Since substellar objects follow mass–luminosity–age relations instead of the mass–luminosity relations of main-sequence stars, the masses of directly imaged planets and brown dwarfs are typically inferred via low-temperature cooling models (e.g., Burrows et al. 1997; Baraffe et al. 2003; Saumon & Marley 2008; Marleau & Cumming 2014; Phillips et al. 2020; Marley et al. 2021). Independent mass measurements are critical to empirically calibrate and test evolutionary models. These models encapsulate assumptions about the origin, interior structure, and atmospheres of substellar objects. This is especially true in the planetary regime, where different formation channels may significantly alter the luminosities of young objects (Fortney et al. 2008; Spiegel & Burrows 2012), with core-accretion scenarios (Pollack et al. 1996) leaving planets with lower initial entropies (“cold-start” models) than gravitational instability (Boss 1997) or turbulent fragmentation (Bate 2009) routes (the “hot-start” pathway). The burning of deuterium for brown dwarfs (and lithium at high masses; Gharib-Nezhad et al. 2021) impacts their evolution by slowing their cooling (Spiegel et al. 2011). Their atmospheres further act to regulate thermal evolution; the presence and properties of clouds, different chemical species, and nonequilibrium processes all affect the emergent spectra and the resultant luminosity evolution (Burrows et al. 2001). By testing evolutionary models and their input physics, benchmark systems therefore provide a direct window into the formation, thermal evolution, and interior structure of substellar objects.

Direct masses of substellar companions can be obtained through measurements of the gravitational reflex motion they exert on their host stars. Because most imaged substellar companions are on wide orbits, orbital motion is challenging to observe for the majority of systems. To date, there have been less than 20 precisely measured dynamical masses of substellar objects with well-constrained ages and luminosities (see recent compilation in Franson et al. 2022). The majority of these studies couple observations of the relative orbital motion of the companion with absolute astrometry of the host star (e.g., Brandt et al. 2019; Maire et al. 2020; Brandt et al. 2021c; Franson et al. 2022), usually from small proper-motion changes between Hipparcos and Gaia, and, in some cases, long-term radial velocity (RV) trends (e.g., Crepp et al. 2012;

Bowler et al. 2018; Cheetham et al. 2018; Rickman et al. 2020; Bowler et al. 2021).

This growing collection of benchmark systems has presented a conflicting story about the reliability of widely used evolutionary models. Though the majority of dynamical masses are consistent with model predictions to within  $\sim 10\%$ – $15\%$  of predicted masses, several companions are significantly less massive (Dupuy et al. 2009; Beatty et al. 2018; Rickman et al. 2020) and more massive (Cheetham et al. 2018; Brandt et al. 2021b; Bowler et al. 2021) than the predicted masses given their luminosities and ages. While overmassive companions can be explained by unresolved binarity, convincing theoretical explanations for the undermassive cases have remained elusive. There is a pressing need for new benchmark systems to test evolutionary models across a wide range of masses, ages, and luminosities.

HIP 21152 is an F5 star in the  $\sim 650$  Myr Hyades cluster (Perryman et al. 1998; Lodieu 2020). Here, we report the discovery and atmospheric characterization of HIP 21152 B, a  $24_{-4}^{+6} M_{\text{Jup}}$  brown dwarf orbiting at a separation of  $\sim 370$  mas ( $\sim 16$  au) and the first directly imaged T-dwarf companion in the Hyades. Due to the precise age and metallicity constraints from the cluster membership, HIP 21152 B offers an excellent opportunity to robustly test substellar atmospheric and evolutionary models. In parallel to our independent detection, Kuzuhara et al. (2022) and Bonavita et al. (2022) identified this companion with SCExAO/CHARIS, Keck/NIRC2, and VLT/SPHERE. Our paper presents the synthesis of all available data on the system. We combine our new Keck/NIRC2  $L'$ -band photometry and SCExAO/CHARIS ( $1.15$ – $2.39 \mu\text{m}$ ) spectrum, together with the VLT/SPHERE ( $0.95$ – $1.65 \mu\text{m}$ ) spectrum from Bonavita et al. (2022), RVs from Kuzuhara et al. (2022), and all available astrometry to carry out a comprehensive orbital and atmospheric characterization of the system.

## 2. The Astrometric Accelerations as Dynamical Beacons Survey

HIP 21152 was observed as part of the Astrometric Accelerations as Dynamical Beacons survey—an ongoing high-contrast imaging campaign targeting stars with small proper-motion differences between Hipparcos and Gaia. The goal of our program is to image new long-period planets and brown dwarfs orbiting young stars. We aim to improve the efficiency of discoveries by observing stars with astrometric accelerations consistent with being caused by wide-separation substellar companions.

HIP 21152 exhibits a significant<sup>26</sup> proper-motion difference between Hipparcos and Gaia Early Data Release 3 (EDR3) in the Hipparcos-Gaia Catalog of Accelerations (HGCA; Brandt 2018, 2021). The HGCA provides three proper-motion values: the Hipparcos proper motion, the Gaia EDR3 proper motion, and a joint Hipparcos-Gaia measurement from the difference in sky positions between the two missions. The latter two measurements produce an average tangential acceleration of  $0.041 \pm 0.004 \text{ mas yr}^{-2}$ , which corresponds to a physical acceleration of  $8.4 \pm 0.8 \text{ m s}^{-1} \text{ yr}^{-1}$  in the plane of the sky.

Our strategy to prioritize potential targets is to compute joint probability maps in separation and companion mass for stars with significant low-amplitude HGCA accelerations. The procedure is summarized as follows. For each grid point in

<sup>26</sup>  $\chi^2 = 175$ , which corresponds to  $13\sigma$  with two degrees of freedom.

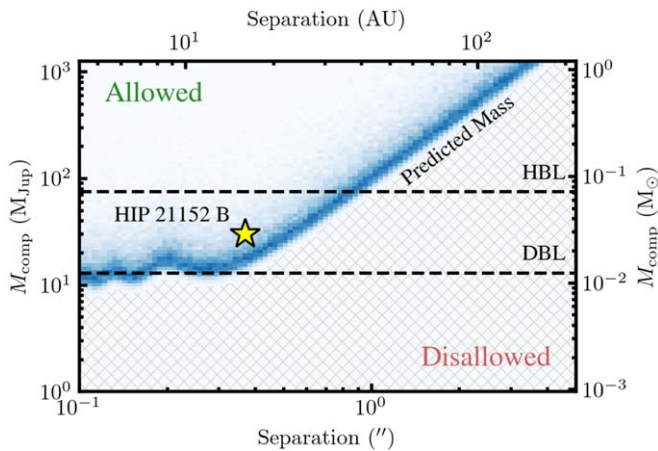


**Figure 1.** Predicted mass as a function of projected separation for HIP 21152 B based on the  $8.4 \pm 0.8 \text{ m s}^{-1} \text{ yr}^{-1}$  Hipparcos-Gaia acceleration of its host star in the HGCA. Colors indicate the relative probability of agreement; companions with separations and masses below the blue curve cannot produce the observed change in proper motion. HIP 21152’s astrometric acceleration indicates the presence of a substellar companion within  $1''$  or a star at wider separations. The dotted lines denote the hydrogen-burning limit (HBL;  $\sim 75 M_{\text{Jup}}$ ) and the deuterium-burning limit (DBL;  $\sim 13 M_{\text{Jup}}$ ). The yellow star on the plot shows the dynamical mass ( $24^{+6}_{-4} M_{\text{Jup}}$ ) and separation ( $0''.37$ ) of HIP 21152 B, which agrees with the prediction.

semimajor axis–companion mass space, 100 circular orbits<sup>27</sup> are generated with random orientations. The resulting acceleration distribution is then compared with the star’s average acceleration and uncertainty through the Kolmogorov–Smirnov statistic (Kolmogorov 1933; Smirnov 1948). The mass prediction from HIP 21152’s astrometric acceleration is shown in Figure 1. This procedure implies that there is a brown dwarf within  $1''$  or a stellar companion at wider separations. Our approach is similar to other analytical and numerical frameworks for predicting the nature of companions found with Hipparcos and Gaia (e.g., De Rosa et al. 2019; Kervella et al. 2019, 2022). By incorporating the sampling of the Hipparcos and Gaia missions, orbital curvature and aliasing is taken into account, and at wide separations the predictions mirror the power-law relation between companion mass and separation from Brandt et al. (2019).

### 3. Host Star Properties

HIP 21152 (=HD 28736, HR 1436, BD+05 674) is a bright ( $V = 6.352 \text{ mag}$ ; Jonev et al. 2006) F5V star (Oblak & Chareton 1981) with a long history of being recognized as a reliable member of the Hyades cluster<sup>28</sup> (e.g., van Bueren 1952; Perryman et al. 1998; Lodieu et al. 2019; Gaia Collaboration et al. 2021b). HIP 21152 has an effective temperature of  $6655 \pm 125 \text{ K}$  and surface gravity of  $4.3 \pm 0.2 \text{ dex}$  (Gebran et al. 2010). Its metallicity is  $[\text{Fe}/\text{H}] = 0.13 \pm 0.05 \text{ dex}$  (Boesgaard & Budge 1988). This star has a Renormalised

<sup>27</sup> If we instead generate eccentric orbits, the mass predictions at a given semimajor axis increase slightly and take on a wider range of values, which has the effect of “blurring out” mass-separation predictions.

<sup>28</sup> Gaia EDR3 proper motions of  $\mu_{\alpha} = 112.17 \pm 0.05 \text{ mas yr}^{-1}$ ,  $\mu_{\delta} = 7.76 \pm 0.05 \text{ mas yr}^{-1}$  and our RV measurement of  $40.6 \pm 1.5 \text{ km s}^{-1}$  from high-resolution spectroscopy (see Section 4.4) produce  $UVW$  space motions of  $U = -42.81 \pm 1.31 \text{ km s}^{-1}$ ,  $V = -20.25 \pm 0.23 \text{ km s}^{-1}$ , and  $W = -0.19 \pm 0.70 \text{ km s}^{-1}$ . Gagné et al. (2018) lists similar average space motions for the Hyades of ( $U, V, W$ ) =  $(-42.27, -18.79, -1.47) \text{ km s}^{-1}$ . BANYAN- $\Sigma$  (Gagné et al. 2018) gives a 99.5% membership probability in the Hyades for the EDR3 proper motions and our RV measurement.

Unit Weight Error (RUWE; Lindegren 2018) statistic in Gaia EDR3 of 0.95. RUWE values characterize the goodness-of-fit of the five-parameter astrometric solution; values above 1.4 can indicate the presence of unresolved binaries (Stassun & Torres 2021). Therefore, there is no evidence in Gaia EDR3 that HIP 21152 is an unresolved stellar binary. Long-term RVs of HIP 21152 reported in Kuzuhara et al. (2022; see Figure 5) have an RV jitter of  $39 \text{ m s}^{-1}$ . Assuming coplanarity with HIP 21152 B ( $i \approx 95^\circ$ ; Section 5), a  $0.1 M_{\odot}$  binary companion would produce RV semi-amplitudes of  $7.7 \text{ km s}^{-1}$  at 0.1 au,  $3.4 \text{ km s}^{-1}$  at 0.5 au, and  $2.4 \text{ km s}^{-1}$  at 1 au. Variations at this level are not seen in HIP 21152’s RVs.

The Hyades is the closest open cluster to the Sun (Lodieu et al. 2019). The core radius is about 3 pc and the tidal radius is about 10 pc (Perryman et al. 1998; Röser et al. 2011). Stars within the tidal radius are generally bound, while stars beyond that radius are likely unbound due to tidal stripping from the Galaxy and are therefore less reliable to identify. Lodieu et al. (2019) identified 710 candidate members within 30 pc of the center of the cluster, corresponding to a total mass of  $343 M_{\odot}$ . Two tidal tails have been found using Gaia Data Release 2 (DR2) astrometry, extending out to distances of up to 170 pc from the cluster center (Meingast & Alves 2019; Röser et al. 2019). HIP 21152’s distance of 9.75 pc from the center of the cluster (Lodieu et al. 2019) places it at the approximate tidal radius. Spectroscopic abundance measurements of Hyades members consistently point to a supersolar metallicity of the Hyades ( $[\text{Fe}/\text{H}] = 0.1\text{--}0.2 \text{ dex}$ ; Branch et al. 1980; Boesgaard & Friel 1990; Cummings et al. 2017; Takeda & Honda 2020).

There is some debate about the age of the Hyades, but most modern estimates fall between 600 and 800 Myr. Isochrone fits to the main-sequence turnoff produce ages of about 600–650 Myr (Perryman et al. 1998; Lebreton et al. 2001). Fits using evolutionary models with an updated treatment of stellar rotation by Brandt & Huang (2015a) and Brandt & Huang (2015b) yielded a somewhat older age of  $\sim 800 \text{ Myr}$ , although Gossage et al. (2018) found younger values of  $\sim 680 \text{ Myr}$  using models with a different implementation of rotation. DeGennaro et al. (2009) determined a white-dwarf cooling age of  $648 \pm 45 \text{ Myr}$ . Recent efforts to measure the cluster’s age using the lithium depletion boundary have produced an age of  $650 \pm 70 \text{ Myr}$  (Lodieu et al. 2018; Martín et al. 2018; Lodieu 2020). For this work, we adopt a fiducial age of  $650 \pm 100 \text{ Myr}$  based on these age estimates. The properties of the host star are summarized in Table 1.

## 4. Observations

### 4.1. Keck/NIRC2 Adaptive Optics Imaging

We obtained high-contrast imaging of HIP 21152 on UT 2021 December 21 with the NIRC2 camera at the W.M. Keck Observatory in  $L'$  band ( $3.426\text{--}4.126 \mu\text{m}$ ) with the Vector Vortex Coronagraph (VVC; Serabyn et al. 2017). The differential image motion monitor (DIMM) seeing for the night averaged  $0''.65$ . The observations were carried out with natural guide star adaptive optics (Wizinowich 2013) and the visible-light Shack–Hartmann wave-front sensor. Images were taken in sequences of 20–30 science frames using the quadrant analysis of coronagraphic images for tip-tilt sensing (QACITS) algorithm, which centers the star behind the vortex mask by applying small tip-tilt corrections after each exposure (Huby et al. 2015, 2017). Each sequence includes an off-axis unsaturated frame of the star for flux-calibration and sky-background frames for both the science



**Table 1**  
Properties of HIP 21152 AB

Property	Value	References
HIP 21152 A		
$\alpha_{2000.0}$	04:32:04.81	1
$\delta_{2000.0}$	+05:24:36.2	1
$\pi$ (mas)	$23.109 \pm 0.028$	1
Distance (pc)	$43.27 \pm 0.05$	1
$\mu_{\alpha, \text{EDR3}}^i$ (mas yr $^{-1}$ )	$112.17 \pm 0.05$	2
$\mu_{\delta, \text{EDR3}}$ (mas yr $^{-1}$ )	$7.76 \pm 0.05$	2
$a^{\text{ii}}$ (mas yr $^{-2}$ )	$0.041 \pm 0.004$	3
$a^{\text{ii}}$ (m s $^{-1}$ yr $^{-1}$ )	$8.4 \pm 0.8$	3
SpT	F5V	4
Mass $^{\text{iii}}$ ( $M_{\odot}$ )	$1.40 \pm 0.05$	3
Age (Myr)	$650 \pm 100$	5, 6, 7
$T_{\text{eff}}$ (K)	$6655 \pm 125$	8
$\log g$ (dex)	$4.3 \pm 0.2$	8
[Fe/H] (dex)	$0.13 \pm 0.05$	9
RV (km s $^{-1}$ )	$40.6 \pm 1.5$	3
$v \sin i$ (km s $^{-1}$ )	$45.6 \pm 1.8$	3
RUWE $_{\text{EDR3}}$	0.950	1
$V$ (mag)	$6.352 \pm 0.002$	10
Gaia $G$ (mag)	$6.2678 \pm 0.0028$	1
$J$ (mag)	$5.593 \pm 0.024$	11
$H$ (mag)	$5.385 \pm 0.020$	11
$K_s$ (mag)	$5.333 \pm 0.021$	11
$W1$ (mag)	$5.348 \pm 0.053$	12
HIP 21152 B		
Mass ( $M_{\text{Jup}}$ )	$24^{+6}_{-4}$	3
SpT	T0 $\pm$ 1	3
$\log(L_{\text{bol}}/L_{\odot})$ (dex)	$-4.57 \pm 0.07$	3
$T_{\text{eff}}^{\text{iv}}$ (K)	$1300 \pm 50$	3

#### Notes.

<sup>i</sup> Proper motion in R.A. includes a factor of  $\cos \delta$ .

<sup>ii</sup> Calculated from proper-motion difference between Hipparcos-Gaia joint proper motion and Gaia EDR3 proper motion in Brandt (2021).

<sup>iii</sup> Determined by taking the mean and standard deviation of masses for HIP 21152 from van Saders & Pinsonneault (2013), Douglas et al. (2014), David & Hillenbrand (2015), Reiners & Zechmeister (2020), Allende Prieto & Lambert (1999), Röser et al. (2011), Pace et al. (2012), Kopytova et al. (2016), Lodieu et al. (2019), and Bochanski et al. (2018).

<sup>iv</sup> Calculated using the companion’s bolometric luminosity and its model-inferred radius of  $0.997 \pm 0.023 R_{\text{Jup}}$  (see Section 6.2.2). The best fit atmospheric model had  $T_{\text{eff}} = 1400$  K, while atmospheric retrievals produced  $T_{\text{eff}} \sim 1400\text{--}1600$  K.

**References.** (1) Gaia Collaboration et al. (2021a); (2) Brandt (2021); (3) This work; (4) Oblak & Chareton (1981); (5) Gossage et al. (2018); (6) DeGennaro et al. (2009); (7) Lodieu (2020); (8) Gebran et al. (2010); (9) Boesgaard & Budge (1988); (10) Joner et al. (2006); (11) Skrutskie et al. (2006); (12) Marocco et al. (2021).

images and the flux-calibration image. The science frames consist of 90 coadds each with integration times of 0.3 s using a subarray of the central  $512 \times 512$  px for shorter readout times. Exposures were taken in pupil-tracking mode to facilitate angular differential imaging (ADI; Liu 2004; Marois et al. 2006). Excluding short pointing optimization frames taken as part of the QACITS algorithm, we obtained a total of 86 exposures of HIP 21152, amounting to 2322 s (38.7 minutes) of integration time and  $55^{\circ}9^{29}$  of frame rotation.

<sup>29</sup> 4.6 FWHM at the separation of HIP 21152 B.

Science frames are first flat-fielded and dark-subtracted. Cosmic rays are removed using the L.A.Cosmic algorithm (van Dokkum 2001) and geometric distortions are corrected by applying the solution from Service et al. (2016) for the narrow-field mode of the NIRC2 camera. The sky background is modeled and subtracted with principal component analysis (PCA) using the Vortex Image Processing (VIP) package (Gomez Gonzalez et al. 2017). Following Xuan et al. (2018), we fit four principal components to the sky-background frames, which equals the number of sky exposures for the science images. These sky principal components are then subtracted from each frame. The sky background is estimated and subtracted from off-axis flux-calibration frames in a similar fashion. Following sky subtraction, the science frames are coregistered through a cross-correlation approach developed by Guizar-Sicairos et al. (2008), which is implemented in the “register\_translation” function of scikit-image and utilized by VIP. We coregister to a median-combined frame. The absolute centering is determined by fitting a negative two-dimensional Gaussian to the vortex core.

Point-spread function (PSF) subtraction is carried out and astrometry is measured using the VIP package via a similar approach to that described in Franson et al. (2022). PCA is used to estimate the PSF for each image in the sequence (Amara & Quanz 2012; Soummer et al. 2012). Then, the PSFs are subtracted and science frames are derotated and coadded. To select the total number of PCA components  $n_{\text{comp}}$ , we run PSF subtractions from  $n_{\text{comp}} = 1$  to  $n_{\text{comp}} = 30$ , measuring the resultant companion signal-to-noise ratio (S/N) in the reduced images. S/N is determined via the method of Mawet et al. (2014), which imposes a penalty at small separations to account for the small number of resolution elements. The highest S/N is produced for the reduction using 10 components, so we adopt that for the measurement of our astrometry. The reduced image and S/N map are shown in Figure 2. We detect HIP 21152 B with a S/N of 7.9. In Appendix E, we also present an independent reduction with a modified version of the Patch COvariances (PACO) algorithm (Flasseur et al. 2018), which recovers the companion with a comparable S/N.

To minimize the introduction of systematics from the PSF subtraction method, we use the negative companion injection approach (e.g., Lagrange et al. 2010; Marois et al. 2010) to measure astrometry. A PSF template is generated by median combining the four sky-subtracted off-axis calibration frames taken over the sequence. A negative version of this is then injected into the science frames at the approximate position and with the approximate flux of the companion. After PSF subtraction, the residuals at the position of the injected template indicate how well the parameters of the input PSF template match the true values of the companion. The astrometry and photometry is first optimized through the AMOEBA downhill simplex algorithm (Nelder & Mead 1965), using the sum of the  $\chi^2$  residuals within a 1.5 FWHM aperture to assess how well the injected parameters match the companion. The parameter space is then finely explored using the emcee affine-invariant Markov Chain Monte Carlo (MCMC) ensemble sampler (Foreman-Mackey et al. 2013). We use a total of 100 walkers over 251 steps per walker (25,100 total steps) and discard the first 30% of each chain as burn-in. We assess convergence by both visually inspecting the chains and performing multiple runs of the routine, which yields identical astrometry.



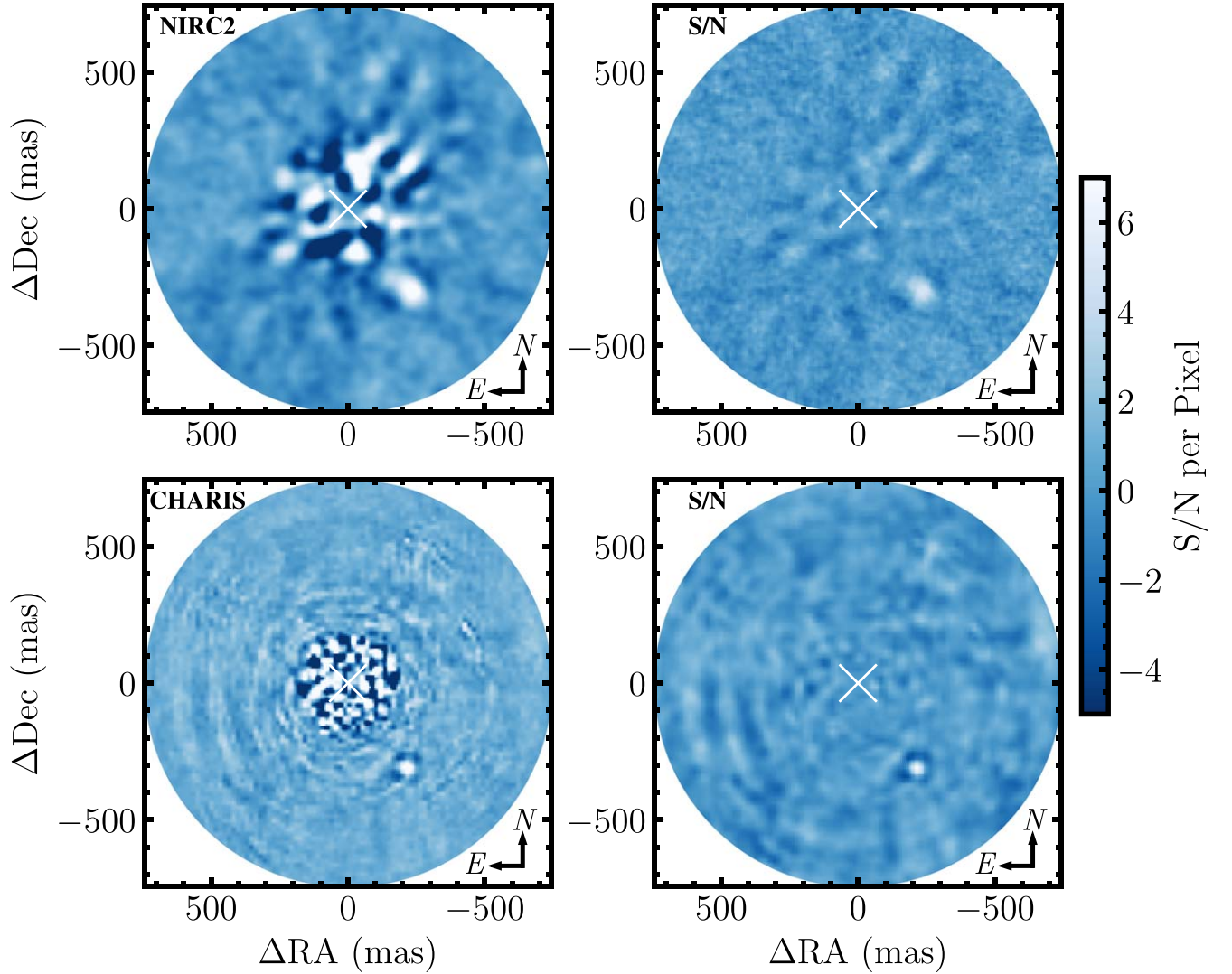


**Figure 2.** Keck/NIRC2  $L'$  (top) and SCExAO/CHARIS 1.15–2.39  $\mu\text{m}$  (bottom) imaging of HIP 21152 B. The left panels show the PSF-subtracted images for each data set, while the right panels show the corresponding S/N maps. Each frame is oriented so that north is up and east is to the left. The S/N maps are generated by measuring the flux in 0.5 FWHM-radius circular apertures at different separations and comparing the flux to noise estimated through additional nonoverlapping apertures at the same separation. We apply a Gaussian filter with a standard deviation of 1.5 px to the Keck/NIRC2  $L'$  imaging to enhance features at the scale of the recovered FWHM of the companion.

The VVC has a transmission profile that extends well beyond the inner working angle ( $\sim 125$  mas) of the coronagraph (see Figure 4 of Serabyn et al. 2017), causing a small loss of light at the separation of HIP 21152 B ( $\sim 370$  mas) and to a lesser extent at the separation of the off-axis PSF ( $\sim 500$  mas). Thus, we correct for the coronagraph at two points in this procedure: the creation of the PSF template from the off-axis frames, and each time a negative PSF is injected in the MCMC run. This is performed by computing the radial distance to the vortex center on a pixel-by-pixel basis across the image and interpolating a recently simulated PSF transmission profile of the VVC (G. Ruane, private communication, 2022) to correct for the throughput.

The MCMC run produces chains of separation, position angle, and flux ratio. We convert the flux ratio into an apparent  $L'$ -band magnitude by scaling the flux ratio to the  $W1$  magnitude<sup>30</sup> of HIP 21152 in CatWISE2020 ( $W1 = 5.348 \pm 0.053$  mag; Marocco et al. 2021). Uncertainties are produced in

a similar manner to Franson et al. (2022), incorporating the standard deviation of each parameter from the MCMC run and the uncertainty in the distortion solution, north alignment, and plate scale from Service et al. (2016). Following Wang et al. (2020), we also add a 4.5 mas QACITS centering uncertainty (Huby et al. 2017) in quadrature to account for the average pointing accuracy provided by the QACITS controller. This centering uncertainty is divided by the separation measurement before being added in quadrature to the position angle uncertainty. Our astrometry is shown in Table 2. We measure a separation of  $\rho = 371 \pm 6$  mas, position angle of  $\theta = 217^\circ 8 \pm 0^\circ 8$ , and  $L'$ -band contrast of  $\Delta L' = 9.31 \pm 0.09$  mag, which corresponds to an apparent magnitude  $L' = 14.66 \pm 0.11$  mag, absolute magnitude  $M_{L'} = 11.48 \pm 0.11$  mag, and flux density  $f_{\lambda=3.8 \mu\text{m}} = 7.3 \pm 0.7 \times 10^{-17} \text{ W m}^{-2} \mu\text{m}^{-1}$ . The flux density conversion uses the Maunakea Observatories'  $L'$  zero-point of  $5.31 \times 10^{-11} \text{ W m}^{-2} \mu\text{m}^{-1}$  from Tokunaga & Vacca (2005). Our value of the  $L'$  apparent magnitude of HIP 21152 B is consistent with the value from Kuzuhara et al. (2022) of  $L' = 15.01 \pm 0.12$  mag to within  $2.3\sigma$ .

<sup>30</sup> Here we assume that  $L' - W1 = 0$  mag, because  $W1$  and  $L'$  are in the Rayleigh–Jeans tail of the F5 host star’s spectral energy distribution.

**Table 2**  
Relative Astrometry of HIP 21152 B

Date (UT)	Epoch (UT)	Filter	Separation (mas)	PA (°)	Instrument	References
2019 Oct 26	2019.818	$J^a$	$422.4 \pm 1.5$	$217.06 \pm 0.20$	SPHERE/IFS	Bonavita et al. (2022)
2020 Oct 07	2020.767	$1.15 - 2.39 \mu\text{m}$	$408 \pm 4$	$217.4 \pm 0.7$	CHARIS	Kuzuhara et al. (2022)
2020 Dec 04	2020.925	$1.15 - 2.39 \mu\text{m}$	$401 \pm 4$	$216.7 \pm 0.7$	CHARIS	Kuzuhara et al. (2022)
2020 Dec 25	2020.982	$L'$	$406 \pm 6$	$216.4 \pm 0.8$	NIRC2	Kuzuhara et al. (2022)
2021 Oct 14	2021.785	$1.15 - 2.39 \mu\text{m}$	$379 \pm 5$	$216.9 \pm 0.8$	CHARIS	Kuzuhara et al. (2022)
2021 Dec 21	2021.971	$L'$	$371 \pm 6$	$217.8 \pm 0.8$	NIRC2	This Work
2022 Feb 27	2022.156	$1.15 - 2.39 \mu\text{m}$	$373 \pm 4$	$215.4 \pm 0.5$	CHARIS	This Work

**Note.**

<sup>a</sup> Astrometry from  $J$ -band portion of SPHERE/IFS spectrum ( $0.95\text{--}1.65 \mu\text{m}$ ).

#### 4.2. SCExAO/CHARIS Adaptive Optics Imaging

We obtained high-contrast imaging and spectroscopy of HIP 21152 B with the Coronagraphic High Angular Resolution Imaging Spectrograph (CHARIS; Groff et al. 2016) on the Subaru Telescope in low-resolution ( $R \sim 20$ ), broadband ( $1.15\text{--}2.39 \mu\text{m}$ ) mode on UT 2022 February 28. Wave-front correction was provided by both the facility AO188 system, which removes lower-order aberrations, and the Subaru Coronagraphic Extreme Adaptive Optics instrument (SCExAO; Jovanovic et al. 2015b), which provides high-order correction with a 2000-actuator deformable mirror (DM) to achieve typical Strehl ratios  $>80\%$ . The host star was occulted with the 113 mas Lyot coronagraph. The DIMM seeing for the night averaged  $0''.68$ . These data were taken in pupil-tracking mode to facilitate ADI in addition to spectral differential imaging (SDI; Marois et al. 2000; Sparks & Ford 2002) enabled by the Integral Field Spectrograph (IFS). We obtained 101 exposures each with an integration time of 30 s, amounting to  $20^\circ.4$  of frame rotation over the sequence. Spectrophotometric calibration is carried out using satellite spots—fainter copies of the host-star PSF. Four satellite spots are generated at a separation of  $11.2 \lambda/D$  (463 mas in the  $H$  band) by applying a modulation to the DM of two sine waves with amplitudes of 50 nm (Jovanovic et al. 2015a).

The CHARIS spectrum was extracted using the CHARIS raw data-reduction pipeline (Brandt et al. 2017) and the CHARIS post-processing pipeline implemented in the `pyKLIP` package (Wang et al. 2015). The CHARIS raw data-reduction pipeline constructs three-dimensional (3D) data cubes from raw detector readouts using a  $\chi^2$  spectral extraction algorithm detailed in Brandt et al. (2017). The extracted 3D data cubes consist of two-dimensional (2D) images with wavelength as the third dimension. We then use the CHARIS post-processing tools in `pyKLIP` to perform PSF subtraction, measure astrometry, and extract the companion’s spectrum. The host-star position is determined in each 2D slice by averaging the positions of the four satellite spots. The spot positions are found through a global fit of the satellite spots over all wavelength bins and exposures. PSF subtraction is carried out with the Karhunen Loève Image Processing algorithm (Soummer et al. 2012), which is a PCA-based algorithm that uses a Karhunen Loève (KL) transform (Karhunen 1947; Loève 1948) to construct eigenimages. A total of 30 principal components (KL modes) are used in the PSF subtraction. Figure 2 shows the wavelength-collapsed reduced image and S/N map. We detect HIP 21152 B at a S/N of 9.6.

The companion’s spectrum and astrometry are determined by forwarding modeling its PSF with the implementation of KLIP-FM (Pueyo 2016) in `pyKLIP`. KLIP-FM uses perturbation-based forward modeling to account for the impact of over-subtraction and self-subtraction and reduce the number of false negatives produced by classical KLIP. Our PSF models for KLIP-FM are generated by subtracting the background from the satellite spots, extracting a 15 px square region about the spot positions, and averaging over the four spots in each image and the spots from all exposures in the sequence at a given wavelength. This provides one PSF model per wavelength bin.

To optimize the position of the companion, we vary the injected companion parameters (separation and position angle) using `emcee`. We use 100 walkers over 1000 steps per walker ( $10^5$  total steps) to sample the parameter space. Astrometric calibration is provided by a short CHARIS sequence of the known binary HIP 55507 taken on the same night (see Appendix A). A plate scale of  $16.15 \pm 0.1 \text{ mas spaxel}^{-1}$  is adopted based on previous CHARIS calibration sequences (M. Chen et al. 2022, in preparation). Uncertainties in the astrometry include the MCMC-based measurement errors, the plate scale uncertainty, and, for position angle, the uncertainty from the north alignment using the calibrator ( $\pm 0^\circ.3$ ; Appendix A). These sources of error are added in quadrature and the resulting astrometry is reported in Table 2.

Spectral extraction is then carried out with the `extractSpec` module in `pyKLIP`, which implements the KLIP-FM framework to determine the spectrum of a companion, given its astrometry. The spectrum (in units of contrast) is then calibrated by interpolating Castelli–Kurucz model atmospheres to the effective temperature ( $T_{\text{eff}} = 6655 \pm 125 \text{ K}$ ; Gebran et al. 2010) and surface gravity ( $\log g = 4.3 \pm 0.2 \text{ dex}$ ; Gebran et al. 2010) of the host star. Finally, we scale our CHARIS spectrum to the SPHERE/IFS spectrum of the companion using Equation (2) of Cushing et al. (2008) to calculate the scale factor that minimizes the  $\chi^2$  value between the two spectra. The values of the extracted and rescaled 2022 CHARIS spectrum are listed in Table 3. Figure 3 shows this spectrum alongside the companion’s SPHERE/IFS spectrum and additional photometry.

#### 4.3. SPHERE/IFS Observations

HIP 21152 was observed with the Spectro-Polarimetric High-contrast Exoplanet REsearch instrument (SPHERE; Beuzit et al. 2019) on the Very Large Telescope (VLT) on UT 2019 November 26 as part of an independent high-contrast

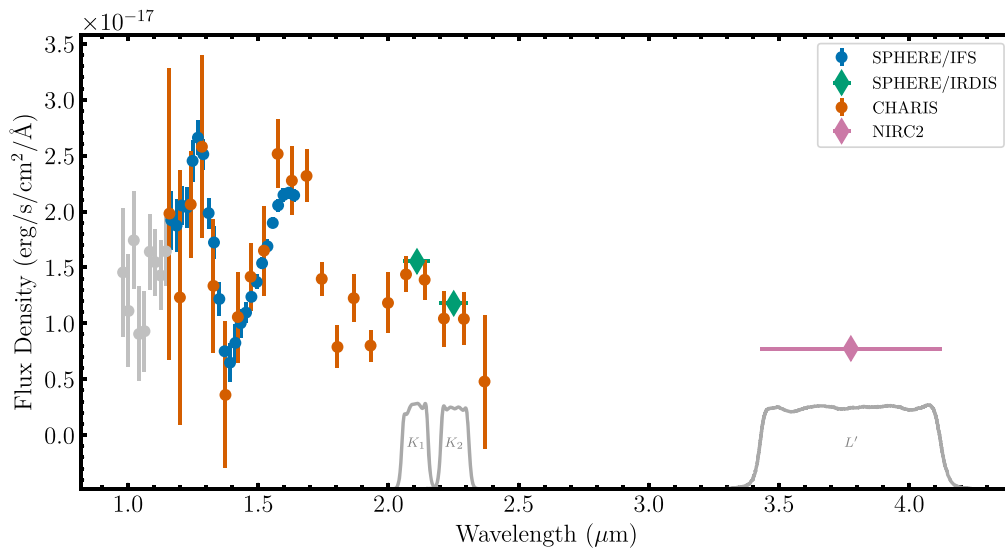


**Figure 3.** Spectra and photometry of HIP 21152 B. The blue points are the SPHERE/IFS spectrum from Bonavita et al. (2022), the green diamonds are the SPHERE/IRDIS  $K_1$  and  $K_2$  photometry from Bonavita et al. (2022), the orange points are our new SCExAO/CHARIS spectrum, and the pink diamond is our Keck/NIRC2  $L'$  photometry. Due to the modest discrepancy between the two reductions of the SPHERE/IFS spectrum at short wavelengths (Section 4.3.1), we exclude the  $\lambda < 1.15 \mu\text{m}$  region (shown in gray) from our analysis.

imaging survey of accelerating stars (Bonavita et al. 2022) selected using the Code for Orbital Parameterization of Astrometrically Inferred New Systems method (COPAINS; Fontanive et al. 2019). The observations were carried out with the IFS (Claudi et al. 2008) and Infra-Red Dual-beam Imaging and Spectroscopy (IRDIS; Dohlen et al. 2008) instruments observing in parallel. The data were taken in IRDIFS-EXT mode, which routes  $Y-H$ -band light to the IFS and  $K$ -band to IRDIS.  $K_1$ - and  $K_2$ -band filters were used for the IRDIS dual-beam imaging (Vigan et al. 2010).

The observing sequence consists of two flux-calibration subsequences in which the host star is offset from the coronagraph. In addition, two subsequences with four symmetric satellite spots for centering were obtained, a short sky-observing sequence was taken for fine correction of the hot pixel variation during the night, and the science observations were acquired with the host star behind the coronagraph. The IRDIS and IFS data sets were reduced using the SPHERE Data Reduction and Handling (DRH) automated pipeline (Pavlov et al. 2008) complemented with additional steps implemented via the SPHERE Data Center (Mesa et al. 2015; Delorme et al. 2017) for an improved wavelength calibration, and bad pixel and crosstalk correction (see Langlois et al. 2021, for details). Images of the astrometric reference field 47 Tuc observed with SPHERE on UT 2019 September 7 and UT 2019 November 28 were used for calibration. The plate scale and true north values used are based on the long-term analysis of the GTO astrometric calibration described by Maire et al. (2016).

The SpeCal software (Galicher et al. 2018) was used to subtract the host star’s PSF using PCA and spectral differential imaging (Mesa et al. 2015) for the IFS and the template locally optimized combination of images (Marchetti et al. 2014; Galicher et al. 2018) approach for IRDIS. Using ADI in combination with negative companion injection, SpeCal provides the brightness and position of the companion, and the associated uncertainties, in the IFS  $J$  and  $H$  channels and in the IRDIS  $K_1$  and  $K_2$  bands. For our orbit fit, we use the  $J$ -band value reported in Bonavita et al. (2022).

**Table 3**  
2022 February CHARIS Spectrum

$\lambda$ ( $\mu\text{m}$ )	$f_\lambda \times 10^{-17}$ ( $\text{erg/s/cm}^2/\text{\AA}$ )	$\sigma_{f_\lambda} \times 10^{-17}$ ( $\text{erg/s/cm}^2/\text{\AA}$ )
1.160	2.0	1.3
1.200	1.2	1.1
1.241	2.1	0.5
1.284	2.6	0.8
1.329	1.3	0.6
1.375	0.4	0.7
1.422	1.1	0.4
1.471	1.4	0.3
1.522	1.6	0.4
1.575	2.5	0.3
1.630	2.3	0.3
1.686	2.32	0.23
1.744	1.40	0.15
1.805	0.79	0.19
1.867	1.22	0.21
1.932	0.80	0.14
1.999	1.2	0.3
2.068	1.44	0.16
2.139	1.39	0.18
2.213	1.04	0.25
2.290	1.04	0.24
2.369	0.5	0.6

Spectral extraction of the IFS spectrum of HIP 21152 B is performed by injecting negative PSF templates generated from the flux-calibration frames at the average companion position for a given wavelength slice and adjusting the flux density to minimize the rms of the residuals in a  $9 \times 9$  px square about the companion’s mean position. Uncertainties for each point are estimated by repeating this process for five noise estimation points at the same separation as HIP 21152 B but offset in position angle by a multiple of  $60^\circ$ . This produces the spectrum shown in Figure 4. The values of this reduction of the spectrum are reported in Table 11, denoted by “Reduction 1.”



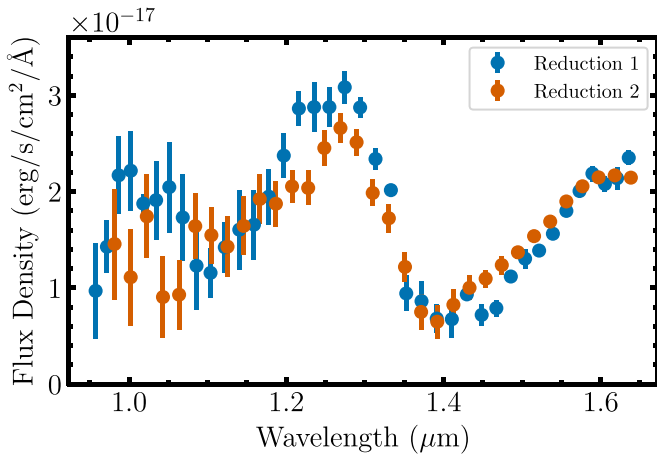


**Figure 4.** Comparison between two independent reductions of the SPHERE/IFS data. Reduction 1 uses the DRH pipeline complemented with additional steps described in Langlois et al. (2021) and the SpeCal software to extract spectral cubes from the raw data, subtract the host-star PSF, and obtain the companion’s spectrum. Reduction 2 uses a modified version of the CHARIS pipeline and the TRAP post-processing pipeline to measure the companion’s spectrum from the raw data. These two independent reductions produce similar results for  $\lambda \gtrsim 1.15 \mu\text{m}$ . Reduction 2 tends to yield lower values for the companion flux blueward of  $1.15 \mu\text{m}$  than Reduction 1. Due to this discrepancy, we exclude points with  $\lambda < 1.15 \mu\text{m}$  from this analysis.

#### 4.3.1. Independent Reduction of SPHERE/IFS Observations

We carried out a second independent reduction of the IFS spectrum using the CHARIS pipeline (Brandt et al. 2017) to extract the spectral data cubes from the raw data and the TRAP post-processing pipeline (Samland et al. 2021) to fit the planet signal and detrend the systematic noise. The CHARIS pipeline has been recently adapted to reduce SPHERE/IFS data (Samland et al. 2022), which offers several advantages over the DRH pipeline: (1) it implements improved spectral extraction methods such as “optimal extraction” and “least-square fitting” using an instrument model, (2) it provides a correct wavelength solution natively without reinterpolating the data, (3) it uses the instrument model for crosstalk correction, and (4) it significantly reduces artifacts in low S/N channels. We use this pipeline to extract 3D data cubes from each raw detector readout using the optimal extraction approach (Brandt et al. 2017). Analogous to the DRH pipeline, the position of the star is measured based on the satellite spots before and after the coronagraphic sequence. However, the unsaturated PSF images (flux frames) taken before and after the ADI sequence are relatively underexposed in some wavelengths. We therefore use the satellite spots to obtain a higher S/N unsaturated PSF model. The closest coronagraphic raw frames were first scaled and subtracted from the star center frame before extracting the images using the CHARIS pipeline. This effectively removes the static speckle background. The four satellite spots were then combined and averaged across all available frames. We determined a single star-to-spot flux ratio between the calibrated flux frames and the satellite spot frames as measured in a circular aperture ( $R = 3$  px) and averaged over all wavelengths to scale the satellite spot PSF to the flux-calibrated unsaturated stellar PSF frames. The first two unsaturated flux frames after the coronagraphic sequence were excluded as they showed signs of persistence.

The TRAP post-processing was performed using 20% of the available principal components to detrend the temporal systematics and otherwise adopted default parameters. The reduction was done channel by channel without using SDI, such that there is no overfitting or bias from training data on other spectral channels. The spectrum was then extracted at the best-fit position determined from the wavelength-combined detection image. We calibrate this spectrum using a PHOENIX-Gaia model spectrum appropriate for the temperature and surface gravity of the host star, with the absolute calibration provided by using Equation (2) of Cushing et al. (2008) to calculate the appropriate scale factor to anchor this reduction to Reduction 1. The values of this reduction of the spectrum are reported in Table 11 under “Reduction 2.”

Figure 4 displays the two reductions of the SPHERE/IFS data. While they are similar for  $\lambda \gtrsim 1.15 \mu\text{m}$ , they are discrepant at shorter wavelengths. We thus exclude flux densities at  $\lambda < 1.15 \mu\text{m}$  from our analysis. The peak flux density in the *J* band is lower for Reduction 2 than Reduction 1, with the two reductions having different spectral shapes from 1.2 to  $1.25 \mu\text{m}$ . Additionally, Reduction 2 produces a slightly higher flux from  $\sim 1.4$  to  $1.55 \mu\text{m}$ . Based on a comparison of atmospheric retrievals using both versions of the spectrum, we ultimately adopt Reduction 2 for our spectral analysis, model comparison, and retrieval work in Section 6.2.<sup>31</sup> A comparison with atmospheric models and a suite of retrievals using Reduction 1 are presented in Appendices C and D, respectively.

#### 4.4. Tull Coudé Spectra

We are uniformly acquiring high-resolution optical spectra of accelerating stars to further vet for close binaries and characterize targets in our survey. As part of this effort, we observed HIP 21152 with the Tull Coudé spectrograph (Tull et al. 1995) at the McDonald Observatory’s 2.7 m Harlan J. Smith telescope on UT 2021 October 15. Two spectra were obtained at an air mass of 1.11 with integration times of 50 s and 100 s. The  $1''/2$  slit was used, resulting in a resolving power of  $R = 60,000$  in a setup covering 56 orders (with gaps between orders) from  $3870 \text{ \AA}$  to  $10450 \text{ \AA}$ . Several slowly rotating RV standards spanning a range of spectral types were targeted in the same setup throughout the night.

Spectra are extracted and wavelength calibrated using a custom pipeline. Two-dimensional curved spectral traces are fit with a polynomial and remapped to a one-dimensional horizontal trace, then each order is optimally extracted following Horne (1986). Spectral orders are continuum normalized by dividing a fifth-order polynomial fit to each extracted spectrum. Wavelength solutions for each order are determined using a ThAr emission lamp spectrum taken on the same night with an identical setup as the science target. A ThAr emission line list is compiled from Lovis & Pepe (2007) and Murphy et al. (2007), and a third-order polynomial solution is derived for each order to map pixels to wavelengths.

<sup>31</sup> Atmospheric retrievals using Reduction 1 (Appendix D) produce significantly higher effective temperatures of  $\sim 1800\text{--}1900$  K than retrievals restricted to the CHARIS spectrum ( $T_{\text{eff}} \sim 1400$  K) or retrievals that use Reduction 2 ( $T_{\text{eff}} \sim 1400\text{--}1600$  K; Section 6.2.3), likely owing to the increased flux in the *J* band. This higher effective temperature is inconsistent with the effective temperature from the Stefan–Boltzmann law using the companion’s bolometric luminosity and a model-inferred radius ( $T_{\text{eff}} = 1300 \pm 50$  K; Section 6.2.2).

**Table 4**  
HIP 21152 B Orbit Fit Results

Parameter	Median $\pm 1\sigma$	95.4% C.I.	Prior
Fitted Parameters			
$M_{\text{comp}} (M_{\text{Jup}})$	$24^{+6}_{-4}$	(18, 46)	$1/M_{\text{comp}}$ (log-flat)
$M_{\text{host}} (M_{\odot})$	$1.37 \pm 0.20$	(0.98, 1.77)	$1.4 \pm 0.2 M_{\odot}$ (Gaussian)
$a$ (au)	$17^{+5}_{-4}$	(11, 36)	$1/a$ (log-flat)
$i$ ( $^{\circ}$ )	$95.3^{+3.9}_{-2.1}$	(91.3, 125.0)	$\sin(i)$ , $0^{\circ} < i < 180^{\circ}$
$\sqrt{e} \sin \omega$	$0.1^{+0.3}_{-0.4}$	(-0.5, 0.6)	Uniform
$\sqrt{e} \cos \omega$	$0.0^{+0.6}_{-0.7}$	(-0.9, 0.9)	Uniform
$\Omega$ ( $^{\circ}$ )	$39.3^{+2.6a}_{-1.5}$	(36.1, 50.0) <sup>a</sup>	Uniform
$\lambda_{\text{ref}}$ ( $^{\circ}$ ) <sup>b</sup>	$180^{+160}_{-30}$	(10, 360)	Uniform
Parallax (mas)	$23.109 \pm 0.030$	(23.049, 23.169)	$23.109 \pm 0.028$ mas (Gaussian)
$\mu_{\alpha}$ (mas yr $^{-1}$ )	$112.37^{+0.06}_{-0.05}$	(112.28, 112.55)	Uniform
$\mu_{\delta}$ (mas yr $^{-1}$ )	$7.80^{+0.07}_{-0.06}$	(7.68, 7.99)	Uniform
RV jitter $\sigma_{\text{RV}}$ (m s $^{-1}$ )	$< 5.293^c$	...	$1/\sigma_{\text{RV}}$ (log-flat), $\sigma_{\text{RV}} \in (0, 1000 \text{ m s}^{-1})$
Derived Parameters			
$P$ (yr)	$59^{+31}_{-16}$	(34, 183)	...
$e$	$0.36^{+0.37}_{-0.25}$	(0.02, 0.98)	...
$\omega$ ( $^{\circ}$ )	$160^{+160}_{-130}$	(10, 350)	...
$T_0$ (JD)	$2449000^{+15000}_{-4000}$	(2431000, 2468000)	...
$q (=M_{\text{comp}}/M_{\text{host}})$	$0.017^{+0.005}_{-0.003}$	(0.012, 0.035)	...

#### Notes.

<sup>a</sup> The  $\Omega$  posterior consists of two distinct peaks separated by  $180^{\circ}$ . The values shown in the table correspond to the higher peak. The other peak is located at  $218.4^{+2.3}_{-1.6}$  with a 95.4% confidence interval of (205.9, 227.6).

<sup>b</sup> Mean longitude at the reference epoch of 2010.0.

<sup>c</sup>  $2\sigma$  upper limit. The median value is  $0 \text{ m s}^{-1}$ .

The RV and projected rotational velocity of HIP 21152 are derived by cross correlating each order with observations of the stable F2 star HD 207978. Because some orders also contain strong telluric features, especially at red–optical wavelengths, only 42 orders are used for the RV and  $v \sin i$  measurements. Each order of the standard is individually broadened by convolving it with a broadening kernel assuming a linear limb-darkening law with a limb-darkening coefficient ( $\epsilon$ ) of 0.6 (Gray 2005). A fine grid of  $v \sin i$  values is sampled; the  $v \sin i$  and RV values that produce the highest cross-correlation function peak are adopted for each order. RVs relative to HD 207978 are corrected for barycentric motion and shifted to an absolute scale using the measured RV of  $18.92 \pm 0.02 \text{ km s}^{-1}$  from Soubiran et al. (2018). Projected rotational velocities are computed as the quadrature sum of the intrinsic broadening of HD 20797— $6.2 \text{ km s}^{-1}$  based on four measurements from Glebocki & Gnacinski (2005), and the additional broadening applied to the standard star spectrum.

After removing outlier measurements following a biweight estimator (Equation (9) in Beers et al. 1990), we determine an RV of  $40.6 \pm 2.2 \text{ km s}^{-1}$  and a  $v \sin i$  value of  $45.8 \pm 2.5 \text{ km s}^{-1}$  for the 50 s integration observation. For the 100 s observation we find an RV of  $40.6 \pm 2.0 \text{ km s}^{-1}$  and a  $v \sin i$  value of  $45.3 \pm 2.5 \text{ km s}^{-1}$ . We adopt the weighted mean and weighted standard deviation of these two observations for our final measurements:  $\text{RV} = 40.6 \pm 1.5 \text{ km s}^{-1}$  and  $v \sin i = 45.6 \pm 1.8 \text{ km s}^{-1}$ . These are in good agreement with values from the literature. For example, the RV from Gaia DR2 (Gaia Collaboration et al. 2018) is  $41.5 \pm 0.5 \text{ km s}^{-1}$  and the

projected rotational velocity of HIP 21152 from Glebocki & Gnacinski (2005) is  $42 \text{ km s}^{-1}$  based on three measurements.

### 5. 3D Orbit and Dynamical Mass

Our orbit fit incorporates all available relative astrometry and RVs from this work, Kuzuhara et al. (2022), and Bonavita et al. (2022). It also includes the astrometric acceleration between Hipparcos and Gaia EDR3, which enables the measurement of a precise dynamical mass of HIP 21152 B. The fit is performed with `orvara` (Brandt et al. 2021d), which uses the parallel-tempered MCMC (PT-MCMC) ensemble sampler in `emcee` to sample the orbital parameter posteriors. In PT-MCMC, individual chains span a range of “temperatures.” Low-temperature chains more accurately sample the neighborhood of a  $\chi^2$  minimum, while higher-temperature chains are capable of escaping local minima and accessing the entire parameter space. Periodically, chains swap positions, which enables low-temperature chains to be sensitive to additional peaks in the posterior distribution accessed by the higher-temperature ones. This strategy is well suited for orbit fitting of imaged companions, as their typically short orbit arcs can produce complex, multimodal posteriors.

For HIP 21152, we use 100 walkers, 20 temperatures, and  $10^7$  total steps to sample the parameter space. The coldest chain is adopted as the posterior distribution. `orvara` fits nine quantities: the host-star mass ( $M_{\text{host}}$ ), the companion mass ( $M_{\text{comp}}$ ), semimajor axis ( $a$ ), inclination ( $i$ ), eccentricity ( $e$ ), argument of periastron ( $\omega$ ), longitude of ascending node ( $\Omega$ ), the longitude at the reference epoch of 2010.0 ( $\lambda_{\text{ref}}$ ), and an RV jitter term ( $\sigma_{\text{RV}}$ ). Eccentricity and argument of periastron are fit as  $\sqrt{e} \sin \omega$  and  $\sqrt{e} \cos \omega$  to avoid the Lucy–Sweeney bias

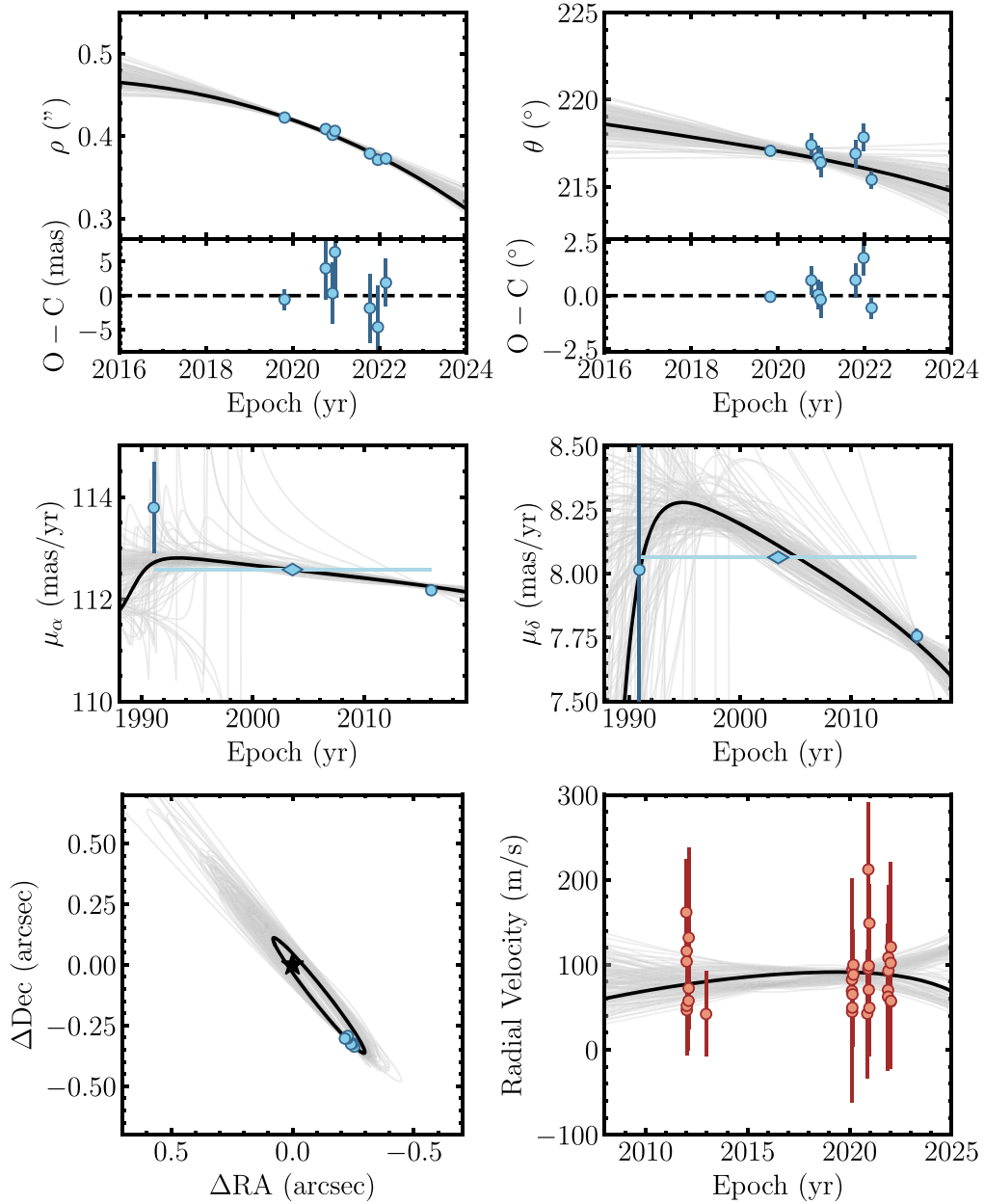


**Figure 5.** Orbit fit of HIP 21152 B compared with relative astrometry (top panels), HGCA proper motions (middle panels), sky-projected orbit (bottom-left panel), and RVs (bottom-right panel). The gray curves show 150 randomly drawn orbits from the MCMC chains. The maximum-likelihood orbit is highlighted in black. The middle proper motion (diamond) in the proper-motion panels is a joint proper motion from the difference in sky position between Hipparcos and Gaia EDR3. It is an average proper motion that reflects the reflex motion over the entire 25 yr between the missions.

against circular orbits (Lucy & Sweeney 1971). The code analytically marginalizes over instrumental RV zero-points, parallax, and barycentric proper motion.

We adopt uninformative priors for all quantities excluding primary mass. For the host-star mass, we use a broad Gaussian prior of  $1.4 \pm 0.2 M_\odot$ ,<sup>32</sup> which encompasses typical mass estimates of HIP 21152 in the literature (see Table 1) but also allows for potential systematic errors that may be larger than

the dispersion of quoted values. Log-flat priors are adopted for the companion mass, semimajor axis, and RV jitter. An isotropic,  $\sin i$  prior is used for inclination. All other quantities are assigned uniform priors. The first 50% of each walker is discarded as burn-in (5e6 steps). We assess convergence by checking that different portions of the walkers and starting positions produce the same posteriors.

Results of the orbit fit are listed in Table 4. Figure 5 compares the relative astrometry, HGCA proper motions, and RVs against a sample of the orbit solutions. The black curves highlight the maximum-likelihood orbit. Note that the central point on the proper-motion panels is a joint Hipparcos-Gaia proper motion from the difference in sky position between the two epochs. Unlike the Hipparcos and Gaia proper motions, this point is an average proper motion over the 25 yr time

<sup>32</sup> To verify that the host-star mass prior minimally impacts the resulting orbital elements, we also performed joint orbit fits with a narrow prior of  $1.40 \pm 0.10 M_{\text{Jup}}$  and a wide prior of  $1.4 \pm 0.5 M_{\text{Jup}}$ . Both runs produced consistent orbit elements within  $1\sigma$ , with the narrow prior yielding  $M_{\text{comp}} = 24^{+6}_{-4} M_{\text{Jup}}$ ,  $a = 17^{+5}_{-3}$  au,  $e = 0.35^{+0.31}_{-0.24}$ , and  $i = 95.2^{+3.0}_{-2.0}^\circ$  and the wide prior producing  $M_{\text{comp}} = 25^{+7}_{-5} M_{\text{Jup}}$ ,  $a = 17^{+5}_{-4}$  au,  $e = 0.4^{+0.4}_{-0.3}$ , and  $i = 95^{+6}_{-2}^\circ$ .



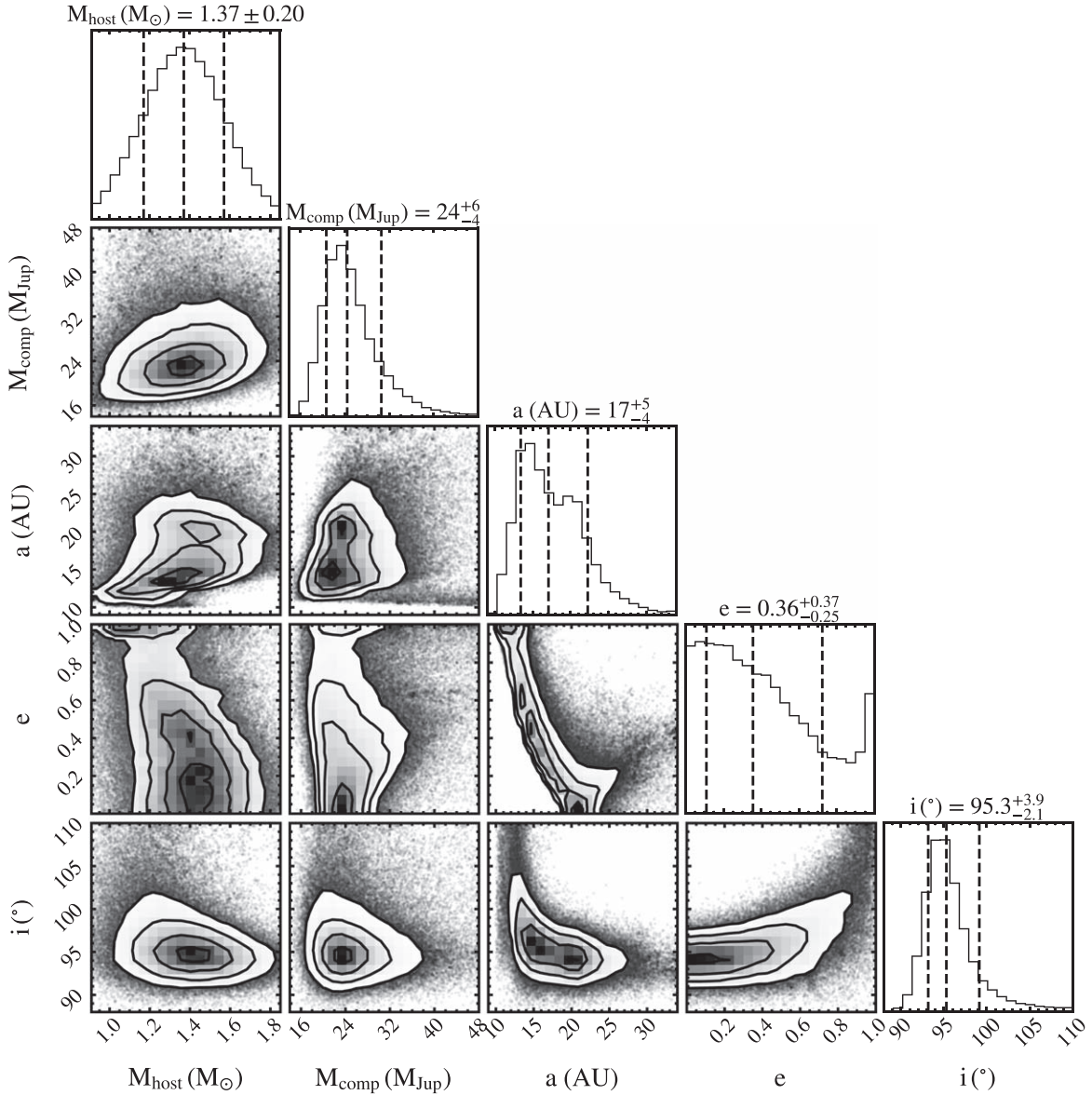


**Figure 6.** Joint posterior distributions for the primary mass ( $M_{\text{host}}$ ), companion mass ( $M_{\text{comp}}$ ), semimajor axis ( $a$ ), eccentricity ( $e$ ), and inclination ( $i$ ) from the orbit fit of HIP 21152 B. Diagonal panels show the marginalized posterior for each parameter. We measure a dynamical mass of  $24^{+6}_{-4} M_{\text{Jup}}$  for HIP 21152 B.

baseline between the missions. Figure 6 shows the posterior distributions for a subset of the orbital elements. We measure a semimajor axis of  $a = 17^{+5}_{-4}$  au, a nearly edge-on inclination of  $95.3^{+3.9}_{-2.1}$ °, and an orbital period of  $P = 59^{+31}_{-16}$  yr. The companion is moving toward its host star at a rate of  $\sim 25$  mas yr $^{-1}$ . The orbit fit yields a dynamical mass for HIP 21152 B of  $M_{\text{comp}} = 24^{+6}_{-4} M_{\text{Jup}}$ , which corresponds to a mass ratio of  $q = 0.017^{+0.005}_{-0.003}$ .

Our dynamical mass measurement is consistent with the value from Bonavita et al. (2022) of  $22 \pm 7 M_{\text{Jup}}$ , which was determined from the separation of the companion in the SPHERE/IFS data and the host star’s proper-motion difference. Kuzuhara et al. (2022) conducted a joint orbit fit of relative astrometry, RVs, and HGCA proper motions, finding values of  $M_{\text{comp}} = 28^{+9}_{-5} M_{\text{Jup}}$ ,  $a = 17^{+7}_{-4}$  au, and  $i = 105^{+18}_{-7}$ ° that are consistent with our fit. Our uncertainties on the dynamical mass and inclination measurements are 29% and 76% lower than the uncertainties from Kuzuhara et al. (2022),

respectively. This is likely due to our orbit fit’s relative astrometry covering a longer time baseline. Eccentricity is poorly constrained in both orbit fits. Continued orbital monitoring with high-contrast imaging and RVs, particularly as the companion approaches periastron, will be essential in improving the constraint on the companion’s eccentricity to facilitate comparisons with observed brown dwarf and giant planet eccentricity distributions (Bowler et al. 2020).

## 6. Discussion

### 6.1. Evolutionary Model Comparison

Our model-independent mass of HIP 21152 B and age constraint from the host star’s Hyades membership enable a direct comparison against the mass predictions of different substellar evolutionary models. We select a variety of hot-start model grids that cover the luminosity and age of the companion: Burrows et al. (1997), Cond (Baraffe et al. 2003), ATMO-2020 (Phillips et al. 2020), and the Saumon &

**Table 5**  
Model-inferred Parameters

Model	Predicted Mass <sup>a</sup> ( $M_{\text{Jup}}$ )	$P(M_{\text{Inferred}} > M_{\text{Dynamical}})^{\text{b}}$ (%)	$\Delta_{\text{mass pri}}^{\text{b}}$	Predicted Age (Myr)	$P(\text{Age}_{\text{Inferred}} > \text{Age}_{\text{Hyades}})^{\text{b}}$ (%)	$\Delta_{\text{age}}^{\text{c}}$
Burrows	$41_{-4}^{+4}$	96.1	$1.8\sigma$	$220_{-60}^{+110}$	0.7	$-2.4\sigma$
Cond	$37.8_{-3.5}^{+3.3}$	94.0	$1.6\sigma$	$280_{-80}^{+130}$	2.2	$-2.0\sigma$
ATMO2020	$38.3_{-3.5}^{+3.3}$	94.4	$1.6\sigma$	$250_{-80}^{+130}$	1.9	$-2.1\sigma$
SM (no clouds)	$38.1_{-3.4}^{+3.5}$	94.3	$1.6\sigma$	$260_{-80}^{+130}$	1.9	$-2.1\sigma$
SM (hybrid)	$34_{-4}^{+6}$	89.1	$1.2\sigma$	$340_{-110}^{+160}$	7.3	$-1.5\sigma$
SM (f2)	$41_{-4}^{+4}$	95.8	$1.7\sigma$	$230_{-70}^{+110}$	0.9	$-2.4\sigma$

**Notes.**<sup>a</sup> Predicted mass and age entries are median  $\pm 1\sigma$ .<sup>b</sup> A probability of 50% signifies that the model-inferred quantities and measurement are equivalent. Probabilities below 50% indicate that the model-inferred values are lower than the dynamical mass or system age. Probabilities above 50% indicate that the model-inferred values are higher.<sup>c</sup> One-sided Gaussian equivalent  $\sigma$ . Calculated via  $\sigma = \sqrt{2} \operatorname{erf}^{-1}(1 - 2P)$ , where  $P$  is  $P(M_{\text{Inferred}} > M_{\text{Dynamical}})$  or  $P(\text{Age}_{\text{Inferred}} > \text{Age}_{\text{Hyades}})$ .

Marley (2008) models with three cloud prescriptions (no clouds, hybrid, and cloudy).

To determine the luminosity of HIP 21152 B, we synthesize  $K_s$ -band photometry from the companion’s CHARIS spectrum. As an estimate of the uncertainty from the absolute flux calibration of the CHARIS spectrum, we scale the CHARIS spectrum to the  $K_s$ -band magnitude of  $K_s = 16.57 \pm 0.17$  mag reported in Kuzuhara et al. (2022). The uncertainty of the resulting scale factor is then incorporated into the measurement of the photometry, in addition to the individual uncertainties on each flux density measurement in the spectrum. This produces  $K_s = 16.35 \pm 0.17$  mag, which corresponds to an absolute magnitude of  $M_{K_s} = 13.13 \pm 0.18$  mag and a bolometric luminosity of  $\log(L_{\text{bol}}/L_{\odot}) = -4.57 \pm 0.07$  dex, applying the  $M_{K_s} - \log(L_{\text{bol}}/L_{\odot})$  relation from Dupuy & Liu (2017).

To generate predicted masses for each evolutionary model, we draw from the luminosity and age distributions  $10^6$  times following Franson et al. (2022). For each of these trials, we then linearly interpolate the cooling curves for a given model to obtain a corresponding inferred mass. Figure 7 compares the inferred masses for the array of hot-start models with our model-independent, dynamical mass of  $24_{-4}^{+6} M_{\text{Jup}}$ . The model predictions are summarized in Table 5. We quantify the consistency between the model-inferred masses and the companion’s dynamical mass by computing  $P(M_{\text{Inferred}} > M_{\text{Dynamical}})$ , the probability that a randomly drawn value from a given inferred mass distribution is higher than a random value drawn from the dynamical mass prior. If the two distributions are consistent with one another,  $P(M_{\text{Inferred}} > M_{\text{Dynamical}})$  should be  $\approx 50\%$ . Values below 50% signify that the inferred mass is lower than the dynamical mass, while values above 50% indicate that the inferred mass is higher than the dynamical mass. We determine  $P(M_{\text{Inferred}} > M_{\text{Dynamical}})$  by drawing  $10^6$  pairs of masses from each inferred mass distribution and the dynamical mass posterior; this probability is simply the fraction of draws where the inferred mass is higher than the dynamical mass.

We find that the model predictions are higher than the dynamical mass by  $1-2\sigma$ . The model that produces the most consistent inferred mass with the companion’s true mass is the hybrid Saumon & Marley (2008) model, which agrees to within  $1.2\sigma$ . This grid aims to represent the progression of brown dwarfs through their spectral sequence and the L/T transition by using cloudy ( $f_{\text{sed}} = 2$ ) model atmospheres for

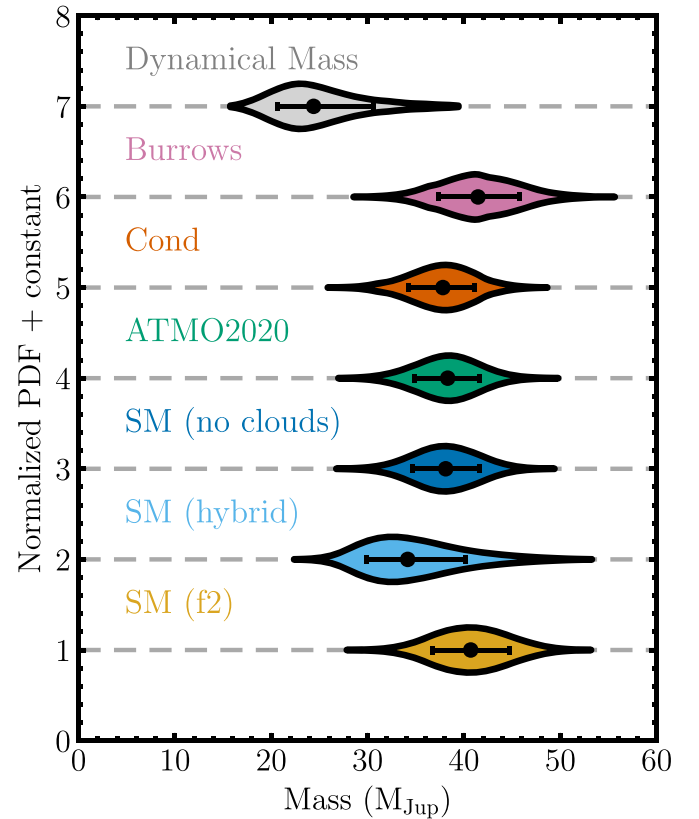


**Figure 7.** Comparison between the mass predictions of hot-start evolutionary models and the dynamical mass (top distribution) of HIP 21152 B. The median and 68.3% confidence interval are highlighted for each distribution. The dynamical mass is lower than most model predictions by  $1-2\sigma$ . The hybrid Saumon & Marley (2008) grid is most consistent with the dynamical mass, agreeing to within  $1.2\sigma$ .

$T_{\text{eff}} > 1400$  K (L dwarfs) and clear model atmospheres for  $T_{\text{eff}} < 1200$  K (T dwarfs). Between 1200 K and 1400 K, the atmosphere grid is linearly interpolated between the cloudy and clear models to emulate the breakup of iron and silicate clouds at the L/T transition. This makes these models better suited for L/T transition objects and T dwarfs than the other models we consider here. The ATMO-2020 (Phillips et al. 2020) grids are designed to model cloudless T and Y dwarfs, adopting the same assumption in Cond and the cloud-free Saumon & Marley (2008) model that dust grains settle below the photosphere and

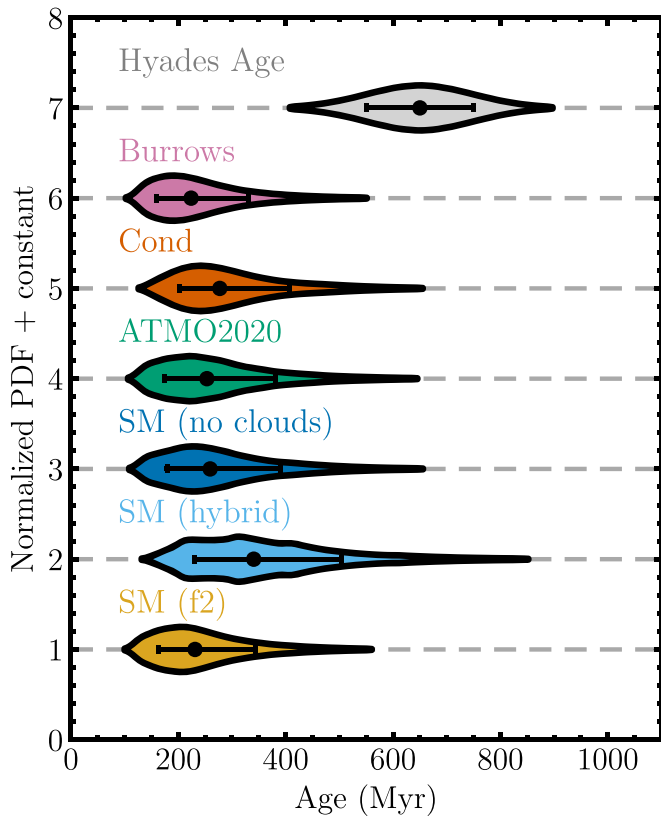


**Figure 8.** Age predictions from the luminosity and mass of HIP 21152 B for several hot-start evolutionary models. The median and 68.3% confidence interval are highlighted for each distribution. In general, the inferred ages are about  $2\sigma$  lower than the age of the Hyades ( $650 \pm 100$  Myr).

minimally impact the radiative transfer. The Burrows et al. (1997) grid uses gray cloudless (grain-free) atmospheres from Saumon et al. (1996) for  $T_{\text{eff}} \gtrsim 1300$  K and nongray model atmospheres computed in a similar manner to Marley et al. (1996) for lower effective temperatures. This approach is best suited for lower-temperature T dwarfs. The slightly better agreement between the dynamical mass and the hybrid Saumon & Marley (2008) grid than the other evolutionary models lends support for the potential presence of clouds.

We can also investigate the ages that evolutionary models predict given the companion’s luminosity and dynamical mass. Figure 8 and Table 5 present the predicted ages for the same suite of hot-start models previously examined. The model-inferred ages are determined in a similar manner as the model-inferred masses: we draw from the luminosity and dynamical mass distributions  $10^6$  times and linearly interpolate the corresponding ages for each model. The probability  $P(\text{Age}_{\text{Inferred}} > \text{Age}_{\text{Hyades}})$  is determined by drawing  $10^6$  samples from the inferred age distribution and our adopted Hyades age of  $650 \pm 100$  Myr. The inferred ages are generally 200–300 Myr lower than the nominal age of the Hyades. The model that produces the closest age of  $330^{+190}_{-120}$  Myr is the hybrid Saumon & Marley (2008) grid.

## 6.2. Spectral Analysis

### 6.2.1. Spectral Type

Our photometry and spectroscopy together with observations from Bonavita et al. (2022) are used to determine the spectral

type of HIP 21152 B.  $J$ - and  $H$ -band photometry are synthesized from our 2022 CHARIS spectrum to compare the position of HIP 21152 B in near-infrared color–magnitude diagrams (CMDs) with the empirical cooling sequence of brown dwarfs. Figure 9 shows two CMDs as a function of the companion’s  $J-H$  and  $H-L'$  colors. The sequence of substellar objects is from The UltracoolSheet (Best et al. 2020).  $W1$  magnitudes of field brown dwarfs are converted to  $L'$  magnitudes using the relation derived in Appendix B. We select all L, T, and Y dwarfs in the compilation with parallax measurements. Subdwarfs, young brown dwarfs, and unresolved close binaries are excluded. The companion’s positions on these CMDs point to a late-L or early-T spectral type.

Figure 10 compares the SPHERE/IFS spectrum, CHARIS spectrum, and SPHERE/IRDIS photometry of HIP 21152 B with the sequence of L and early-T spectral standards. The L-type standards are from Table 4 of Kirkpatrick et al. (2010). The T-type standards are from Burgasser et al. (2006), with the exception of the T3 standard SDSS J120602.51+281328.7, which was proposed by Liu et al. (2010) as a replacement for the original standard that was later found to be a binary. Each template spectrum is optimally scaled to the SPHERE and CHARIS data using the scale factor that minimizes the resulting  $\chi^2$  value. Reduced chi-squared values ( $\chi^2_{\nu}$ ) are computed between the template spectra and HIP 21152 B’s spectra and photometry. The L5 (SDSS J083506.16+195304.3) and T0 (SDSS J120747.17+024424.8) standards yield the lowest  $\chi^2_{\nu}$  values. Between those two spectral types, T0 is more consistent with the companion’s position on the CMD (Figure 9). We therefore assign HIP 21152 B a spectral type of  $T0 \pm 1$ .

### 6.2.2. Grid-based Model Comparison

To determine the physical properties of HIP 21152 B, we compare the SPHERE/IFS spectrum, SPHERE/IRDIS photometry, CHARIS spectrum, and Keck/NIRC2 photometry against model spectra from Saumon & Marley (2008). Here, we adopt Reduction 2 for the SPHERE/IFS data (see Appendix C for the same model comparison using Reduction 1). The Saumon & Marley (2008) model grid is a set of one-dimensional, hydrostatic, nongray radiative-convective atmosphere models in chemical equilibrium (see Marley & Robinson 2015 for a detailed review). It is part of a lineage of grids originally developed to model the atmosphere of Titan (McKay et al. 1989). They have since been extended to model the atmospheres of giant planets and brown dwarfs (e.g., Marley et al. 1996; Burrows et al. 1997; Marley & McKay 1999; Marley et al. 2002; Saumon et al. 2006; Cushing et al. 2008).

The models we consider here were computed using the two-stream source function approach (Toon et al. 1989) to solve the one-dimensional (1D) plane-parallel radiative transfer equation. For convective portions of the profile, the temperature gradient was iteratively fixed to the adiabatic gradient, since super-adiabaticity is negligible for cool,  $H_2$ -dominated atmospheres (Baraffe et al. 2002). Chemical equilibrium calculations were carried out following Fegley & Lodders (1994, 1996), Lodders & Fegley (2002, 2006), and Lodders (1999, 2002), with elemental abundances from Lodders (2003). These abundances confer a C/O ratio of 0.5. The  $k$ -distribution method with the correlated- $k$  approximation (Goody et al. 1989) was used to incorporate opacities. Freedman et al. (2008) outlines the



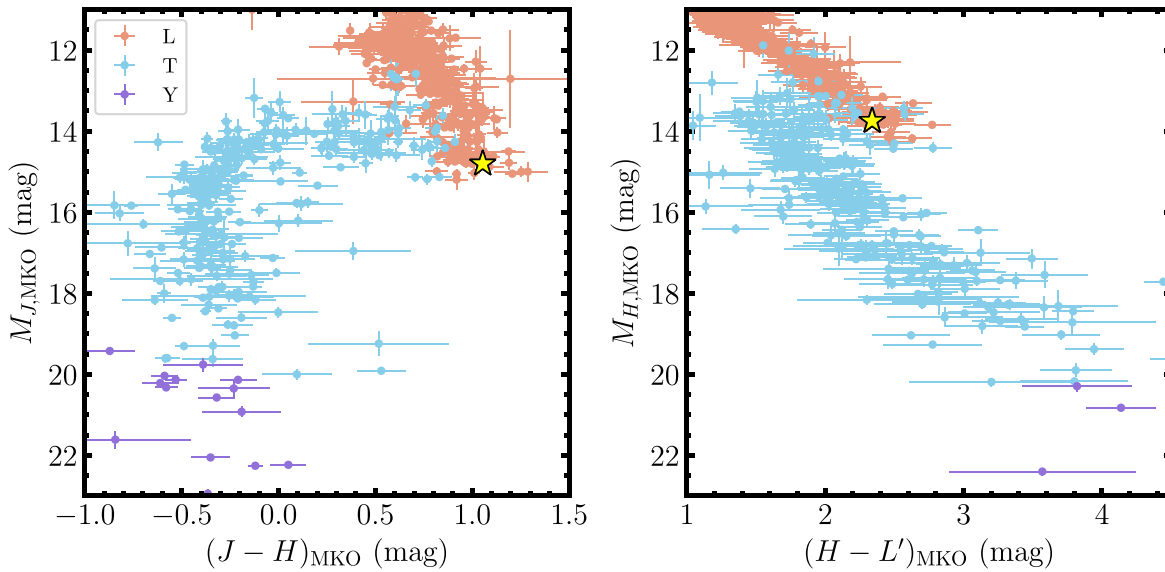


**Figure 9.** Near-infrared color–magnitude diagrams of HIP 21152 B. The companion’s position in each plot is denoted by the yellow star. The uncertainties on the companion’s magnitudes are smaller than the symbol size. The background points are L (red), T (blue), and Y (purple) dwarfs from The UltracoolSheet. The companion’s positions on these two CMDs are consistent with a late-L or early-T spectral type.

opacity data used for these models. The Ackerman & Marley (2001) cloud prescription was used to account for the effect of condensates on the emergent spectrum. This is parameterized by a sedimentation efficiency factor,  $f_{\text{sed}}$ , where larger values of the parameter imply larger particle sizes and more efficient settling. Additionally, a set of models were computed where the effects of condensation and rainout were included in the chemical equilibrium calculation but the opacity from the condensates is ignored.

The model atmospheres we consider have effective temperatures that range from  $800 \text{ K} \leq T_{\text{eff}} \leq 2400 \text{ K}$ , surface gravities that range from  $4.5 \leq \log g \leq 5.5$ , and sedimentation efficiencies  $f_{\text{sed}} = 1, 2, 3, 4$ , alongside the clear version. All synthetic spectra have solar metallicities. To compare our data against the model spectra, we first smooth and resample the models to the wavelength grid of the SPHERE/IFS spectrum, CHARIS spectrum, and photometry. Using a Gaussian kernel, we smooth the spectrum to a spectral resolution of  $R = 25$ , based on the resolutions of CHARIS ( $R \sim 20$ ) and the IFS ( $R \sim 30$  for IRDIFS-EXT mode). Each spectrum is then anchored to our data using the scale factor that minimizes the  $\chi^2$  value between the data and model. For each model, we then compute a reduced chi-square value  $\chi_\nu^2$  and a goodness-of-fit statistic  $G$ , using Equations (1) and (2) of Cushing et al. (2008). The  $G$  statistic weights spectral and photometric points by their wavelength coverage. This causes photometric points, whose bandpasses span a relatively wide range of wavelengths, to be weighted higher than individual spectral points, whose spacing covers a smaller wavelength coverage. On the other hand, the  $\chi_\nu^2$  metric weights each photometric and spectral monochromatic flux density equally and is more statistically meaningful (assuming independent, Gaussian-distributed measurement uncertainties and a model free of systematic errors), although photometry inevitably provides little additional information compared to a spectrum.

Figure 11 shows these goodness-of-fit values as a function of  $T_{\text{eff}}$ ,  $\log g$ , and  $f_{\text{sed}}$ . Generally, the two metrics yield similar results, with a clear minimum at  $T_{\text{eff}} = 1400 \text{ K}$  and best-fitting spectrum of  $(T_{\text{eff}}, \log g, f_{\text{sed}}) = (1400 \text{ K}, 4.5 \text{ dex}, 2)$  produced

by both statistics. The best-fit model corresponds to a radius of  $0.72 R_{\text{Jup}}$ . Here, the radius is determined from the flux-calibration scale factor  $C$  via  $R = d\sqrt{C}$ , where  $d$  is the distance to the system (see, e.g., Bowler et al. 2009). This model spectrum is plotted against HIP 21152 B’s spectra and photometry in Figure 12. Models with  $f_{\text{sed}} = 2$  tend to provide the best fit compared to other  $f_{\text{sed}}$  values for  $T_{\text{eff}} < 1600 \text{ K}$ . The clear models yield the poorest fit to the data.

Another approach to determine an effective temperature is by using the Stefan–Boltzmann law:

$$T_{\text{eff}} = \left( \frac{L_{\text{bol}}}{4\pi R^2 \sigma} \right)^{1/4}. \quad (1)$$

Here,  $L_{\text{bol}}$  is the companion’s bolometric luminosity and  $R$  is its radius. In Section 6.1, we determined the bolometric luminosity to be  $\log(L_{\text{bol}}/L_{\odot}) = -4.57 \pm 0.07 \text{ dex}$ . For the radius, we interpolate evolutionary model tracks from Burrows et al. (1997) in a similar fashion as the mass and age distributions in Section 6.1. We draw values from an age distribution of  $650 \pm 100 \text{ Myr}$  and the dynamical mass posterior of  $24_{-4}^{+6} M_{\text{Jup}}$  and interpolate the corresponding radius. This yields  $R = 0.997 \pm 0.023 R_{\text{Jup}}$ . The Stefan–Boltzmann law then produces an effective temperature of  $T_{\text{eff}} = 1300 \pm 50 \text{ K}$ , which is consistent with the best-fit Saumon & Marley (2008) model of  $1400 \text{ K}$ .

### 6.2.3. Atmospheric Retrieval

We also perform a suite of atmospheric retrievals on HIP 21152 B’s SPHERE/IFS spectrum, CHARIS spectrum, SPHERE/IRDIS  $K_1/K_2$  photometry, and Keck/NIRC2  $L'$  photometry. Here, we adopt Reduction 2 for the SPHERE/IFS data (see Appendix D for retrievals using Reduction 1). The atmospheric retrievals are performed with the open-source `Helios-r2` code (Kitzmann et al. 2020), which implements the MULTINEST (Feroz et al. 2009) multimodal nested sampling (Skilling 2006) algorithm for Bayesian exploration of parameter space. The forward model, which computes the

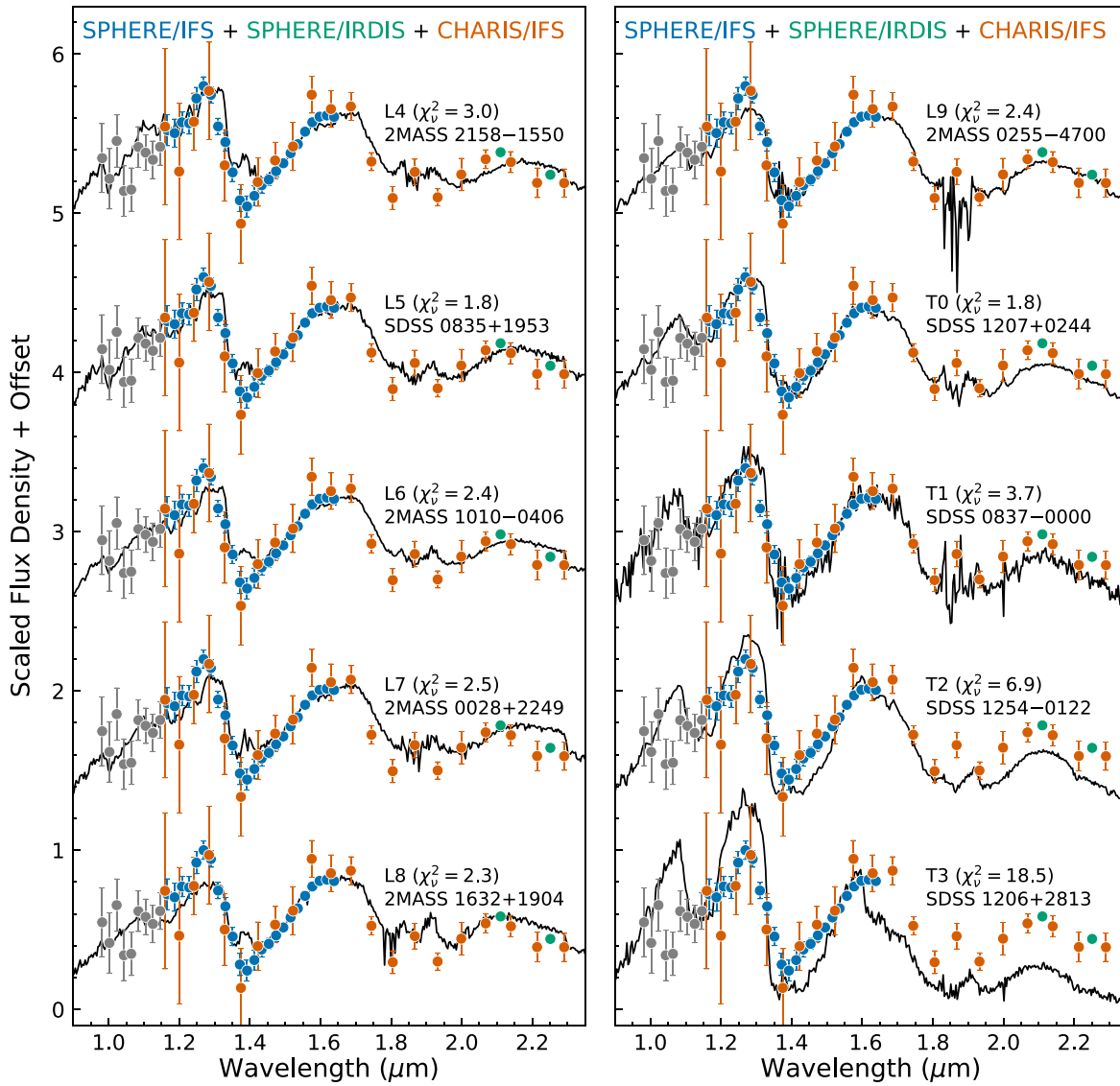


**Figure 10.** Comparison of the SPHERE/IFS spectrum (red), CHARIS spectrum (blue), and SPHERE/IRDIS photometry (red) of HIP 21152 B to L4–T3 spectral standards. We find that the T0 spectrum provides the best match to the data. We thus assign a spectral type of T0±1 for the brown dwarf companion.

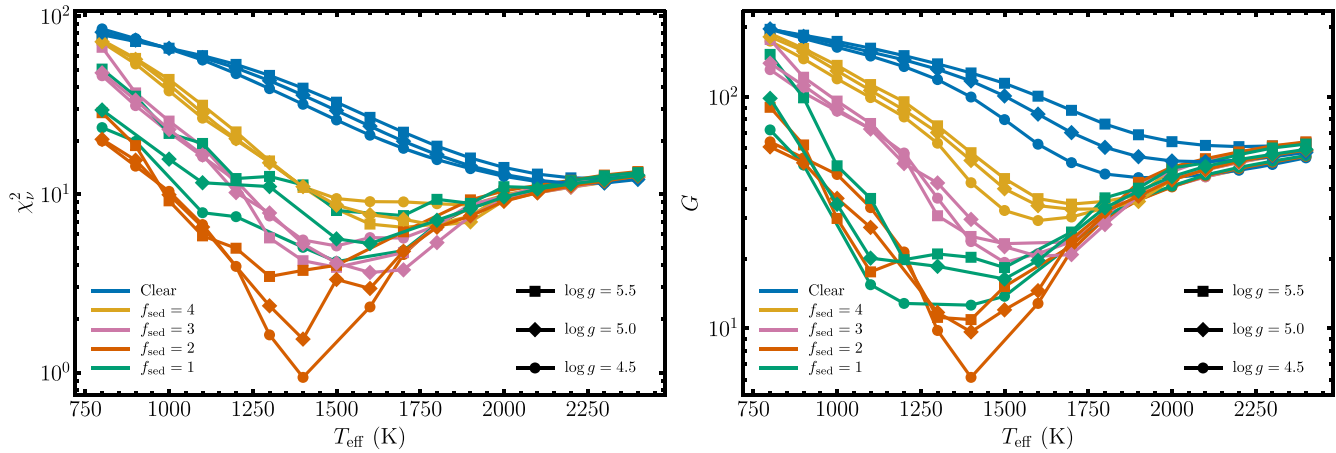


**Figure 11.** Reduced chi-square ( $\chi^2_v$ , left) and goodness-of-fit ( $G$ , right) values for model spectra from Saumon & Marley (2008) compared with HIP 21152 B's spectra and photometry. Lower values of  $\chi^2_v$  or  $G$  signify a better fit to the data. Colors indicate different values of  $f_{\text{sed}}$ , while symbols correspond to different values of  $\log g$ . Reduction 2 is used for the SPHERE/IFS spectrum. The two metrics yield the same best-fitting spectrum, with  $T_{\text{eff}} = 1400$  K,  $\log g = 4.5$ , and  $f_{\text{sed}} = 2$ .

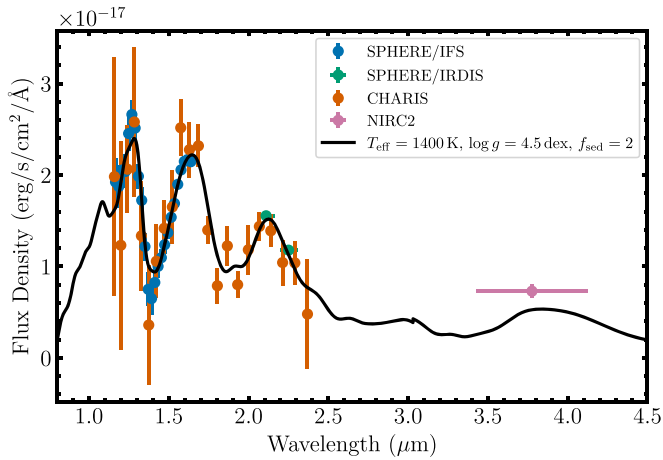


**Figure 12.** Spectra and photometry of HIP 21152 B compared with the best-fitting Saumon & Marley (2008) model spectrum (black). The model represents  $T_{\text{eff}} = 1400$  K,  $\log g = 4.5$  dex, and  $f_{\text{sed}} = 2$ , and has been smoothed to a resolving power of  $R = 25$ . Reduction 2 is used for the SPHERE/IFS spectrum. The atmospheric model reproduces the companion’s spectra well, although we find a slight excess in  $L'$  that might hint at disequilibrium chemistry from 3 to 4  $\mu\text{m}$ .

outgoing radiation flux as a function of wavelength, uses the method of short characteristics (Olson & Kunasz 1987). The temperature–pressure profile is described using seven free parameters and 70 levels (i.e., 69 layers) via a finite-element approach (Kitzmann et al. 2020). The opacities of atoms and molecules are computed using the open-source HELIOS-K calculator (Grimm & Heng 2015; Grimm et al. 2021). We include  $\text{H}_2\text{O}$ ,  $\text{CH}_4$ ,  $\text{NH}_3$ ,  $\text{CO}_2$ ,  $\text{CO}$ ,  $\text{H}_2\text{S}$ ,  $\text{CrH}$ ,  $\text{FeH}$ ,  $\text{CaH}$ ,  $\text{TiH}$ , as well as the alkali metals Na and K. Corresponding line lists are taken from the ExoMol database (Barber et al. 2006; Yurchenko et al. 2011; Yurchenko & Tennyson 2014; Azzam et al. 2016) and the HITEMP database (Rothman et al. 2010). Collision-induced absorption coefficients for  $\text{H}_2 - \text{H}_2$  and  $\text{H}_2 - \text{He}$  are based on Abel et al. (2011) and Abel et al. (2012), respectively. For the resonance lines of Na and K, we use the line profile descriptions from Allard et al. (2016) and Allard et al. (2019), as described in Kitzmann et al. (2020). Helios-r2 was previously applied to a curated sample of 19 L and T dwarfs (Lueber et al. 2022). We adopt the same criterion for model comparison using the ratio of Bayesian evidences (i.e., the Bayes factor; Trotta 2008), which are natural outcomes of the nested sampling algorithm (Skilling 2004).

The priors for our suite of retrievals are listed in Table 6. A general description of the brown dwarf forward model used here can be found in Kitzmann et al. (2020) and Lueber et al. (2022). We consider both cloud-free and cloudy atmospheres. For the cloudy cases, we either use gray or nongray clouds. Additionally, for each retrieval with clouds, both a log-uniform and a uniform prior on the cloud optical depth  $\tau$  is adopted. This follows Lueber et al. (2022), who found that when a uniform (instead of a log-uniform) prior is used for the  $\tau$ , it becomes constrained. In total, we run the companion’s spectrum and photometry through five different versions of the retrieval: one with no clouds, one with gray clouds and a log-uniform prior on  $\tau$ , one with gray clouds and a uniform prior on  $\tau$ , one with nongray clouds and a log-uniform prior on  $\tau$ , and one with nongray clouds and a uniform prior on  $\tau$ . In total, we have 21 free parameters for the cloud-free retrieval, 24

**Table 6**  
Summary of Free Parameters for Retrievals

Parameter	Description	Prior
<i>All retrievals</i>		
$\log g$	Surface gravity	3.5–6.0 (cgs; uniform)
$d$	Distance	$43.27 \pm 0.052$ pc (Gaussian)
$f$	Flux scaling factor	0.1–5.0 (uniform)
$T_1$	Temperature at base of modeled atmosphere	1000–5000 K (uniform)
$b_{i=1\dots6}$	$P/T$ profile coefficients	0.1–0.95 (uniform)
$\ln \delta$	Error inflation term	–10–1.0 (uniform)
$x_i$	Mixing ratio of species $i$	$10^{-12} - 0.1$ (log-uniform)
<i>Gray clouds</i>		
$p_t$	Pressure at top of cloud	$10^{-2} - 50$ bar (log-uniform)
$b_c$	Cloud base pressure scale factor	1–10 (log-uniform)
$\tau$	Optical depth	$10^{-5} - 20$ (log-uniform)
<i>Nongray clouds</i>		
$p_t$	Pressure at top of cloud	$10^{-2} - 50$ bar (uniform)
$b_c$	Cloud base pressure scale factor	1–10 (log-uniform)
$\tau_{\text{ref}}$	Optical depth at reference wavelength	$10^{-5} - 20$ (log-uniform)
$Q_0$	Particle size (dimensionless) with highest extinction	1–100 (log-uniform)
$a_0$	Power-law index for small particles	3–7 (uniform)
$a$	Particle size	0.1–50 $\mu\text{m}$ (log-uniform)
<i>Additional <math>\tau</math> prior</i>		
$\tau$	Optical depth	–10–20 (uniform)

**Note.** We consider five different retrieval versions: one with no clouds, two with gray clouds, and two with nongray clouds. The four cloudy retrievals consist of two with log-uniform priors on  $\tau$  and two with uniform priors on  $\tau$ .

free parameters for the gray cloud retrievals, and 27 for the nongray cloud retrievals.

We consider retrievals for three combinations of HIP 21152 B’s spectra and photometry: the SPHERE/IFS spectrum only; the CHARIS spectrum only; and the combined data set of the IFS spectrum, CHARIS spectrum, SPHERE/IRDIS  $K_{12}$  photometry, and Keck/NIRC2  $L'$  photometry. Due to the discrepancy between the two reductions of the SPHERE/IFS data at short wavelengths (see Section 4.3.1 and Figure 11), we exclude points with  $\lambda < 1.15 \mu\text{m}$ . This also circumvents unresolved issues with the shapes of the alkali metal resonance line wings (Oreshenko et al. 2020). The posteriors for the suite of retrievals are shown in Table 12, while Table 7 summarizes the Bayesian evidences for each retrieval and the relative Bayes factors  $B_{ij}$  between each cloudy retrieval and the cloud-free retrieval. Figure 13 displays the spectra and photometry of HIP 21152 B against the best-fit retrievals. The posteriors of the five permutations of different retrieval models (cloud-free and cloudy scenarios) for each data set yield very similar values. This is consistent with the Bayes factors being close to unity for all cases, indicating that there is not a significant statistical preference between the retrieval models. Though there are slight differences in the posteriors between retrievals with



**Table 7**  
Summary of Bayesian Statistics for Atmospheric Retrievals

Model	Parameter	IFS	CHARIS	IFS + CHARIS + Photometry
Cloud-free	Log evidence	275.83	275.26	558.35
Gray clouds (log-uniform $\tau$ )	Log evidence	274.18	274.18	557.41
Gray clouds (uniform $\tau$ )	Log evidence	274.08	273.78	556.62
Nongray clouds (log-uniform $\tau$ )	Log evidence	273.71	273.26	556.28
Nongray clouds (uniform $\tau$ )	Log evidence	272.84	272.97	555.63
Gray clouds (log-uniform $\tau$ ) versus cloud-free	$\ln B_{ij}^a$	1.66	1.08	0.94
Gray clouds (uniform $\tau$ ) versus cloud-free	$\ln B_{ij}^a$	1.75	1.48	1.74
Nongray clouds (log-uniform $\tau$ ) versus cloud-free	$\ln B_{ij}^a$	2.12	1.99	2.08
Nongray clouds (uniform $\tau$ ) versus cloud-free	$\ln B_{ij}^a$	2.99	2.29	2.73

**Note.**

<sup>a</sup> The Bayes factor  $B_{ij}$  is the ratio of the Bayesian evidence values for two models (Trotta 2008).  $\ln B_{ij} \sim 1$  signifies weak evidence for a statistical preference between the two models, while  $\ln B_{ij} \gtrsim 5$  indicates strong evidence.

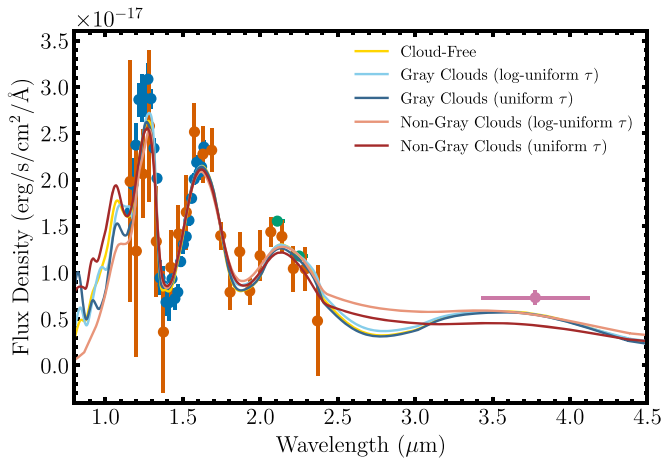


**Figure 13.** Spectra and photometry of HIP 21152 B compared with the best-fit retrievals for each of the five prescriptions we consider. Here we show the retrievals performed with the complete data set (IFS and CHARIS spectra, and photometry) using Reduction 2 for the SPHERE/IFS spectrum. The colors of the spectra and photometry are the same as in Figures 3 and 12. The retrieval models have been smoothed to a resolving power of  $R = 25$ .

subsets of the data (i.e., a slightly lower median  $T_{\text{eff}}$  for the retrieval with only the CHARIS spectrum), the retrieval results remain generally consistent. Depending on the retrieval and the subset of the data used, we obtain a surface gravity of  $\log g \sim 4.9\text{--}5.4$  and effective temperature of  $T_{\text{eff}} \sim 1400\text{--}1600$  K. These effective temperatures are roughly consistent with the value from the companion’s bolometric luminosity and radius ( $1300 \pm 50$  K) and the best-fit Saumon & Marley (2008) model spectrum (1400 K). The small retrieved radii of  $0.5\text{--}0.8 R_{\text{Jup}}$  is a recurrent issue with retrievals, possibly indicating missing physics or chemistry (Kitzmann et al. 2020; Lueber et al. 2022).

Water is formally detected in all retrievals with a volume mixing ratio  $x_{\text{H}_2\text{O}} \sim 10^{-3}\text{--}10^{-2}$ , while potassium, chromium hydride, iron hydride, and titanium hydride are only partially detected, depending on the wavelength coverage and spectral resolution of the data set. For these chemical species, the mixing ratios are roughly constant with values of about  $10^{-10}\text{--}10^{-8}$ . Similar to Lueber et al. (2022),  $\tau$  is unconstrained for the cloudy retrievals that utilize a log-uniform prior for  $\tau$ , but it becomes

constrained when a uniform  $\tau$  prior is adopted. Besides the cloud-top pressures, other cloud properties—especially the nongray cloud properties—remain unconstrained.

### 6.3. Transit Search in TESS

The Transiting Exoplanet Survey Satellite (TESS; Ricker et al. 2014) observed HIP 21152 at a 2 minute cadence during Sectors 4 and 32 for a total of 62 days. We downloaded the Science Processing Operations Center (SPOC) reduced Pre-search Data Conditioning Simple Aperture Photometry light curve (Smith et al. 2012; Stumpe et al. 2012, 2014) from the Mikulski Archive for Space Telescopes data archive<sup>33</sup> using the `lightkurve` (Lightkurve Collaboration et al. 2018) software package. All photometric measurements flagged as poor quality by the SPOC pipeline (`DQUALITY > 0`) or listed as NaN were removed. Positive outliers at  $3\sigma$  and negative outliers at  $10\sigma$  were further rejected to allow for possible transit events. We detrended the light curve using a 1D box-smoothing kernel with a one-hour width. The detrended light curve has an rms of 0.2 ppt (in units of relative flux). We searched for signals of a transiting planet in the detrended light curve using a box least-squares search (Kovács et al. 2002) between 0.5 and 30 day orbits, but did not identify any significant periodic transit-like events.

### 6.4. A Wide Common-proper-motion Companion

To investigate the outer architecture of the HIP 21152 system, we search for any wide-separation comoving companions using Gaia EDR3 (Gaia Collaboration et al. 2016, 2021a) and Pan-STARRS1 (PS1; Chambers et al. 2016; Magnier et al. 2020). For each survey, we follow Zhang et al. (2021a) and apply the following conditions to identify wide companions: (1) the projected separation between the two components is  $< 10^5$  au; (2) the companion’s proper motion has a  $S/N > 5$ ; (3) the vector difference between the proper motions of HIP 21152 A ( $\vec{\mu}_p$ ; from Gaia EDR3) and the companion ( $\vec{\mu}_c$ ; from Gaia or PS1) is within 30% of HIP 21152 A’s total proper motion (i.e.,  $|\vec{\mu}_c - \vec{\mu}_p| \leq 0.3|\mu_p|$ ); (4) the parallax difference between HIP 21152 A and the companion is within 30% of HIP 21152 A’s parallax; (5) if present, the RVs of two components are consistent to within  $3\sigma$ . We only applied the

<sup>33</sup> <https://archive.stsci.edu/missions-and-data/tess/>

**Table 8**  
Properties of HIP 21152 C

Property	Value	References
$\alpha_{2000.0}$	04:33:56.60	1
$\delta_{2000.0}$	+05:37:23.54	1
$\pi$ (mas)	$22.62 \pm 0.45$	1
$\mu_\alpha$ (mas yr <sup>-1</sup> )	$107.17 \pm 0.49$	1
$\mu_\delta$ (mas yr <sup>-1</sup> )	$7.60 \pm 0.39$	1
Distance (pc)	$44.2 \pm 0.9$	1
Projected separation (″)	1837	2
Projected separation (10 <sup>4</sup> au)	7.9	2
3D separation (10 <sup>5</sup> au)	$2.5 \pm 1.4$	2
SpT	L0/1	3, 4
RUWE	1.05	1
$\log(L_{\text{bol}}/L_\odot)$ (dex)	$-3.62 \pm 0.04$	2
Mass ( $M_{\text{Jup}}^a$ )	$73 \pm 7$	2
Binding energy (10 <sup>39</sup> erg)	$-5 \pm 4$	2
$r$ (mag)	$21.64 \pm 0.07$	5
$i$ (mag)	$19.538 \pm 0.009$	5
$z$ (mag)	$18.039 \pm 0.008$	5
$y$ (mag)	$17.087 \pm 0.009$	5
Gaia $G$ (mag)	$19.969 \pm 0.004$	1
$J$ (mag)	$15.28 \pm 0.06$	6
$H$ (mag)	$14.39 \pm 0.06$	6
$K$ (mag)	$13.91 \pm 0.06$	6

**Note.**

<sup>a</sup> Inferred via the BHAC15 evolutionary model (Baraffe et al. 2015).

**References.** (1) Gaia Collaboration et al. (2021a); (2) This work; (3) Reylé (2018); (4) Gagné & Faherty (2018); (5) Chambers et al. (2016); (6) Skrutskie et al. (2006).

last two criteria when searching for companions in Gaia. This process produced one candidate common-proper-motion companion: 2MASS J04335658+0537235 (HIP 21152 C herein-after). The properties of HIP 21152 C are summarized in Table 8. The PS1 and Gaia EDR3 proper motions and parallax values for HIP 21152 A and HIP 21152 C are plotted against nearby sources in Figure 14.

HIP 21152 C has an angular separation of 1837″ from HIP 21152 A, corresponding to a projected physical separation of  $7.9 \times 10^4$  au at the primary star’s distance. The Gaia astrometry of HIP 21152 C is determined from 20 visibility periods, with a RUWE of 1.05, suggesting this wide-orbit companion is likely single. HIP 21152 C was previously identified as a Hyades member by Gagné & Faherty (2018) using BANYAN $\Sigma$  (Gagné et al. 2018) and Gaia DR2 astrometry. HIP 21152 C was also independently found by Reylé (2018) in their Gaia-based search for ultracool dwarfs. Based on the object’s  $G$ -band absolute magnitude, Gagné & Faherty (2018) and Reylé (2018) assigned a spectral type of L1 and L0 to this companion, respectively.

To determine the bolometric luminosity and infer the mass of the object, we first convert its  $H$ -band magnitude from 2MASS to an absolute magnitude  $M_{H_{2\text{MASS}}} = 11.17 \pm 0.08$  mag using HIP 21152 C’s Gaia EDR3 parallax. The  $M_{H_{2\text{MASS}}} - \log(L_{\text{bol}}/L_\odot)$  relation from Dupuy & Liu (2017) then yields a luminosity  $\log(L_{\text{bol}}/L_\odot) = -3.62 \pm 0.04$  dex. We determine a mass for HIP 21152 C by drawing  $10^6$  samples from its luminosity and the age distribution of the Hyades ( $650 \pm 100$  Myr; Section 3) and interpolating the BHAC15 evolutionary model grid (Baraffe et al. 2015). This yields a model-inferred mass of  $73 \pm 7 M_{\text{Jup}}$ . The hydrogen-burning

limit (HBL) is defined as the mass at which half of an object’s luminosity is generated by fusing hydrogen (Reid & Hawley 2005) and is primarily a function of opacity (metallicity) and helium fraction (Burrows et al. 2001). Rotation rate can also influence the HBL (Chowdhury et al. 2022). Stars with higher opacities, metallicities, helium fractions, and slower rotation rates can sustain hydrogen burning at lower masses. Generally, model and empirically determined HBLs range from  $\approx 70\text{--}80 M_{\text{Jup}}$  (Saumon & Marley 2008; Scudlaire et al. 2008; Baraffe et al. 2015; Dupuy & Liu 2017; Fernandes et al. 2019). HIP 21152 C’s mass of  $73 \pm 7 M_{\text{Jup}}$  places it at the HBL, so it is unclear whether it is a low-mass star or a brown dwarf. This corresponds to a mass ratio of  $q = 0.049 \pm 0.005$ . The binding energy of the HIP 21152 AC pair is  $(5 \pm 4) \times 10^{39}$  erg. This is similar to other wide common-proper-motion low-mass companions with very low binding energies of  $\sim 10^{40}$  erg (see, e.g., Dhital et al. 2010; Faherty et al. 2010).

We determine the odds that HIP 21152 AC is a chance alignment with unrelated Hyades members by calculating the probability of there being at least two cluster members within a  $10^5 \times 10^5 \times (2 \times 10^5)$  au ellipsoid. The first two dimensions are based on the search criterion that the projected separation between two sources is  $< 10^5$  au. The last dimension is from the parallax difference between HIP 21152 A and HIP 21152 C, which corresponds to a line-of-sight distance of  $0.94 \text{ pc} \approx 2 \times 10^5$  au. We estimate the number density of Hyades stars at HIP 21152’s position by selecting the Hyades sources in Lodieu et al. (2019) with physical distances in a volumetric shell from the cluster center within 1 pc of HIP 21152’s distance of 9.75 pc. After dividing by the volume of the shell, this yields a density of  $n = 0.023$  stars/pc<sup>3</sup>. The probability of two or more sources occurring in a region of volume  $V$  and number density  $n$  is given by the complement of a Poisson distribution:

$$P(N \geq 2) = 1 - P(N = 1) = 1 - \lambda e^{-\lambda}, \quad (2)$$

where the rate is  $\lambda = nV$ . We find that the probability of chance alignment  $P(N \geq 2) = 0.7\%$ , so this companion is likely physical. Although HIP 21152 A and C have consistent distances ( $43.27 \pm 0.05$  pc and  $44.2 \pm 0.9$  pc), we note that there is a modest uncertainty on the line-of-sight distance between the objects of  $\pm 0.9$  pc. If we extend the ellipsoid to have a depth of  $2.74 \text{ pc} \approx 5.7 \times 10^5$  au, representing a  $2\sigma$  increase in the distance between the sources, the resulting probability of chance alignment  $P(N \geq 2) = 2\%$ , which remains low. We therefore conclude that HIP 21152 C is likely a bound companion and not a chance alignment of an isolated Hyades member.

One can compare the proper motion of the barycenter of the system from the joint orbit fit of HIP 21152 B (Section 5) and the Gaia EDR3 proper motion of HIP 21152 C to assess whether the proper motions are compatible with the object being bound. We first convert the barycenter proper motions in Table 4 to the position of HIP 21152 C using the Gaia EDR3 coordinates, parallaxes of the A and C components, and our RV of  $40.6 \pm 1.5 \text{ km s}^{-1}$  (Section 4.4). The resulting barycenter proper motions at the position of HIP 21152 C are  $\mu_\alpha = 108.4 \pm 2.5 \text{ mas yr}^{-1}$  and  $\mu_\delta = 6.8 \pm 0.7 \text{ mas yr}^{-1}$ . Compared with the EDR3 proper motions of  $\mu_\alpha = 107.17 \pm 0.49 \text{ mas yr}^{-1}$  and  $\mu_\delta = 7.60 \pm 0.39 \text{ mas yr}^{-1}$ , the barycenter proper motion differs by  $\Delta_\mu = 2.6 \pm 1.6 \text{ mas yr}^{-1}$ , or  $\Delta_\mu = 0.55 \pm .32 \text{ km s}^{-1}$ . The 3D

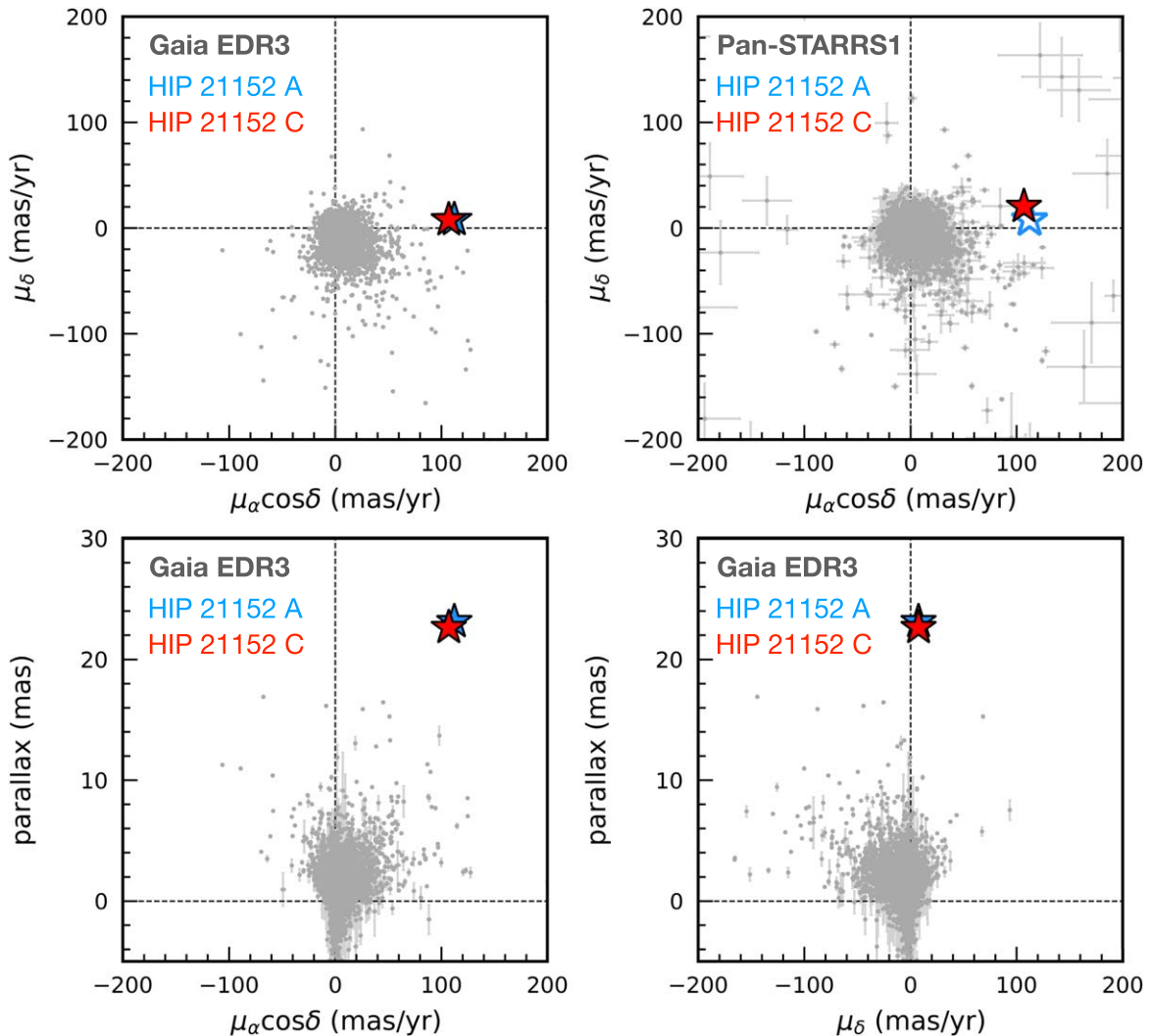


**Figure 14.** Top: proper motions of HIP 21152 A (blue) and HIP 21152 C (red) from Gaia EDR3 (top left) and PS1 (top right), overlaid with nearby sources within a radius of  $1^\circ$  (gray). We only show PS1 neighbors if their proper motions have  $S/N > 5$  or have errors  $< 10 \text{ mas yr}^{-1}$ . The host star does not have a PS1 proper motion given that it is saturated, so we plot its Gaia EDR3 proper motion (blue open symbol) in the top-right panel. Bottom: Gaia EDR3 proper motions and parallaxes of HIP 21152 AC and nearby sources shown in the top-left panel. The potential association between the A and C components is indicated by their common proper motions and parallaxes.

separation between HIP 21152 A and C is  $(2.5 \pm 1.4) \times 10^5 \text{ au}$ . At that distance, the escape velocity from the host star is  $v_{\text{esc}} = 0.11 \pm 0.04 \text{ km s}^{-1}$ .  $\Delta_\mu$  is thus compatible with the companion being bound to within  $2\sigma$ . A future RV measurement of HIP 21152 C would enable the determination of the 3D relative velocity between the barycenter and the source as an additional assessment of whether the companion is bound.

## 7. Conclusions

In this work, we reported the independent discovery of HIP 21152 B, the first imaged brown dwarf companion in the Hyades, along with a comprehensive characterization of its orbital and atmospheric properties. HIP 21152 was targeted in our ongoing Astrometric Accelerations as Dynamical Beacons program due to its small but significant Hipparcos-Gaia astrometric acceleration of  $8.4 \pm 0.8 \text{ ms}^{-1} \text{ yr}^{-1}$ . A joint orbit fit of its relative astrometry including new Keck/NIRC2 and CHARIS imaging, RVs, and HGCA acceleration yields a dynamical mass of  $24_{-4}^{+6} M_{\text{Jup}}$ . This measurement is slightly lower ( $1-2\sigma$ ) than model-inferred masses from substellar

evolutionary models, with the Saumon & Marley (2008) hybrid grid that incorporates both the presence and dissipation of clouds producing the most consistent inferred mass. HIP 21152 B is the first benchmark brown dwarf with a model-independent mass in the Hyades, the lowest-mass brown dwarf companion with a dynamical mass, and the fourth-lowest-mass benchmark substellar companion after  $\beta$  Pic b (Brandt et al. 2021a),  $\beta$  Pic c (Nowak et al. 2020; Brandt et al. 2021a), and HR 8799 e (Brandt et al. 2021b). We also identified a wide-separation ( $1837''$ ) comoving low-mass star or high-mass brown dwarf, HIP 21152 C, that is likely bound with a model-inferred mass of  $73 \pm 7 M_{\text{Jup}}$ .

We investigated the atmospheric properties of HIP 21152 B using new reductions of the SPHERE/IFS spectrum from Bonavita et al. (2022), a new 2022 CHARIS spectrum, and both SPHERE/IRDIS  $K_{12}$  and Keck/NIRC2  $L'$  photometry. Comparing the observed spectra against spectral standards yields a spectral type of  $T0 \pm 1$ . The best-fit model atmosphere from Saumon & Marley (2008) has  $T_{\text{eff}} = 1400 \text{ K}$ ,  $\log g = 4.5$ , and  $f_{\text{sed}} = 2$ . This is consistent with the companion residing at the L/T transition. We additionally performed a suite of



retrievals with the `Helios-r2` models. The retrievals produce a similar temperature to the grid-based comparison of 1400–1600 K, while the retrieved surface gravity is slightly higher ( $\log g \sim 4.9\text{--}5.4$ ).

This companion joins a small but growing list of benchmark companions with well-constrained dynamical masses and independent age determinations (see Franson et al. 2022 for a recent compilation). The modest difference between the model-predicted mass and the dynamical mass of this companion echoes other cases where benchmark companions are somewhat less massive than model-inferred masses (e.g., Dupuy et al. 2009; Beatty et al. 2018; Rickman et al. 2020). Additionally, it follows the trend suggested in Brandt et al. (2021c) of younger, lower-mass benchmark brown dwarfs being systematically undermassive. These discrepancies underscore the need for additional benchmark companions to empirically test and calibrate substellar evolutionary models. As demonstrated by the discovery of HIP 21152 B, astrometric accelerations offer a promising avenue forward.

We thank Garreth Ruane, Bin Ren, Nicole Wallack, and Dimitri Mawet for helpful discussions regarding the reduction of VVC ADI sequences. We thank Masayuki Kuzuhara and Thayne Currie for helpful discussions about this object and for sharing their astrometry and RVs. K.F. acknowledges support from the National Science Foundation Graduate Research Fellowship Program under grant No. DGE-2137420. B.P.B. acknowledges support from the National Science Foundation grant No. AST-1909209, NASA Exoplanet Research Program grant No. 20-XRP20\_2-0119, and the Alfred P. Sloan Foundation. K.M. acknowledges funding by the Science and Technology Foundation of Portugal (FCT), grant Nos. PTDC/FIS-AST/28731/2017 and UIDB/00099/2020. This work was supported by a NASA Keck PI Data Award, administered by the NASA Exoplanet Science Institute.

This work has made use of data from the European Space Agency (ESA) space mission Gaia. Gaia data are being processed by the Gaia Data Processing and Analysis Consortium (DPAC). Funding for the DPAC is provided by national institutions, in particular the institutions participating in the Gaia MultiLateral Agreement (MLA). The Gaia mission website is <https://www.cosmos.esa.int/gaia>. The Gaia archive website is <https://archives.esac.esa.int/gaia>. This publication makes use of data products from the Two Micron All Sky Survey, which is a joint project of the University of Massachusetts and the Infrared Processing and Analysis Center/California Institute of Technology, funded by the National Aeronautics and Space Administration and the National Science Foundation. This publication makes use of data products from the Wide-field Infrared Survey Explorer, which is a joint project of the University of California, Los Angeles, and the Jet Propulsion Laboratory/California Institute of Technology, funded by the National Aeronautics and Space Administration. The Pan-STARRS1 Surveys (PS1) have been made possible through contributions of the Institute for Astronomy, the University of Hawaii, the Pan-STARRS Project Office, the Max-Planck Society and its participating institutes, the Max Planck Institute for Astronomy, Heidelberg and the Max Planck Institute for Extraterrestrial Physics, Garching, The Johns Hopkins University, Durham University, the University of Edinburgh, Queen’s University Belfast, the Harvard-Smithsonian Center for Astrophysics, the Las

Cumbres Observatory Global Telescope Network Incorporated, the National Central University of Taiwan, the Space Telescope Science Institute, the National Aeronautics and Space Administration under grant No. NNX08AR22G issued through the Planetary Science Division of the NASA Science Mission Directorate, the National Science Foundation under grant No. AST-1238877, the University of Maryland, and Eotvos Lorand University (ELTE). This research has made use of the SIMBAD database and the VizieR catalog access tool, CDS, Strasbourg, France. This work has made use of the SPHERE Data Centre, jointly operated by OSUG/IPAG (Grenoble), PYTHEAS/LAM/CeSAM (Marseille), OCA/Lagrange (Nice) and Observatoire de Paris/LESIA (Paris) and supported by a grant from Labex OSUG@2020 (Investissements d’avenir—ANR10 LABX56). This work has benefited from The UltracoolSheet at <http://bit.ly/UltracoolSheet>, maintained by Will Best, Trent Dupuy, Michael Liu, Rob Siverd, and Zhoujian Zhang, and developed from compilations by Dupuy & Liu (2012), Dupuy & Kraus (2013), Liu et al. (2016), and Best et al. (2018, 2021).

The development of SCEXAO is supported by the Japan Society for the Promotion of Science (Grant-in-Aid for Research #23340051, #26220704, #23103002, #19H00703, #19H00695 and #21H04998), the Subaru Telescope, the National Astronomical Observatory of Japan, the Astrobiology Center of the National Institutes of Natural Sciences, Japan, the Mt Cuba Foundation and the Heising-Simons Foundation. CHARIS was built at Princeton University under a Grant-in-Aid for Scientific Research on Innovative Areas from MEXT of the Japanese government (#23103002). Data presented herein were obtained at the W. M. Keck Observatory from telescope time allocated to the National Aeronautics and Space Administration through the agency’s scientific partnership with the California Institute of Technology and the University of California. The Observatory was made possible by the generous financial support of the W. M. Keck Foundation.

The authors wish to recognize and acknowledge the very significant cultural role and reverence that the summit of Maunakea has always had within the indigenous Hawaiian community. We are most fortunate to have the opportunity to conduct observations from this mountain.

*Facilities:* Keck:II (NIRC2), VLT:Melipal (SPHERE), Subaru (SCEXAO/CHARIS), Smith (Tull Coudé spectrograph).

*Software:* VIP (Gomez Gonzalez et al. 2017), pyKLIP (Wang et al. 2015), orvara (Brandt et al. 2021d), ccdproc (Craig et al. 2017), photutils (Bradley et al. 2019), astropy (Astropy Collaboration et al. 2013, 2018), pandas (McKinney 2010), matplotlib (Hunter 2007), numpy (Harris et al. 2020), scipy (Virtanen et al. 2020), emcee (Foreman-Mackey et al. 2013), corner (Foreman-Mackey 2016), lightkurve (Lightkurve Collaboration et al. 2018), Helios-r2 (Kitzmann et al. 2020), scikit-learn (Pedregosa et al. 2011).

## Appendix A

### CHARIS Astrometric Calibration with HIP 55507

We calibrate our 2022 February CHARIS astrometry of HIP 21152 AB using the 0<sup>h</sup>75 visual binary HIP 55507. We targeted HIP 55507 with CHARIS on UT 2022 February 27 during the same run we observed HIP 21152. HIP 55507 was previously imaged with Keck/NIRC2 on UT 2012 January 7 and 2015 May 29 (PI: Justin Crepp) as part of the TRENDS

**Table 9**  
Astrometry of HIP 55507 B

Filter	Date (UT)	Epoch (UT)	Separation (mas)	PA (°)	Instrument
<i>H</i>	2012 Jan 07	2012.016	475.8 ± 1.4	292.40 ± 0.12	NIRC2
<i>K'</i>	2012 Jan 07	2012.016	475.3 ± 1.4	292.65 ± 0.12	NIRC2
<i>K</i> <sub>cont</sub>	2015 May 29	2015.406	549.7 ± 1.4	274.79 ± 0.11	NIRC2
<i>J</i> <sub>cont</sub>	2015 May 29	2015.406	548.6 ± 1.4	274.67 ± 0.11	NIRC2
<i>K</i> <sub>s</sub>	2021 Dec 21	2021.970	748 ± 5	254.04 ± 0.20	NIRC2

**Table 10**  
HIP 55507 B Orbit Fit Results

Parameter	Median ± 1σ	95.4% C.I.	Prior
Fitted Parameters			
$M_{\text{comp}} (M_{\text{Jup}})$	98 <sup>+13</sup> <sub>-11</sub>	(78, 126)	1/ $M_{\text{comp}}$ (log-flat)
$M_{\text{host}} (M_{\odot})$	0.79 <sup>+0.12</sup> <sub>-0.10</sub>	(0.61, 1.05)	0.7 ± 0.2 $M_{\odot}$ (Gaussian)
$a$ (au)	34 <sup>+7</sup> <sub>-4</sub>	(26, 51)	1/ $a$ (log-flat)
$i$ (°)	117.5 ± 1.5	(114.6, 120.5)	sin( $i$ ), 0° < $i$ < 180°
$\sqrt{e} \sin \omega$	-0.43 <sup>+0.17</sup> <sub>-0.14</sub>	(-0.66, -0.03)	Uniform
$\sqrt{e} \cos \omega$	-0.35 <sup>+0.10</sup> <sub>-0.08</sub>	(-0.50, -0.13)	Uniform
$\Omega$ (°)	219.9 ± 2.2	(215.9, 224.3)	Uniform
$\lambda_{\text{ref}}$ (°) <sup>a</sup>	253 ± 7	(240, 266)	Uniform
Parallax (mas)	39.319 ± 0.015	(39.288, 39.349)	39.3187 ± 0.0147 mas (Gaussian)
$\mu_{\alpha}$ (mas yr <sup>-1</sup> )	-200.60 <sup>+0.32</sup> <sub>-0.37</sub>	(-201.38, -200.01)	Uniform
$\mu_{\delta}$ (mas yr <sup>-1</sup> )	-139.0 <sup>+0.4</sup> <sub>-0.5</sub>	(-140.0, -138.2)	Uniform
RV jitter $\sigma_{\text{RV}}$ (m s <sup>-1</sup> )	4.4 <sup>+0.9</sup> <sub>-0.7</sub>	(3.2, 6.5)	1/ $\sigma_{\text{RV}}$ (log-flat), $\sigma_{\text{RV}} \in (0, 1000 \text{ m s}^{-1})$
Derived Parameters			
$P$ (yr)	210 <sup>+80</sup> <sub>-50</sub>	(130, 420)	...
$e$	0.31 <sup>+0.12</sup> <sub>-0.10</sub>	(0.13, 0.54)	...
$\omega$ (°)	231 <sup>+14</sup> <sub>-19</sub>	(185, 257)	...
$T_0$ (JD)	2450600 <sup>+1400</sup> <sub>-2000</sub>	(2446000, 2453300)	...
$q (=M_{\text{comp}}/M_{\text{host}})$	0.118 <sup>+0.015</sup> <sub>-0.013</sub>	(0.095, 0.150)	...
$\rho$ on 2022.159 (mas)	759 ± 4	(750, 767)	...
$\theta$ on 2022.159 (°)	253.08 ± 0.15	(252.78, 253.39)	...

**Note.**

<sup>a</sup> Mean longitude at the reference epoch of 2010.0.

survey (Gonzales et al. 2020). We also obtained coronagraphic adaptive optics imaging of this system with Keck/NIRC2 on UT 2021 December 21. HIP 55507 additionally has Keck/HIRES radial velocities from 2009 to 2013, reported in Butler et al. (2017). To correct for small but potentially significant orbital motion between the 2021 December imaging and the 2022 February CHARIS data set, we perform a joint orbit fit with `orvara` of the relative astrometry, RVs, and HGCA acceleration ( $\chi^2 = 674$ , or  $26\sigma$  with 2 degrees of freedom).

Basic image reduction is carried out following the description in Section 4.1. To correct for geometric distortions, we apply the solution from Service et al. (2016) for imaging after the NIRC2 camera and adaptive optics system were realigned on UT 2015 April 13 and the solution from Yelda et al. (2010) for imaging prior to that date. We fit 2D Gaussians to the positions of the host star and the binary companion in each exposure to measure astrometry from the calibrated images. The individual exposures within a sequence are weighted by their total integration times. We also incorporate the uncertainty in the distortion solution, north alignment, and plate scale

from Service et al. (2016) or Yelda et al. (2010), following Franson et al. (2022). For the 2021 December imaging with the 600 mas Lyot coronagraph, we adopt a noise floor of ±5 mas in separation and ±0.2° in position angle to account for potential systematic offsets in the host-star position behind the partially transparent coronagraph (see Bowler et al. 2018). The resulting astrometry is listed in Table 9.

We perform a joint orbit fit of HIP 55507 A with `orvara` to obtain the predicted companion position on UT 2022 February 28 for anchoring the CHARIS astrometry. Our fit uses 100 walkers, 20 temperatures, and  $5 \times 10^5$  total steps. We discard the first 50% of each chain as burn-in. The priors for the orbit fit of HIP 21152 B (see Table 4) are adopted except for host-star mass, for which we use a prior of  $0.7 \pm 0.2 M_{\odot}$  based on the estimate in Anders et al. (2022), and parallax, which was measured to be  $39.3187 \pm 0.0147$  mas from Gaia EDR3. The orbit elements from the fit are shown in Table 10. Upon propagating the position to the UT 2022 February 28 epoch, the orbit fit predicts the companion to have a separation of  $\rho = 759 \pm 4$  mas and a position angle of  $\theta = 253.08 \pm 0.15$ .

The CHARIS sequence of HIP 55507 that we obtained consists of 30 frames in low-resolution ( $R \sim 20$ ), broadband ( $1.15 - 2.39 \mu\text{m}$ ) mode with integration times of 30 s and the 113 mas Lyot coronagraph. The CHARIS plate scale has been found to be stable over long periods, so we adopt the value of  $16.15 \pm 0.1 \text{ mas spaxel}^{-1}$  from M. Chen et al. 2022 (in preparation). We measure astrometry using the same procedure from Section 4.2 and find a separation of  $758 \pm 6 \text{ mas}$  and a position angle of  $252^\circ.2 \pm 0^\circ.2$ . While the separation value is consistent with the prediction, the position angle is slightly lower, with a difference of  $0^\circ.9 \pm 0^\circ.3$ . To account for this slight offset in north alignment, we add this value to the position angle of the HIP 21152 B CHARIS measurement (Section 4.2).

## Appendix B Converting W1 to $L'$ Magnitudes

To convert W1 magnitudes to  $L'$  magnitudes in constructing the CMD (Section 6.2.1), we develop a relation between the absolute W1 magnitude  $M_{W1}$  and  $L' - W1$  using the 35 field-age substellar objects in Filippazzo et al. (2015) with parallaxes and both  $L'$  and W1 photometry. We fit a fourth-order polynomial of the form  $P(x) = \sum_{i=0}^4 c_i x^i$ , where  $x = M_{W1}$  and  $P(x) = L' - W1$ . The fit produced coefficients of  $c_0 = -11.449$ ,  $c_1 = 3.0429$ ,  $c_2 = -0.26004$ , and  $c_3 = 6.7306 \times 10^{-3}$ , and has an rms of 0.128. The absolute W1 magnitudes of the objects used in the fit range from  $8.9 \text{ mag} \leq M_{W1} \leq 17.1 \text{ mag}$ . The relation is shown in Figure 15.

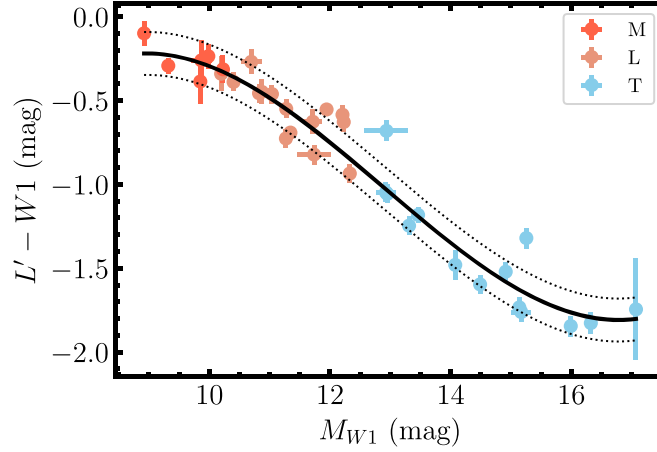


**Figure 15.**  $L' - W1$  as a function of  $M_{W1}$  for field-age M dwarfs (orange), L dwarfs (light orange), and T dwarfs (blue) from Filippazzo et al. (2015). The black line denotes a fourth-order polynomial fit to the objects' magnitudes and the dotted lines show the rms of the relation.



### Appendix C Grid-based Model Comparison (Reduction 1)

Here, we show the results of performing the model comparison with Saumon & Marley (2008) atmospheric models using Reduction 1 for the SPHERE/IFS spectrum (see Section 6.2.2 for details on the model comparison). Figure 16 displays reduced chi-square ( $\chi_\nu^2$ ) and goodness-of-fit ( $G$ ) statistics (analogous to Figure 11). Unlike with Reduction 2, the best-fitting atmospheric model is dependent on the metric used.  $\chi_\nu^2$  yields a minimum around 1600 K, with the best-fit spectrum having  $T_{\text{eff}} = 1500$  K,  $\log g = 4.5$ , and  $f_{\text{sed}} = 3$ . The

best-fit model produced by the  $G$  statistic has  $T_{\text{eff}} = 1400$  K,  $\log g = 4.5$ , and  $f_{\text{sed}} = 2$ , which matches the best-fit model with Reduction 2 of the IFS spectrum (Section 6.2.2). The  $\chi_\nu^2$  metric preferring models with higher  $T_{\text{eff}}$  and  $f_{\text{sed}}$  indicates that Reduction 1 drives effective temperature and sedimentation efficiency upward. As  $G$  weights the companion’s photometry more heavily, this effect is minimized for that metric. This can be seen in Figure 17, which shows the two best-fit model spectra. The  $\chi_\nu^2$  metric (green curve) better captures the enhanced flux in the  $J$  band from Reduction 1, but it departs from the compared to the 1400 K model.

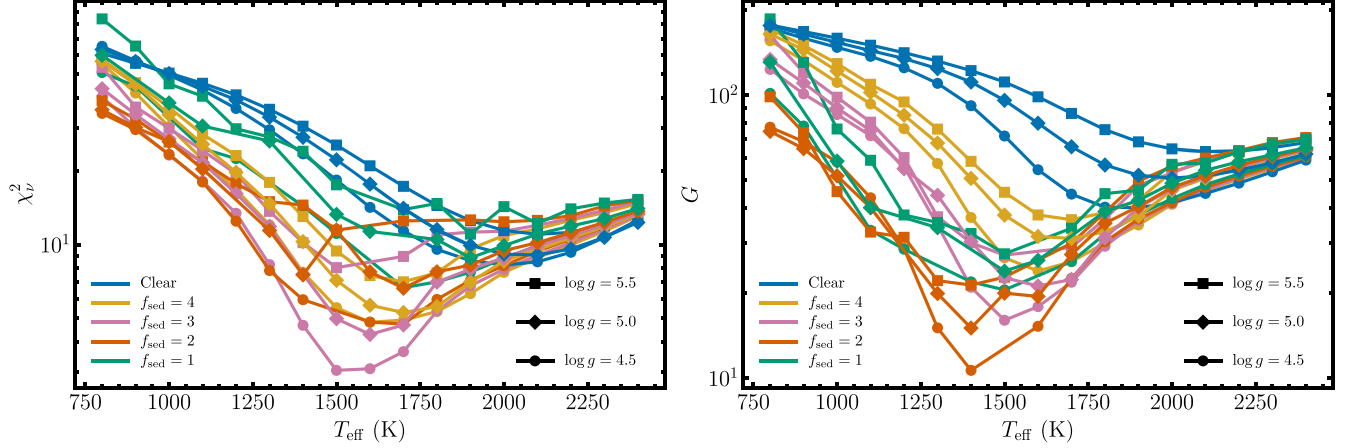


**Figure 16.** Reduced chi-square ( $\chi_\nu^2$ , left) and goodness-of-fit ( $G$ , right) values for model spectra from Saumon & Marley (2008) compared with HIP 21152 B’s spectra and photometry. Here, Reduction 1 is used for the SPHERE/IFS spectrum. The two metrics produce different best-fitting spectra.  $\chi_\nu^2$  yields a best-fit spectrum with  $T_{\text{eff}} = 1500$  K,  $\log g = 4.5$ , and  $f_{\text{sed}} = 3$ , while  $G$  gives a best-fitting spectrum with  $T_{\text{eff}} = 1400$  K,  $\log g = 4.5$ , and  $f_{\text{sed}} = 2$ .

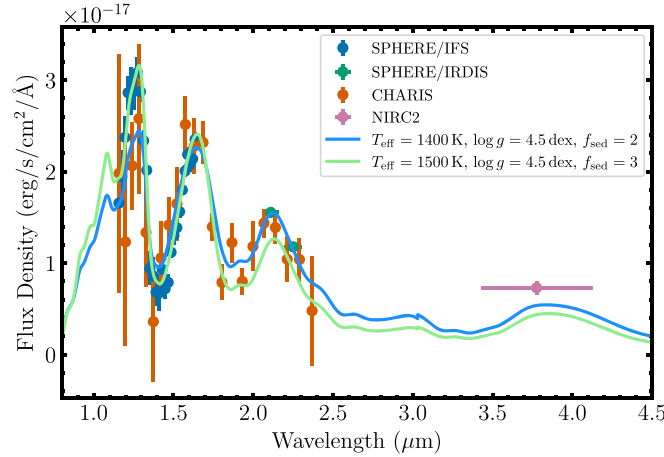


**Figure 17.** Comparison of best-fitting model spectra with HIP 21152 B’s spectra and photometry. The two curves show the best-fitting spectra based on  $\chi_\nu^2$  (light green) and  $G$  (blue). Here, Reduction 1 is used for the SPHERE/IFS spectrum. The model spectra have been smoothed to a resolving power of  $R = 25$ .

### Appendix D Atmospheric Retrieval (Reduction 1)

Here, we show the retrieval results using Reduction 1 for the SPHERE/IFS spectrum instead of Reduction 2 (see Section 6.2.3 for details on the retrievals). Table 13 shows the posteriors on the retrieved parameters. The CHARIS-only retrieval is shown for completeness; it is identical to the version in Table 12. These retrievals produce significantly higher effective temperatures of  $T_{\text{eff}} \sim 1800$  K for the IFS-only version and  $T_{\text{eff}} \sim 1900$  K for the IFS + CHARIS +

Photometry retrievals. These values are inconsistent with the effective temperature derived from the Stefan–Boltzmann relation ( $1300 \pm 50$  K) and the effective temperature from the CHARIS-only retrieval of  $\sim 1400$  K. We detect water in all retrievals, with mixing ratios  $x_{\text{H}_2\text{O}} \sim 10^{-3}$ – $10^{-2}$ . FeH and TiH are detected in some versions of the retrieval models or included data sets, with small mixing ratios  $\sim 10^{-9}$ – $10^{-6}$ . Figure 18 shows the best-fit spectra for the five retrieval versions against the companion’s spectra and photometry (analogous to Figure 13).

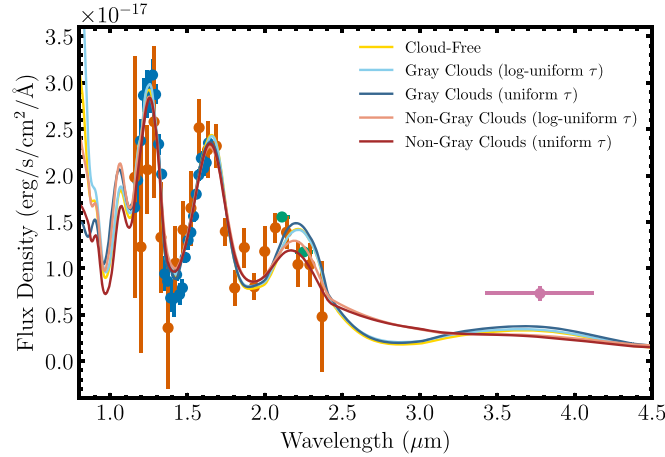


**Figure 18.** Spectra and photometry of HIP 21152 B compared with the best-fit retrievals from the five retrieval versions we consider. These retrievals incorporate all available data (IFS + CHARIS + Photometry) and adopt Reduction 1 for the SPHERE/IFS spectrum. The retrieved spectra are smoothed to a resolving power of  $R = 25$ .

## Appendix E Additional Reduction of Keck/NIRC2 Imaging

Here, we apply an independent reduction of the 2021 December  $L'$ -band NIRC2 observation of HIP 21152 using an alternative framework to further assess the significance of the detection from this ADI sequence. We developed a custom implementation of the PATCH COvariances (PACO) algorithm (Flasseur et al. 2018), which uses spatially local models of the expected speckle noise statistics in a maximum-likelihood estimator to find the best-fit flux estimate of a potential off-axis point source. Fixed spatial patches centered at a pixel  $\phi_t$  in the  $t$ th frame, and spanning the time axis of the ADI image cube, are used to construct a mean vector and covariance matrix,  $\mathbf{m}_{\phi_t}$  and  $\hat{\mathbf{C}}_{\phi_t}$ . These parameterize a multivariate Gaussian distribution that describes the speckle noise local to  $\phi_t$ . The set of spatial patches centered at pixels  $\phi_{\{1:T\}}$ , determined by the parallactic rotation of the ADI sequence, each contain an off-axis point source if it were located at  $\phi_1$  in the first frame. The maximum-likelihood estimate of a potential point source is found by minimizing the quadratic cost function

$$\hat{\alpha}_{\phi_1} = \arg \min_{\alpha} \sum_{t=1}^T (\mathbf{p}_{\phi_t} - \alpha \mathbf{h} - \mathbf{m}_{\phi_t})^{\top} \hat{\mathbf{C}}_{\phi_t}^{-1} (\mathbf{p}_{\phi_t} - \alpha \mathbf{h} - \mathbf{m}_{\phi_t}), \quad (\text{E1})$$

where  $T$  is the number of frames in the ADI sequence and  $\mathbf{h}$  is a unit-normalized template of the expected signal profile of a point source in the data patch,  $\mathbf{p}_{\phi_t}$ . Equation (E1) has a closed-form solution, and can be solved with linear least-squares. Under this framework, the S/N of a potential source is

$$\text{S/N} = \frac{\hat{\alpha}_{\phi_1}}{\sqrt{\frac{1}{T} \sum_{t=1}^T \mathbf{h}^{\top} \hat{\mathbf{C}}_{\phi_t}^{-1} \mathbf{h}}}. \quad (\text{E2})$$

Our implementation of the PACO algorithm deviates slightly from the original paper. We model the local speckle noise as a multivariate double exponential distribution, which we find is more robust at close separations. This model results in finding the minimum mean absolute error estimate of  $\hat{\alpha}_{\phi_1}$ , but does not permit an analytical solution. We used the `SciPy` implementation of the Levenberg–Marquardt non-linear least-squares algorithm (Virtanen et al. 2020) instead. Additionally, we used the `scikit-learn` implementation of the Ledoit–Wolf covariance shrinkage method (Pedregosa et al. 2011) to estimate each  $\hat{\mathbf{C}}_{\phi_t}$  in lieu of the covariance shrinkage approach proposed by Flasseur et al. (2018). To improve the run-time of our implementation, we process the ADI sequence serially over pixel-width annuli, and parallelize the algorithm for each pixel in the annulus. The choice of  $\mathbf{h}$  is instrument specific. For the  $L'$ -band filter with NIRC2, we use a symmetric 2D Gaussian profile with a 3.5 pixel standard deviation. The size of the local spatial patch centered at each pixel,  $\phi_t$ , must also be tuned. We find that using a square patch with a width of 8 px works well for most data sets.

Using our implementation of PACO, we were able to formally recover HIP 21152 B at an S/N of 24.7, as determined using Equation (E2). However, we note that the S/N values across the image show correlated noise features with S/N levels up to  $\pm 10$ . To be consistent with the reduction produced with the PCA-based algorithm in Section 4.1, we also calculate the S/N with the standard empirical approach, using the rms flux value in an annular section at the separation of HIP 21152 B, which gives an S/N value of 7.8 that is comparable to the companion’s S/N from the PCA reduction (Section 4.1). Figure 19 shows the PACO reduction of the Keck/NIRC2 imaging.

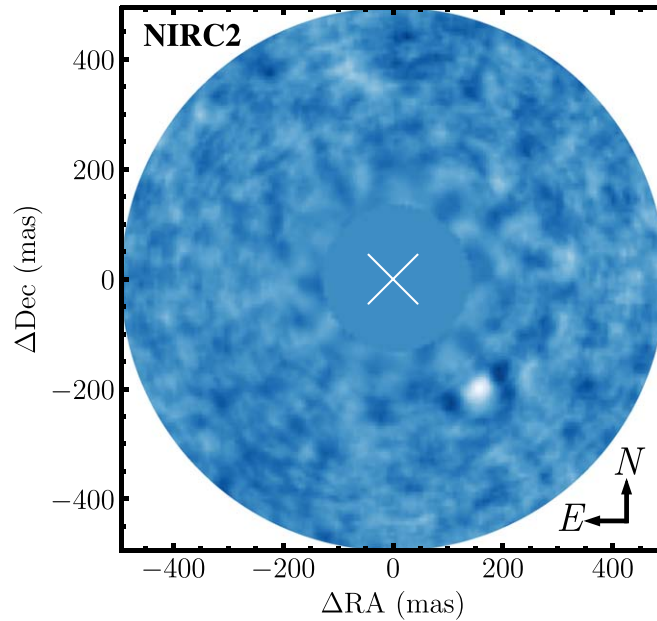


**Figure 19.** Keck/NIRC2  $L'$  imaging of HIP 21152 B, reduced using the PACO algorithm. The frame is oriented so that north is up and east is to the left. We detect HIP 21152 B with a S/N of 7.8 using PACO.



**Table 11**  
SPHERE/IFS Spectrum

Reduction 1			Reduction 2		
$\lambda$ ( $\mu\text{m}$ )	$f_{\lambda} \times 10^{-17}$ ( $\text{erg/s/cm}^2/\text{\AA}$ )	$\sigma_{f_{\lambda}} \times 10^{-17}$ ( $\text{erg/s/cm}^2/\text{\AA}$ )	$\lambda$ ( $\mu\text{m}$ )	$f_{\lambda} \times 10^{-17}$ ( $\text{erg/s/cm}^2/\text{\AA}$ )	$\sigma_{f_{\lambda}} \times 10^{-17}$ ( $\text{erg/s/cm}^2/\text{\AA}$ )
0.957	1.0	0.5	0.982	1.5	0.6
0.972	1.4	0.3	1.002	1.1	0.5
0.987	2.2	0.4	1.023	1.7	0.4
1.002	2.2	0.4	1.043	0.9	0.4
1.018	1.88	0.10	1.064	0.9	0.4
1.034	1.9	0.4	1.084	1.6	0.3
1.051	2.0	0.5	1.105	1.5	0.3
1.068	1.7	0.4	1.125	1.4	0.3
1.086	1.2	0.5	1.146	1.6	0.3
1.104	1.2	0.3	1.166	1.9	0.3
1.122	1.4	0.3	1.187	1.87	0.23
1.140	1.6	0.4	1.207	2.05	0.17
1.159	1.7	0.4	1.228	2.04	0.18
1.178	1.9	0.3	1.248	2.45	0.19
1.197	2.37	0.23	1.269	2.66	0.15
1.216	2.86	0.18	1.289	2.51	0.14
1.235	2.9	0.3	1.310	1.99	0.14
1.255	2.88	0.20	1.331	1.72	0.15
1.274	3.08	0.17	1.351	1.22	0.15
1.294	2.87	0.11	1.372	0.75	0.19
1.314	2.34	0.11	1.392	0.65	0.17
1.333	2.02	0.03	1.413	0.82	0.17
1.353	0.94	0.18	1.433	1.00	0.13
1.372	0.86	0.21	1.454	1.10	0.09
1.391	0.68	0.15	1.474	1.24	0.10
1.411	0.67	0.20	1.495	1.37	0.07
1.430	0.93	0.06	1.515	1.54	0.05
1.449	0.72	0.11	1.536	1.69	0.06
1.467	0.79	0.09	1.556	1.90	0.05
1.486	1.12	0.06	1.577	2.06	0.05
1.504	1.30	0.10	1.597	2.15	0.06
1.522	1.39	0.05	1.618	2.17	0.05
1.539	1.56	0.06	1.638	2.15	0.06
1.556	1.80	0.03	...	...	...
1.573	2.01	0.06	...	...	...
1.589	2.19	0.08	...	...	...
1.605	2.08	0.08	...	...	...
1.621	2.14	0.12	...	...	...
1.636	2.35	0.08	...	...	...

**Table 12**  
Retrieved Parameters of HIP 21152 B (Reduction 2)

Model	Parameter	IFS	CHARIS	IFS + CHARIS + Photometry
Cloud-free	$\log g$	$5.1^{+0.5}_{-0.7}$	$5.0^{+0.6}_{-0.7}$	$5.3^{+0.4}_{-0.6}$
Gray clouds (log-uniform $\tau$ )	$\log g$	$5.0^{+0.6}_{-0.7}$	$4.9^{+0.6}_{-0.7}$	$5.3^{+0.4}_{-0.5}$
Gray clouds (uniform $\tau$ )	$\log g$	$4.9^{+0.6}_{-0.7}$	$5.0^{+0.6}_{-0.7}$	$5.3^{+0.4}_{-0.4}$
Nongray clouds (log-uniform $\tau$ )	$\log g$	$4.9^{+0.6}_{-0.7}$	$4.9^{+0.7}_{-0.7}$	$5.2^{+0.4}_{-0.5}$
Nongray clouds (uniform $\tau$ )	$\log g$	$4.9^{+0.6}_{-0.7}$	$4.9^{+0.6}_{-0.7}$	$5.2^{+0.5}_{-0.5}$
Cloud-free	$R$	$0.74^{+0.21}_{-0.14}$	$0.8^{+0.5}_{-0.3}$	$0.68^{+0.18}_{-0.09}$
Gray clouds (log-uniform $\tau$ )	$R$	$0.72^{+0.31}_{-0.17}$	$0.8^{+0.4}_{-0.3}$	$0.66^{+0.13}_{-0.09}$
Gray clouds (uniform $\tau$ )	$R$	$0.70^{+0.32}_{-0.16}$	$0.66^{+0.39}_{-0.20}$	$0.54^{+0.08}_{-0.09}$
Nongray clouds (log-uniform $\tau$ )	$R$	$0.77^{+0.28}_{-0.19}$	$0.76^{+0.43}_{-0.25}$	$0.67^{+0.15}_{-0.11}$
Nongray clouds (uniform $\tau$ )	$R$	$0.71^{+0.37}_{-0.18}$	$0.73^{+0.41}_{-0.23}$	$0.65^{+0.12}_{-0.10}$
Cloud-free	$d$	$43.27^{+0.04}_{-0.04}$	$43.27^{+0.04}_{-0.04}$	$43.27^{+0.04}_{-0.04}$
Gray clouds (log-uniform $\tau$ )	$d$	$43.27^{+0.04}_{-0.04}$	$43.27^{+0.04}_{-0.04}$	$43.27^{+0.04}_{-0.04}$
Gray clouds (uniform $\tau$ )	$d$	$43.27^{+0.04}_{-0.04}$	$43.27^{+0.04}_{-0.04}$	$43.27^{+0.04}_{-0.04}$
Nongray clouds (log-uniform $\tau$ )	$d$	$43.27^{+0.04}_{-0.04}$	$43.27^{+0.04}_{-0.04}$	$43.27^{+0.04}_{-0.04}$
Nongray clouds (uniform $\tau$ )	$d$	$43.27^{+0.04}_{-0.04}$	$43.27^{+0.04}_{-0.04}$	$43.27^{+0.04}_{-0.04}$
Cloud-free	$T_{\text{eff}}$	$1460^{+180}_{-140}$	$1360^{+290}_{-210}$	$1480^{+100}_{-140}$
Gray clouds (log-uniform $\tau$ )	$T_{\text{eff}}$	$1500^{+250}_{-200}$	$1370^{+320}_{-220}$	$1500^{+100}_{-110}$
Gray clouds (uniform $\tau$ )	$T_{\text{eff}}$	$1500^{+200}_{-190}$	$1480^{+300}_{-270}$	$1630^{+130}_{-100}$
Nongray clouds (log-uniform $\tau$ )	$T_{\text{eff}}$	$1460^{+240}_{-170}$	$1400^{+300}_{-230}$	$1490^{+110}_{-120}$
Nongray clouds (uniform $\tau$ )	$T_{\text{eff}}$	$1500^{+220}_{-220}$	$1420^{+280}_{-240}$	$1520^{+120}_{-110}$
Cloud-free	$\log \text{H}_2\text{O}$	$-3.4^{+1.5}_{-0.5}$	$-3.6^{+0.8}_{-0.6}$	$-3.61^{+0.24}_{-0.31}$
Gray clouds (log-uniform $\tau$ )	$\log \text{H}_2\text{O}$	$-2.4^{+0.8}_{-1.3}$	$-3.6^{+0.9}_{-0.7}$	$-3.58^{+0.24}_{-0.27}$
Gray clouds (uniform $\tau$ )	$\log \text{H}_2\text{O}$	$-2.4^{+0.8}_{-1.3}$	$-3.4^{+1.0}_{-0.8}$	$-3.4^{+0.5}_{-0.3}$
Nongray clouds (log-uniform $\tau$ )	$\log \text{H}_2\text{O}$	$-2.8^{+1.1}_{-1.2}$	$-3.6^{+0.9}_{-0.6}$	$-3.61^{+0.29}_{-0.29}$
Nongray clouds (uniform $\tau$ )	$\log \text{H}_2\text{O}$	$-2.2^{+0.7}_{-1.3}$	$-3.5^{+1.0}_{-0.7}$	$-3.59^{+0.33}_{-0.29}$
Cloud-free	$\log K$	...	...	$-8.9^{+1.9}_{-1.8}$
Gray clouds (log-uniform $\tau$ )	$\log K$	...	...	$-8.7^{+1.9}_{-1.9}$
Gray clouds (uniform $\tau$ )	$\log K$	...	...	$-8.6^{+2.0}_{-1.9}$
Nongray clouds (log-uniform $\tau$ )	$\log K$	...	...	$-8.7^{+1.8}_{-1.9}$
Nongray clouds (uniform $\tau$ )	$\log K$	...	...	$-8.8^{+1.9}_{-1.8}$
Cloud-free	$\log \text{CrH}$	$-9.5^{+1.5}_{-1.4}$	...	$-9.8^{+1.3}_{-1.3}$
Gray clouds (log-uniform $\tau$ )	$\log \text{CrH}$	$-9.1^{+1.8}_{-1.6}$	...	$-9.6^{+1.2}_{-1.3}$
Gray clouds (uniform $\tau$ )	$\log \text{CrH}$	$-9.1^{+1.9}_{-1.6}$	...	$-9.5^{+1.4}_{-1.4}$
Nongray clouds (log-uniform $\tau$ )	$\log \text{CrH}$	$-9.4^{+1.8}_{-1.5}$	...	$-9.7^{+1.3}_{-1.3}$
Nongray clouds (uniform $\tau$ )	$\log \text{CrH}$	$-9.0^{+1.9}_{-1.7}$	...	$-9.7^{+1.3}_{-1.3}$
Cloud-free	$\log \text{FeH}$	$-9.5^{+1.7}_{-1.4}$	$-8.7^{+1.6}_{-1.8}$	$-9.8^{+1.3}_{-1.3}$
Gray clouds (log-uniform $\tau$ )	$\log \text{FeH}$	$-9.0^{+2.0}_{-1.7}$	$-8.6^{+1.6}_{-1.8}$	$-9.7^{+1.3}_{-1.3}$
Gray clouds (uniform $\tau$ )	$\log \text{FeH}$	$-9.1^{+2.0}_{-1.7}$	$-8.6^{+1.8}_{-1.9}$	$-9.6^{+1.4}_{-1.4}$
Nongray clouds (log-uniform $\tau$ )	$\log \text{FeH}$	$-9.3^{+2.0}_{-1.5}$	$-8.5^{+1.6}_{-1.9}$	$-9.6^{+1.3}_{-1.3}$
Nongray clouds (uniform $\tau$ )	$\log \text{FeH}$	$-8.9^{+2.0}_{-1.7}$	$-8.6^{+1.7}_{-1.9}$	$-9.7^{+1.3}_{-1.3}$
Cloud-free	$\log \text{TiH}$	...	$-8.9^{+1.6}_{-1.7}$	$-10.0^{+1.2}_{-1.2}$
Gray clouds (log-uniform $\tau$ )	$\log \text{TiH}$	...	$-8.9^{+1.7}_{-1.7}$	$-9.9^{+1.2}_{-1.2}$
Gray clouds (uniform $\tau$ )	$\log \text{TiH}$	...	$-8.8^{+1.7}_{-1.7}$	$-9.6^{+1.4}_{-1.3}$
Nongray clouds (log-uniform $\tau$ )	$\log \text{TiH}$	...	$-8.9^{+1.7}_{-1.7}$	$-9.9^{+1.2}_{-1.2}$
Nongray clouds (uniform $\tau$ )	$\log \text{TiH}$	...	$-9.0^{+1.7}_{-1.7}$	$-9.9^{+1.3}_{-1.2}$
Cloud-free	$\log p_t$	...	...	...
Gray clouds (log-uniform $\tau$ )	$\log p_t$	$-0.1^{+1.0}_{-1.0}$	$-0.1^{+1.1}_{-1.1}$	$-0.0^{+1.0}_{-1.1}$
Gray clouds (uniform $\tau$ )	$\log p_t$	$0.2^{+0.8}_{-0.9}$	$0.7^{+0.6}_{-1.0}$	$1.0^{+0.4}_{-0.7}$
Nongray clouds (log-uniform $\tau$ )	$\log p_t$	$-0.1^{+1.0}_{-1.0}$	$-0.1^{+1.0}_{-1.1}$	$0.1^{+1.0}_{-1.1}$
Nongray clouds (uniform $\tau$ )	$\log p_t$	$0.3^{+0.7}_{-0.7}$	$0.7^{+0.6}_{-0.9}$	$0.0^{+1.0}_{-1.1}$
Cloud-free	$\log p_b$	...	...	...
Gray clouds (log-uniform $\tau$ )	$\log p_b$	$0.52^{+0.27}_{-0.28}$	$0.50^{+0.29}_{-0.28}$	$0.52^{+0.28}_{-0.29}$

**Table 12**  
(Continued)

Model	Parameter	IFS	CHARIS	IFS + CHARIS + Photometry
Gray clouds (uniform $\tau$ )	$\log p_b$	$0.49^{+0.28}_{-0.28}$	$0.51^{+0.28}_{-0.29}$	$0.52^{+0.28}_{-0.29}$
Nongray clouds (log-uniform $\tau$ )	$\log p_b$	$0.50^{+0.27}_{-0.28}$	$0.52^{+0.28}_{-0.29}$	$0.49^{+0.28}_{-0.28}$
Nongray clouds (uniform $\tau$ )	$\log p_b$	$0.51^{+0.27}_{-0.28}$	$0.50^{+0.28}_{-0.28}$	$0.51^{+0.28}_{-0.28}$
Cloud-free	$\log \tau$	...	...	...
Gray clouds (log-uniform $\tau$ )	$\log \tau$	$-2.2^{+1.7}_{-1.6}$	$-2.0^{+1.5}_{-1.6}$	$-2.7^{+1.4}_{-1.3}$
Gray clouds (uniform $\tau$ )	$\tau$	$2^{+10}_{-8}$	$11^{+5}_{-6}$	$5^{+9}_{-10}$
Nongray clouds (log-uniform $\tau$ )	$\log \tau$	$-2.2^{+1.6}_{-1.6}$	$-2.1^{+1.6}_{-1.6}$	$-2.7^{+1.4}_{-1.3}$
Nongray clouds (uniform $\tau$ )	$\tau$	$5^{+9}_{-8}$	$3^{+10}_{-8}$	$-4^{+4}_{-3}$
Cloud-free	$\log Q_0$	...	...	...
Gray clouds (log-uniform $\tau$ )	$\log Q_0$	...	...	...
Gray clouds (uniform $\tau$ )	$\log Q_0$	...	...	...
Nongray clouds (log-uniform $\tau$ )	$\log Q_0$	$1.0^{+0.6}_{-0.6}$	$1.0^{+0.6}_{-0.6}$	$1.0^{+0.6}_{-0.6}$
Nongray clouds (uniform $\tau$ )	$\log Q_0$	$1.0^{+0.6}_{-0.6}$	$1.0^{+0.6}_{-0.6}$	$1.0^{+0.6}_{-0.6}$
Cloud-free	$a_0$	...	...	...
Gray clouds (log-uniform $\tau$ )	$a_0$	...	...	...
Gray clouds (uniform $\tau$ )	$a_0$	...	...	...
Nongray clouds (log-uniform $\tau$ )	$a_0$	$5.0^{+1.1}_{-1.1}$	$5.0^{+1.1}_{-1.1}$	$5.0^{+1.1}_{-1.1}$
Nongray clouds (uniform $\tau$ )	$a_0$	$5.0^{+1.1}_{-1.1}$	$5.0^{+1.1}_{-1.1}$	$4.9^{+1.1}_{-1.1}$
Cloud-free	$\log a$	...	...	...
Gray clouds (log-uniform $\tau$ )	$\log a$	...	...	...
Gray clouds (uniform $\tau$ )	$\log a$	...	...	...
Nongray clouds (log-uniform $\tau$ )	$\log a$	$0.4^{+0.7}_{-0.8}$	$0.3^{+0.8}_{-0.8}$	$0.3^{+0.8}_{-0.7}$
Nongray clouds (uniform $\tau$ )	$\log a$	$0.3^{+0.7}_{-0.7}$	$0.3^{+0.8}_{-0.8}$	$0.2^{+0.8}_{-0.7}$

**Table 13**  
Retrieved Parameters of HIP 21152 B (Reduction 1)

Model	Parameter	IFS	CHARIS	IFS + CHARIS + Photometry
Cloud-free	$\log g$	$5.3^{+0.4}_{-0.7}$	$5.0^{+0.6}_{-0.7}$	$5.4^{+0.4}_{-0.6}$
Gray clouds (log-uniform $\tau$ )	$\log g$	$4.8^{+0.6}_{-0.6}$	$4.9^{+0.6}_{-0.7}$	$5.4^{+0.4}_{-0.6}$
Gray clouds (uniform $\tau$ )	$\log g$	$5.1^{+0.6}_{-0.7}$	$5.0^{+0.6}_{-0.7}$	$5.4^{+0.4}_{-0.5}$
Nongray clouds (log-uniform $\tau$ )	$\log g$	$4.8^{+0.6}_{-0.6}$	$4.9^{+0.7}_{-0.7}$	$5.4^{+0.4}_{-0.6}$
Nongray clouds (uniform $\tau$ )	$\log g$	$5.2^{+0.5}_{-0.7}$	$4.9^{+0.6}_{-0.7}$	$5.4^{+0.4}_{-0.5}$
Cloud-free	$R$	$0.52^{+0.10}_{-0.06}$	$0.8^{+0.5}_{-0.3}$	$0.43^{+0.05}_{-0.04}$
Gray clouds (log-uniform $\tau$ )	$R$	$0.54^{+0.09}_{-0.06}$	$0.8^{+0.4}_{-0.3}$	$0.43^{+0.05}_{-0.04}$
Gray clouds (uniform $\tau$ )	$R$	$0.52^{+0.10}_{-0.06}$	$0.66^{+0.39}_{-0.20}$	$0.43^{+0.05}_{-0.03}$
Nongray clouds (log-uniform $\tau$ )	$R$	$0.54^{+0.10}_{-0.06}$	$0.76^{+0.43}_{-0.25}$	$0.43^{+0.05}_{-0.04}$
Nongray clouds (uniform $\tau$ )	$R$	$0.50^{+0.09}_{-0.06}$	$0.73^{+0.41}_{-0.23}$	$0.42^{+0.05}_{-0.04}$
Cloud-free	$d$	$43.27^{+0.04}_{-0.04}$	$43.27^{+0.04}_{-0.04}$	$43.27^{+0.04}_{-0.04}$
Gray clouds (log-uniform $\tau$ )	$d$	$43.27^{+0.04}_{-0.04}$	$43.27^{+0.04}_{-0.04}$	$43.27^{+0.04}_{-0.04}$
Gray clouds (uniform $\tau$ )	$d$	$43.27^{+0.04}_{-0.04}$	$43.27^{+0.04}_{-0.04}$	$43.27^{+0.04}_{-0.04}$
Nongray clouds (log-uniform $\tau$ )	$d$	$43.27^{+0.04}_{-0.04}$	$43.27^{+0.04}_{-0.04}$	$43.27^{+0.04}_{-0.04}$
Nongray clouds (uniform $\tau$ )	$d$	$43.27^{+0.04}_{-0.04}$	$43.27^{+0.04}_{-0.04}$	$43.27^{+0.04}_{-0.04}$
Cloud-free	$T_{\text{eff}}$	$1790^{+230}_{-130}$	$1360^{+290}_{-210}$	$1890^{+270}_{-110}$
Gray clouds (log-uniform $\tau$ )	$T_{\text{eff}}$	$1780^{+190}_{-130}$	$1370^{+320}_{-220}$	$1890^{+260}_{-110}$
Gray clouds (uniform $\tau$ )	$T_{\text{eff}}$	$1780^{+160}_{-130}$	$1480^{+300}_{-270}$	$1870^{+130}_{-90}$
Nongray clouds (log-uniform $\tau$ )	$T_{\text{eff}}$	$1770^{+200}_{-130}$	$1400^{+300}_{-230}$	$1890^{+250}_{-110}$
Nongray clouds (uniform $\tau$ )	$T_{\text{eff}}$	$1780^{+120}_{-120}$	$1420^{+280}_{-240}$	$1880^{+150}_{-100}$
Cloud-free	$\log \text{H}_2\text{O}$	$-1.8^{+0.5}_{-0.6}$	$-3.6^{+0.8}_{-0.6}$	$-1.9^{+0.5}_{-0.7}$
Gray clouds (log-uniform $\tau$ )	$\log \text{H}_2\text{O}$	$-1.8^{+0.5}_{-0.6}$	$-3.6^{+0.9}_{-0.7}$	$-1.9^{+0.5}_{-0.7}$
Gray clouds (uniform $\tau$ )	$\log \text{H}_2\text{O}$	$-1.8^{+0.4}_{-0.6}$	$-3.4^{+1.0}_{-0.8}$	$-1.9^{+0.5}_{-0.7}$
Nongray clouds (log-uniform $\tau$ )	$\log \text{H}_2\text{O}$	$-1.7^{+0.4}_{-0.6}$	$-3.6^{+0.9}_{-0.6}$	$-1.9^{+0.5}_{-0.7}$

**Table 13**  
(Continued)

Model	Parameter	IFS	CHARIS	IFS + CHARIS + Photometry
Nongray clouds (uniform $\tau$ )	log H <sub>2</sub> O	$-1.8^{+0.4}_{-0.6}$	$-3.5^{+1.0}_{-0.7}$	$-1.9^{+0.5}_{-0.7}$
Cloud-free	log K	$-7.7^{+2.3}_{-2.4}$	...	$-7.3^{+2.3}_{-2.6}$
Gray clouds (log-uniform $\tau$ )	log K	$-7.5^{+2.4}_{-2.5}$	...	$-7.5^{+2.3}_{-2.5}$
Gray clouds (uniform $\tau$ )	log K	$-7.5^{+2.4}_{-2.5}$	...	$-7.5^{+2.3}_{-2.5}$
Nongray clouds (log-uniform $\tau$ )	log K	$-7.5^{+2.4}_{-2.5}$	...	$-7.5^{+2.3}_{-2.5}$
Nongray clouds (uniform $\tau$ )	log K	$-7.5^{+2.3}_{-2.5}$	...	$-7.5^{+2.3}_{-2.5}$
Cloud-free	log CrH	$-9.3^{+1.6}_{-1.5}$	...	$-9.3^{+1.6}_{-1.5}$
Gray clouds (log-uniform $\tau$ )	log CrH	$-9.3^{+1.6}_{-1.5}$	...	$-9.3^{+1.6}_{-1.5}$
Gray clouds (uniform $\tau$ )	log CrH	$-9.3^{+1.6}_{-1.5}$	...	$-9.2^{+1.6}_{-1.5}$
Nongray clouds (log-uniform $\tau$ )	log CrH	$-9.3^{+1.5}_{-1.5}$	...	$-9.3^{+1.6}_{-1.5}$
Nongray clouds (uniform $\tau$ )	log CrH	$-9.2^{+1.5}_{-1.5}$	...	$-9.2^{+1.6}_{-1.6}$
Cloud-free	log FeH	$-8.8^{+1.8}_{-1.8}$	$-8.7^{+1.6}_{-1.8}$	$-8.1^{+1.9}_{-2.2}$
Gray clouds (log-uniform $\tau$ )	log FeH	$-8.6^{+1.9}_{-1.9}$	$-8.6^{+1.6}_{-1.8}$	$-8.0^{+1.8}_{-2.1}$
Gray clouds (uniform $\tau$ )	log FeH	$-8.6^{+1.9}_{-1.9}$	$-8.6^{+1.8}_{-1.9}$	$-8.3^{+1.9}_{-2.0}$
Nongray clouds (log-uniform $\tau$ )	log FeH	$-9.3^{+2.0}_{-1.5}$	$-8.5^{+1.6}_{-1.9}$	$-8.2^{+1.8}_{-2.1}$
Nongray clouds (uniform $\tau$ )	log FeH	$-8.7^{+1.8}_{-1.8}$	$-8.6^{+1.7}_{-1.9}$	$-8.0^{+1.8}_{-2.2}$
Cloud-free	log TiH	$-6.7^{+0.9}_{-2.1}$	$-8.9^{+1.6}_{-1.7}$	$-6.5^{+0.8}_{-1.5}$
Gray clouds (log-uniform $\tau$ )	log TiH	$-6.5^{+0.9}_{-2.0}$	$-8.9^{+1.7}_{-1.7}$	$-6.4^{+0.7}_{-1.4}$
Gray clouds (uniform $\tau$ )	log TiH	$-6.6^{+0.9}_{-2.1}$	...	$-6.5^{+0.8}_{-1.9}$
Nongray clouds (log-uniform $\tau$ )	log TiH	$-6.6^{+0.9}_{-2.2}$	$-8.9^{+1.7}_{-1.7}$	$-6.5^{+0.7}_{-1.4}$
Nongray clouds (uniform $\tau$ )	log TiH	$-6.5^{+0.8}_{-1.9}$	$-9.0^{+1.7}_{-1.7}$	$-6.5^{+0.8}_{-1.9}$
Cloud-free	log $p_t$	...	...	...
Gray clouds (log-uniform $\tau$ )	log $p_t$	$-0.0^{+1.0}_{-1.0}$	$-0.1^{+1.1}_{-1.1}$	$0.1^{+0.9}_{-1.0}$
Gray clouds (uniform $\tau$ )	log $p_t$	$0.2^{+0.8}_{-0.9}$	$0.7^{+0.6}_{-1.0}$	$0.4^{+0.7}_{-0.6}$
Nongray clouds (log-uniform $\tau$ )	log $p_t$	$0.0^{+1.0}_{-1.0}$	$-0.1^{+1.0}_{-1.1}$	$0.1^{+0.9}_{-1.0}$
Nongray clouds (uniform $\tau$ )	log $p_t$	$0.4^{+0.7}_{-0.7}$	$0.7^{+0.6}_{-0.9}$	$0.2^{+0.7}_{-0.7}$
Cloud-free	log $p_b$	...	...	...
Gray clouds (log-uniform $\tau$ )	log $p_b$	$0.50^{+0.28}_{-0.28}$	$0.50^{+0.29}_{-0.28}$	$0.52^{+0.27}_{-0.29}$
Gray clouds (uniform $\tau$ )	log $p_b$	$0.51^{+0.28}_{-0.29}$	$0.51^{+0.28}_{-0.29}$	$0.49^{+0.29}_{-0.28}$
Nongray clouds (log-uniform $\tau$ )	log $p_b$	$0.50^{+0.28}_{-0.28}$	$0.52^{+0.28}_{-0.29}$	$0.50^{+0.28}_{-0.28}$
Nongray clouds (uniform $\tau$ )	log $p_b$	$0.50^{+0.28}_{-0.28}$	$0.50^{+0.28}_{-0.28}$	$0.49^{+0.28}_{-0.28}$
Cloud-free	log $\tau$	...	...	...
Gray clouds (log-uniform $\tau$ )	log $\tau$	$-2.2^{+1.7}_{-1.6}$	$-2.0^{+1.5}_{-1.6}$	$-2.2^{+1.8}_{-1.6}$
Gray clouds (uniform $\tau$ )	$\tau$	$1^{+10}_{-7}$	$11^{+5}_{-6}$	$4^{+8}_{-8}$
Nongray clouds (log-uniform $\tau$ )	log $\tau$	$-2.0^{+1.7}_{-1.7}$	$-2.1^{+1.6}_{-1.6}$	$-2.2^{+1.8}_{-1.6}$
Nongray clouds (uniform $\tau$ )	$\tau$	$4^{+9}_{-8}$	$3^{+10}_{-8}$	$3^{+10}_{-8}$
Cloud-free	log $Q_0$	...	...	...
Gray clouds (log-uniform $\tau$ )	log $Q_0$	...	...	...
Gray clouds (uniform $\tau$ )	log $Q_0$	...	...	...
Nongray clouds (log-uniform $\tau$ )	log $Q_0$	$1.0^{+0.6}_{-0.6}$	$1.0^{+0.6}_{-0.6}$	$1.0^{+0.6}_{-0.6}$
Nongray clouds (uniform $\tau$ )	log $Q_0$	$1.0^{+0.6}_{-0.6}$	$1.0^{+0.6}_{-0.6}$	$1.0^{+0.6}_{-0.6}$
Cloud-free	$a_0$	...	...	...
Gray clouds (log-uniform $\tau$ )	$a_0$	...	...	...
Gray clouds (uniform $\tau$ )	$a_0$	...	...	...
Nongray clouds (log-uniform $\tau$ )	$a_0$	$5.0^{+1.1}_{-1.1}$	$5.0^{+1.1}_{-1.1}$	$5.0^{+1.1}_{-1.1}$
Nongray clouds (uniform $\tau$ )	$a_0$	$5.0^{+1.1}_{-1.1}$	$5.0^{+1.1}_{-1.1}$	$5.0^{+1.1}_{-1.1}$
Cloud-free	log $a$	...	...	...
Gray clouds (log-uniform $\tau$ )	log $a$	...	...	...
Gray clouds (uniform $\tau$ )	log $a$	...	...	...
Nongray clouds (log-uniform $\tau$ )	log $a$	$0.3^{+0.8}_{-0.8}$	$0.3^{+0.8}_{-0.8}$	$0.3^{+0.8}_{-0.8}$
Nongray clouds (uniform $\tau$ )	log $a$	$0.4^{+0.7}_{-0.8}$	$0.3^{+0.8}_{-0.8}$	$0.4^{+0.8}_{-0.8}$



## ORCID iDs

Kyle Franson  <https://orcid.org/0000-0003-4557-414X>  
 Brendan P. Bowler  <https://orcid.org/0000-0003-2649-2288>  
 Mariangela Bonavita  <https://orcid.org/0000-0002-7520-8389>  
 Timothy D. Brandt  <https://orcid.org/0000-0003-2630-8073>  
 Minghan Chen  <https://orcid.org/0000-0001-8892-4045>  
 Matthias Samland  <https://orcid.org/0000-0001-9992-4067>  
 Zhoujian Zhang  <https://orcid.org/0000-0002-3726-4881>  
 Anna Lueber  <https://orcid.org/0000-0001-6960-0256>  
 Kevin Heng  <https://orcid.org/0000-0003-1907-5910>  
 Daniel Kitzmann  <https://orcid.org/0000-0003-4269-3311>  
 Trevor Wolf  <https://orcid.org/0000-0002-1406-8829>  
 Brandon A. Jones  <https://orcid.org/0000-0003-3480-6320>  
 Quang H. Tran  <https://orcid.org/0000-0001-6532-6755>  
 Daniella C. Bardalez Gagliuffi  <https://orcid.org/0000-0001-8170-7072>  
 Beth Biller  <https://orcid.org/0000-0003-4614-7035>  
 Justin R. Crepp  <https://orcid.org/0000-0003-0800-0593>  
 Trent J. Dupuy  <https://orcid.org/0000-0001-9823-1445>  
 Jacqueline Faherty  <https://orcid.org/0000-0001-6251-0573>  
 Clémence Fontanive  <https://orcid.org/0000-0002-2428-9932>  
 Tyler D. Groff  <https://orcid.org/0000-0001-5978-3247>  
 Raffaele Gratton  <https://orcid.org/0000-0003-2195-6805>  
 Olivier Guyon  <https://orcid.org/0000-0002-1097-9908>  
 Rebecca Jensen-Clem  <https://orcid.org/0000-0003-0054-2953>  
 Nemanja Jovanovic  <https://orcid.org/0000-0001-5213-6207>  
 N. Jeremy Kasdin  <https://orcid.org/0000-0002-6963-7486>  
 Julien Lozi  <https://orcid.org/0000-0002-3047-1845>  
 Eugene A. Magnier  <https://orcid.org/0000-0002-7965-2815>  
 Koraljka Mužić  <https://orcid.org/0000-0002-7989-2595>  
 Aniket Sanghi  <https://orcid.org/0000-0002-1838-4757>  
 Christopher A. Theissen  <https://orcid.org/0000-0002-9807-5435>

## References

- Abel, M., Frommhold, L., Li, X., & Hunt, K. L. C. 2011, *JPCA*, **115**, 6805  
 Abel, M., Frommhold, L., Li, X., & Hunt, K. L. C. 2012, *JChPh*, **136**, 044319  
 Ackerman, A. S., & Marley, M. S. 2001, *ApJ*, **556**, 872  
 Allard, N. F., Spiegelman, F., & Kielkopf, J. F. 2016, *A&A*, **589**, A21  
 Allard, N. F., Spiegelman, F., Leininger, T., & Molliere, P. 2019, *A&A*, **628**, A120  
 Allende Prieto, C., & Lambert, D. L. 1999, *A&A*, **352**, 555  
 Amara, A., & Quanz, S. P. 2012, *MNRAS*, **427**, 948  
 Anders, F., Khalatyan, A., Queiroz, A. B. A., et al. 2022, *A&A*, **658**, A91  
 Astropy Collaboration, Price-Whelan, A. M., Sipocz, B. M., et al. 2018, *AJ*, **156**, 123  
 Astropy Collaboration, Robitaille, T. P., Tollerud, E. J., et al. 2013, *A&A*, **558**, A33  
 Azzam, A. A. A., Tennyson, J., Yurchenko, S. N., & Naumenko, O. V. 2016, *MNRAS*, **460**, 4063  
 Baraffe, I., Chabrier, G., Allard, F., & Hauschildt, P. H. 2002, *A&A*, **382**, 563  
 Baraffe, I., Chabrier, G., Barman, T. S., Allard, F., & Hauschildt, P. H. 2003, *A&A*, **402**, 701  
 Baraffe, I., Homeier, D., Allard, F., & Chabrier, G. 2015, *A&A*, **577**, A42  
 Barber, R. J., Tennyson, J., Harris, G. J., & Tolchenov, R. N. 2006, *MNRAS*, **368**, 1087  
 Bate, M. R. 2009, *MNRAS*, **397**, 232  
 Beatty, T. G., Morley, C. V., Curtis, J. L., et al. 2018, *AJ*, **156**, 168  
 Beers, T. C., Flynn, K., & Gebhardt, K. 1990, *AJ*, **100**, 32  
 Best, W. M. J., Dupuy, T. J., Liu, M. C., Siverd, R. J., & Zhang, Z. 2020, The UltracoolSheet: Photometry, Astrometry, Spectroscopy, and Multiplicity for 3000+ Ultracool Dwarfs and Imaged Exoplanets, Zenodo, doi:10.5281/ZENODO.4169084  
 Best, W. M. J., Liu, M. C., Magnier, E. A., & Dupuy, T. J. 2021, *AJ*, **161**, 42  
 Best, W. M. J., Magnier, E. A., Liu, M. C., et al. 2018, *ApJS*, **234**, 1  
 Beuzit, J.-L., Vigan, A., Mouillet, D., et al. 2019, *A&A*, **631**, A155  
 Bochanski, J. J., Faherty, J. K., Gagné, J., et al. 2018, *AJ*, **155**, 149  
 Boesgaard, A. M., & Budge, K. G. 1988, *ApJ*, **332**, 410  
 Boesgaard, A. M., & Friel, E. D. 1990, *ApJ*, **351**, 467  
 Bonavita, M., Fontanive, C., Gratton, R., et al. 2022, *MNRAS*, **513**, 5588  
 Boss, A. P. 1997, *Sci*, **276**, 1836  
 Bowler, B. P., Blunt, S. C., & Nielsen, E. L. 2020, *AJ*, **159**, 63  
 Bowler, B. P., Liu, M. C., & Cushing, M. C. 2009, *ApJ*, **706**, 1114  
 Bowler, B. P., Dupuy, T. J., Endl, M., et al. 2018, *AJ*, **155**, 159  
 Bowler, B. P., Endl, M., Cochran, W. D., et al. 2021, *ApJL*, **913**, L26  
 Bradley, L., Sipócz, B., Robitaille, T., et al. 2019, *Astropy/Photutils: V0.7.2*, Zenodo, doi:10.5281/zenodo.3568287  
 Branch, D., Lambert, D. L., & Tomkin, J. 1980, *ApJ*, **241**, L83  
 Brandt, G. M., Brandt, T. D., Dupuy, T. J., Li, Y., & Michalik, D. 2021a, *AJ*, **161**, 179  
 Brandt, G. M., Brandt, T. D., Dupuy, T. J., Michalik, D., & Marleau, G.-D. 2021b, *ApL*, **915**, L16  
 Brandt, G. M., Dupuy, T. J., Li, Y., et al. 2021c, *AJ*, **102**, 301  
 Brandt, T. D. 2018, *ApJS*, **239**, 31  
 Brandt, T. D. 2021, *ApJS*, **254**, 42  
 Brandt, T. D., Dupuy, T. J., & Bowler, B. P. 2019, *AJ*, **158**, 140  
 Brandt, T. D., Dupuy, T. J., Li, Y., et al. 2021d, *AJ*, **162**, 186  
 Brandt, T. D., & Huang, C. X. 2015a, *ApJ*, **807**, 58  
 Brandt, T. D., & Huang, C. X. 2015b, *ApJ*, **807**, 24  
 Brandt, T. D., Rizzo, M., Groff, T., et al. 2017, *JATIS*, **3**, 1  
 Burgasser, A. J., Geballe, T. R., Leggett, S. K., Kirkpatrick, J. D., & Golimowski, D. A. 2006, *ApJ*, **637**, 1067  
 Burrows, A., Hubbard, W. B., Lunine, J. I., & Liebert, J. 2001, *RvMP*, **73**, 719  
 Burrows, A., Marley, M., Hubbard, W. B., et al. 1997, *ApJ*, **491**, 856  
 Butler, R. P., Vogt, S. S., Laughlin, G., et al. 2017, *AJ*, **153**, 208  
 Chambers, K. C., Magnier, E. A., Metcalfe, N., et al. 2016, arXiv:1612.05560  
 Cheetham, A., Ségransan, D., Peretti, S., et al. 2018, *A&A*, **614**, A16  
 Chowdhury, S., Banerjee, P., Garain, D., & Sarkar, T. 2022, *ApJ*, **929**, 117  
 Claudi, R. U., McLean, I. S., Casali, M. M., et al. 2008, *Proc. SPIE*, **7014**, 70143E  
 Craig, M., Crawford, S., Seifert, M., et al. 2017, *Astropy/Ccdproc: V1.3.0*, Post, Zenodo, doi:10.5281/zenodo.1069648  
 Crepp, J. R., Johnson, J. A., Fischer, D. A., et al. 2012, *ApJ*, **751**, 97  
 Cummings, J. D., Deliyannis, C. P., Maderak, R. M., & Steinhauer, A. 2017, *AJ*, **153**, 128  
 Cushing, M. C., Marley, M. S., Saumon, D., et al. 2008, *ApJ*, **678**, 1372  
 Cushing, M. C., Kirkpatrick, J. D., Gelino, C. R., et al. 2011, *ApJ*, **743**, 50  
 David, T. J., & Hillenbrand, L. A. 2015, *ApJ*, **804**, 146  
 De Rosa, R. J., Esposito, T. M., Hirsch, L. A., et al. 2019, *AJ*, **158**, 225  
 DeGennaro, S., von Hippel, T., Jefferys, W. H., et al. 2009, *ApJ*, **696**, 12  
 Delorme, P., Meunier, N., Albert, D., et al. 2017, in *SF2A-2017: Proc. Annual Meeting of the French Society of Astronomy and Astrophysics*, ed. C. Reylyé et al. (Paris: SF2A), **347**  
 Dhital, S., West, A. A., Stassun, K. G., & Bochanski, J. J. 2010, *AJ*, **139**, 2566  
 Dohlen, K., McLean, I. S., Casali, M. M., et al. 2008, *Proc. SPIE*, **7014**, 70143L  
 Douglas, S. T., Agüeros, M. A., Covey, K. R., et al. 2014, *ApJ*, **795**, 161  
 Dupuy, T. J., & Kraus, A. L. 2013, *Sci*, **341**, 1492  
 Dupuy, T. J., & Liu, M. C. 2012, *ApJS*, **201**, 19  
 Dupuy, T. J., & Liu, M. C. 2017, *ApJS*, **231**, 15  
 Dupuy, T. J., Liu, M. C., & Ireland, M. J. 2009, *ApJ*, **692**, 729  
 Dupuy, T. J., Liu, M. C., & Ireland, M. J. 2014, *ApJ*, **790**, 133  
 Faherty, J. K., Burgasser, A. J., West, A. A., et al. 2010, *AJ*, **139**, 176  
 Fegley, B., & Ladders, K. 1994, *Icar*, **110**, 117  
 Fegley, B., Jr., & Ladders, K. 1996, *ApJ*, **472**, L37  
 Fernandes, C. S., Van Grootel, V., Salmon, S. J. A. J., et al. 2019, *ApJ*, **879**, 94  
 Feroz, F., Hobson, M. P., & Bridges, M. 2009, *MNRAS*, **398**, 1601  
 Filippazzo, J. C., Rice, E. L., Faherty, J., et al. 2015, *ApJ*, **810**, 158  
 Flasseur, O., Denis, L., Thiébaud, É., & Langlois, M. 2018, *A&A*, **618**, A138  
 Fontanive, C., Mužić, K., Bonavita, M., & Biller, B. 2019, *MNRAS*, **490**, 1120  
 Foreman-Mackey, D. 2016, *JOSS*, **1**, 24  
 Foreman-Mackey, D., Hogg, D. W., Lang, D., & Goodman, J. 2013, *PASP*, **125**, 306  
 Fortney, J. J., Marley, M. S., Saumon, D., & Ladders, K. 2008, *ApJ*, **683**, 1104  
 Franson, K., Bowler, B. P., Brandt, T. D., et al. 2022, *AJ*, **163**, 50  
 Freedman, R. S., Marley, M. S., & Ladders, K. 2008, *ApJS*, **174**, 504  
 Gagné, J., & Faherty, J. K. 2018, *ApJ*, **862**, 138  
 Gagné, J., Mamajek, E. E., Malo, L., et al. 2018, *ApJ*, **856**, 23

- Gaia Collaboration, Brown, A. G., Vallenari, A., Prusti, T., & de Bruijne, J. H. 2021a, *A&A*, **650**, C3
- Gaia Collaboration, Smart, R. L., Sarro, L. M., et al. 2021b, *A&A*, **649**, A6
- Gaia Collaboration, Prusti, T., de Bruijne, J. H. J., et al. 2016, *A&A*, **595**, A1
- Gaia Collaboration, Brown, A. G. A., Vallenari, A., et al. 2018, *A&A*, **616**, A1
- Galicher, R., Boccaletti, A., Mesa, D., et al. 2018, *A&A*, **615**, A92
- Gebran, M., Vick, M., Monier, R., & Fossati, L. 2010, *A&A*, **523**, A71
- Gharib-Nezhad, E., Marley, M. S., Batalha, N. E., et al. 2021, *ApJ*, **919**, 21
- Glebocki, R., & Gnacinski, P. 2005, *yCat*, **III/244**
- Gomez Gonzalez, C. A., Wertz, O., Absil, O., et al. 2017, *AJ*, **154**, 7
- Gonzales, E. J., Crepp, J. R., Bechter, E. B., et al. 2020, *ApJ*, **893**, 27
- Goody, R., West, R., Chen, L., & Crisp, D. 1989, *JQSRT*, **42**, 539
- Gossage, S., Conroy, C., Dotter, A., et al. 2018, *ApJ*, **863**, 67
- Gray, D. F. 2005, *The Observation and Analysis of Stellar Photospheres* (3rd edn; Cambridge: Cambridge Univ. Press)
- Grimm, S. L., & Heng, K. 2015, *ApJ*, **808**, 182
- Grimm, S. L., Malik, M., Kitzmann, D., et al. 2021, *ApJS*, **253**, 30
- Groff, T. D., Chilcote, J., Kasdin, N. J., et al. 2016, *Proc. SPIE*, **9908**, 164
- Guizar-Sicairos, M., Thurman, S. T., & Fienup, J. R. 2008, *OptL*, **33**, 156
- Harris, C. R., Millman, K. J., van der Walt, S. J., et al. 2020, *Natur*, **585**, 357
- Horne, K. 1986, *PASP*, **98**, 609
- Huby, E., Baudoz, P., Mawet, D., & Absil, O. 2015, *A&A*, **584**, A74
- Huby, E., Bottom, M., Femenia, B., et al. 2017, *A&A*, **600**, A46
- Hunter, J. D. 2007, *CSE*, **9**, 90
- Joner, M. D., Taylor, B. J., Laney, C. D., & van Wyk, F. 2006, *AJ*, **132**, 111
- Jovanovic, N., Guyon, O., Martinache, F., et al. 2015a, *ApJ*, **813**, L24
- Jovanovic, N., Martinache, F., Guyon, O., et al. 2015b, *PASP*, **127**, 890
- Karhunen, K. 1947, *AASF*, **37**, 79
- Kervella, P., Arenou, F., Mignard, F., & Thévenin, F. 2019, *A&A*, **623**, A72
- Kervella, P., Arenou, F., & Thévenin, F. 2022, *A&A*, **657**, A7
- Kirkpatrick, J. D. 2005, *ARA&A*, **43**, 195
- Kirkpatrick, J. D., Looper, D. L., Burgasser, A. J., et al. 2010, *ApJS*, **190**, 100
- Kitzmann, D., Heng, K., Oreshenko, M., et al. 2020, *ApJ*, **890**, 174
- Kolmogorov, A. 1933, *Inst. Ital. Attuari, Giom.*, **4**, 83
- Kopytova, T. G., Brandner, W., Tognelli, E., et al. 2016, *A&A*, **585**, A7
- Kovács, G., Zucker, S., & Mazeh, T. 2002, *A&A*, **391**, 369
- Kumar, S. S. 1963, *ApJ*, **137**, 1121
- Kuzuhara, M., Currie, T., Takarada, T., et al. 2022, *ApJL*, **934**, L19
- Lagrange, A.-M., Bonnefoy, M., Chauvin, G., et al. 2010, *Sci*, **329**, 57
- Langlois, M., Gratton, R., Lagrange, A.-M., et al. 2021, *A&A*, **651**, A71
- Lebreton, Y., Fernandes, J., & Lejeune, T. 2001, *A&A*, **374**, 540
- Lightkurve Collaboration, Cardoso, J. V. d., Hedges, C., et al. 2018, *Lightkurve: Kepler and TESS Time Series Analysis in Python*, Astrophysics Source Code Library, ascl:1812.013
- Lindgren, L. 2018, *Re-Normalising the Astrometric Chi-Square in Gaia DR2*, Technical Report, GAIA-C3-TN-LU-LL-124-01
- Liu, M. C. 2004, *Sci*, **305**, 1442
- Liu, M. C., Dupuy, T. J., & Allers, K. N. 2016, *ApJ*, **833**, 96
- Liu, M. C., Dupuy, T. J., & Leggett, S. K. 2010, *ApJ*, **722**, 311
- Lodders, K. 1999, *ApJ*, **519**, 793
- Lodders, K. 2002, *ApJ*, **577**, 974
- Lodders, K. 2003, *ApJ*, **591**, 1220
- Lodders, K., & Fegley, B. 2002, *Icar*, **155**, 393
- Lodders, K., & Fegley, B., Jr. 2006, *Chemistry of Low Mass Substellar Objects* (Chichester: Praxis), 1
- Lodieu, N. 2020, *MmSAI*, **91**, 84
- Lodieu, N., Rebolo, R., & Pérez-Garrido, A. 2018, *A&A*, **615**, L12
- Lodieu, N., Smart, R. L., Pérez-Garrido, A., & Silvotti, R. 2019, *A&A*, **623**, A35
- Loève, M. 1948, in *Processus Stochastique et Mouvement Brownien*, ed. P. Lévy (Paris: Gauthier-Villars)
- Lovis, C., & Pepe, F. 2007, *A&A*, **468**, 1115
- Lucey, L. B., & Sweeney, M. A. 1971, *AJ*, **76**, 544
- Lueber, A., Kitzmann, D., Bowler, B. P., Burgasser, A. J., & Heng, K. 2022, *ApJ*, **930**, 136
- Magnier, E., Schlafly, E., Finkbeiner, D. P., et al. 2020, *ApJS*, **251**, 6
- Maire, A.-L., Langlois, M., Dohlen, K., et al. 2016, *Proc. SPIE*, **9908**, 990834
- Maire, A.-L., Molaverdikhani, K., Desidera, S., et al. 2020, *A&A*, **639**, A47
- Marleau, G.-D., & Cumming, A. 2014, *MNRAS*, **437**, 1378
- Marley, M., & Robinson, T. 2015, *ARA&A*, **53**, 279
- Marley, M. S., & McKay, C. P. 1999, *Icar*, **138**, 268
- Marley, M. S., Saumon, D., Guillot, T., et al. 1996, *Sci*, **272**, 1919
- Marley, M. S., Seager, S., Saumon, D., et al. 2002, *ApJ*, **568**, 335
- Marley, M. S., Saumon, D., Visscher, C., et al. 2021, *ApJ*, **920**, 85
- Marocco, F., Eisenhardt, P. R. M., Fowler, J. W., et al. 2021, *ApJS*, **253**, 8
- Marchetti, E., Close, L. M., Veran, J.-P., et al. 2014, *Proc. SPIE*, **9148**, 91480U
- Marois, C., Doyon, R., Racine, R., & Nadeau, D. 2000, *PASP*, **112**, 91
- Marois, C., Lafrenière, D., Doyon, R., Macintosh, B., & Nadeau, D. 2006, *ApJ*, **641**, 556
- Marois, C., Zuckerman, B., Konopacky, Q. M., Macintosh, B., & Barman, T. 2010, *Natur*, **468**, 1080
- Martín, E. L., Lodieu, N., Pavlenko, Y., & Bejar, V. J. S. 2018, *ApJ*, **856**, 40
- Mawet, D., Milli, J., Wahhaj, Z., et al. 2014, *ApJ*, **792**, 97
- McKay, C. P., Pollack, J. B., & Courtin, R. 1989, *Icar*, **80**, 23
- McKinney, W. 2010, in *Proc. 9th Python in Science Conf.*, ed. S. van der Walt & J. Millman (Austin, TX: SciPy), 56
- Meingast, S., & Alves, J. 2019, *A&A*, **621**, L3
- Mesa, D., Gratton, R., Zurlo, A., et al. 2015, *A&A*, **576**, A121
- Murphy, M. T., Tzanavaris, P., Webb, J. K., & Lovis, C. 2007, *MNRAS*, **378**, 221
- Nelder, J. A., & Mead, R. 1965, *CompJ*, **7**, 308
- Nielsen, E. L., De Rosa, R. J., Macintosh, B., et al. 2019, *AJ*, **158**, 13
- Nowak, M., Lacour, S., Lagrange, A.-M., et al. 2020, *A&A*, **642**, L2
- Oblak, E., & Chareton, M. 1981, *A&AS*, **45**, 459
- Olson, G. L., & Kunasz, P. B. 1987, *JQSRT*, **38**, 325
- Oreshenko, M., Kitzmann, D., Márquez-Neila, P., et al. 2020, *AJ*, **159**, 6
- Pace, G., Castro, M., Meléndez, J., Théado, S., & do Nascimento, J.-D., Jr. 2012, *A&A*, **541**, A150
- Pavlov, A., Möller-Nilsson, O., Feldt, M., et al. 2008, *Proc. SPIE*, **7019**, 701939
- Pedregosa, F., Varoquaux, G., Gramfort, A., et al. 2011, *JMLR*, **12**, 2825
- Perryman, M. A. C., Brown, A. G. A., Lebreton, Y., et al. 1998, *A&A*, **331**, 81
- Phillips, M. W., Tremblin, P., Baraffe, I., et al. 2020, *A&A*, **637**, A38
- Pollack, J. B., Hubickyj, O., Bodenheimer, P., et al. 1996, *Icar*, **124**, 62
- Pueyo, L. 2016, *ApJ*, **824**, 117
- Reid, I. N., & Hawley, S. L. 2005, *New Light on Dark Stars : Red Dwarfs, Low-Mass Stars, Brown Dwarfs* (Berlin: Springer)
- Reiners, A., & Zechmeister, M. 2020, *ApJS*, **247**, 11
- Reylé, C. 2018, *A&A*, **619**, L8
- Ricker, G. R., Winn, J. N., Vanderspek, R., et al. 2014, *JATIS*, **1**, 014003
- Rickman, E. L., Ségransan, D., Hagelberg, J., et al. 2020, *A&A*, **635**, A203
- Röser, S., Schilbach, E., & Goldman, B. 2019, *A&A*, **621**, L2
- Röser, S., Schilbach, E., Piskunov, A. E., Kharchenko, N. V., & Scholz, R. D. 2011, *A&A*, **531**, A92
- Rothman, L. S., Gordon, I. E., Barber, R. J., et al. 2010, *JQSRT*, **111**, 2139
- Samland, M., Bouwman, J., Hogg, D. W., et al. 2021, *A&A*, **646**, A24
- Samland, M., Brandt, T. D., Milli, J., Delorme, P., & Vigan, A. 2022, *A&A*, **668**, A84
- Saumon, D., Hubbard, W. B., Burrows, A., et al. 1996, *ApJ*, **460**, 993
- Saumon, D., & Marley, M. S. 2008, *ApJ*, **689**, 1327
- Saumon, D., Marley, M. S., Cushing, M. C., et al. 2006, *ApJ*, **647**, 552
- Scuflaire, R., Théado, S., Montalbán, J., et al. 2008, *Ap&SS*, **316**, 83
- Serabyn, E., Huby, E., Matthews, K., et al. 2017, *AJ*, **153**, 43
- Service, M., Lu, J. R., Campbell, R., et al. 2016, *PASP*, **128**, 095004
- Skilling, J. 2004, in *AIP Conf. Ser. 735, Bayesian Inference and Maximum Entropy Methods in Science and Engineering: 24th Int. Workshop on Bayesian Inference and Maximum Entropy Methods in Science and Engineering*, ed. R. Fischer, R. Preuss, & U. V. Toussaint (Melville, NY: AIP), 395
- Skilling, J. 2006, *BayAn*, **1**, 833
- Skrutskie, M. F., Cutri, R. M., Stiening, R., et al. 2006, *AJ*, **131**, 1163
- Smirnov, N. 1948, *Ann. Math. Stat.*, **19**, 279
- Smith, J. C., Stumpe, M. C., Van Cleve, J. E., et al. 2012, *PASP*, **124**, 1000
- Soubiran, C., Jasniewicz, G., Chemin, L., et al. 2018, *A&A*, **616**, A7
- Soummer, R., Pueyo, L., & Larkin, J. 2012, *ApJ*, **755**, L28
- Sparks, W. B., & Ford, H. C. 2002, *ApJ*, **578**, 543
- Spiegel, D. S., & Burrows, A. 2012, *ApJ*, **745**, 174
- Spiegel, D. S., Burrows, A., & Milsom, J. A. 2011, *ApJ*, **727**, 57
- Stassun, K. G., & Torres, G. 2021, *ApJ*, **907**, L33
- Stumpe, M. C., Smith, J. C., Catanzarite, J. H., et al. 2014, *PASP*, **126**, 100
- Stumpe, M. C., Smith, J. C., Van Cleve, J. E., et al. 2012, *PASP*, **124**, 985
- Takeda, Y., & Honda, S. 2020, *AJ*, **159**, 174
- Tokunaga, A. T., & Vacca, W. D. 2005, *PASP*, **117**, 421
- Toon, O. B., McKay, C. P., Ackerman, T. P., & Santhanam, K. 1989, *JGR*, **94**, 16287
- Trotta, R. 2008, *ConPh*, **49**, 71
- Tull, R. G., MacQueen, P. J., Sneden, C., & Lambert, D. L. 1995, *PASP*, **107**, 251
- van Bueren, H. G. 1952, *BAN*, **11**, 385
- van Dokkum, P. G. 2001, *PASP*, **113**, 1420
- van Saders, J. L., & Pinsonneault, M. H. 2013, *ApJ*, **776**, 67
- Vigan, A., Moutou, C., Langlois, M., et al. 2010, *MNRAS*, **407**, 71

- Virtanen, P., Gommers, R., Oliphant, T. E., et al. 2020, [NatMe](#), 17, 261
- Wang, J. J., Ruffio, J.-B., De Rosa, R. J., et al. 2015, pyKLIP: PSF Subtraction for Exoplanets and Disks, Astrophysics Source Code Library, ascl:1506.001
- Wang, J. J., Ginzburg, S., Ren, B., et al. 2020, [AJ](#), 159, 263
- Wizinowich, P. 2013, [PASP](#), 125, 798
- Xuan, W. J., Mawet, D., Ngo, H., et al. 2018, [AJ](#), 156, 156
- Yelda, S., Lu, J. R., Ghez, A. M., et al. 2010, [ApJ](#), 725, 331
- Yurchenko, S. N., Barber, R. J., & Tennyson, J. 2011, [MNRAS](#), 413, 1828
- Yurchenko, S. N., & Tennyson, J. 2014, [MNRAS](#), 440, 1649
- Zhang, Z., Liu, M. C., Claytor, Z. R., et al. 2021a, [ApJL](#), 916, L11
- Zhang, Z., Liu, M. C., Marley, M. S., Line, M. R., & Best, W. M. J. 2021b, [ApJ](#), 916, 53